# Multidimensional Radiative Transfer

*A thesis submitted to the University of Sydney*
*in fulfillment of the requirements for the degree of*

Doctor of Philosophy

*by*

Michiel J. van Noort

*Department of Theoretical Physics*
*University of Sydney*
*Australia*

*March 2003*

This thesis is partly based on the following publication:

*van Noort, M., Hubeny, I. & Lanz, T. ; 2002, ApJ.,* **568**, *1066*

To the best of my knowledge, this thesis contains no copy or paraphrase of work published by another person, except where duly acknowledged in the text. This thesis contains no material which has been presented for a degree at the University of Sydney or any other university.

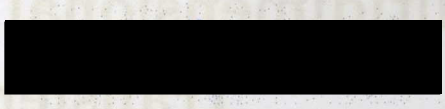

Michiel J. van Noort,
University of Sydney,
March 2003.

# Acknowledgments

I gratefully acknowledge the support of my supervisors, Mark Wardle at the University of Sydney and Ivan Hubeny and Thierry Lanz at the NASA Goddard Space Flight Center, without whom this thesis would not have been possible.

The personal support of Sarah R. Heap at the NASA Goddard Space Flight Center was crucial to the success of my visits there and I thank her for her continuing interest in my work.

Part of the parallel computations reported in this thesis were done on theHIVE, a Beowulf-class parallel computer cluster at the NASA Goddard Space Flight Center. I thank Dr. John Dorband for providing me with access to this system.

Part of the parallel computations reported in this thesis were done on the Swinburne Supercluster, a Beowulf-class parallel computer cluster at Swinburne University, Melbourne, VIC, Australia. I thank Dr. Matthew Bailes for providing me with access to this system.

I also thank the anonymous referee of van Noort, Hubeny & Lanz, 2002, for a number of useful comments and suggestions that helped to improve the presentation of the paper on which chapter 2 is based.

The author was the recipient of an International Postgraduate Research Scholarship (IPRS), granted by the Department of Education Science and Training (DEST) (formerly Department of Education Training and Youth Affairs (DETYA)) of the Commonwealth of Australia and administered by the University of Sydney.

The author was also the recipient of an International Postgraduate Award (IPA), granted and administered by the University of Sydney.

This work was supported by NASA grant 015-97LTSA. A partial support from HST/STIS GTO funds is gratefully acknowledged.

# Abstract

A multidimensional radiative transfer code is presented, using the short characteristics scheme and the ALI method. The code uses the 2-level atom formulation, appropriate for strong resonance lines, and can operate with Cartesian, cylindrical and spherical coordinate systems, the last two assuming rotational symmetry about the $z$-axis.

The emphasis of the code is on accurately treating large, three-dimensional velocity fields on a large number of spatial points and with high angular resolution, in order to deal with complete objects.

To keep the code fast and reduce memory requirements, the code was parallelized for use on a cluster of networked PCs by using a spatial parallelization method, where the computational domain is divided spatially in independent subdomains. It is shown that such a method is both efficient and reliable.

The accuracy of the code was tested at length and was found to be $\sim 5\%$ in most cases of interest.

A spectrum synthesis code is then presented, using the long characteristics method and an Adaptive Mesh Refinement technique. The code can accurately calculate the emergent line profile for a specified inclination angle on a two-dimensional structure with a specified source function assuming rotational symmetry, in cylindrical and spherical coordinate systems. The accuracy of the code was determined to be of the order of 1%, given the structure and line source function.

Both codes were then applied to the problem of rotation in expanding stellar winds. The spectroscopic effects of rotation were found to be significant for large inclination angles only, with the largest differences with respect to non-rotating of $\sim 20\%$. The direction of the radiation volume force was found to change at most by a similar amount.

Finally, the codes were applied to calculate line profiles for the disks in cataclysmic variables. The differences due to rotation were found to be significant, with the cores of strong resonance lines brightened by about 50% for small inclination angles. The radiation force was not found to be strongly affected.

# Contents

# Chapter 1

# Introduction

Radiative transfer is a fundamental ingredient of modern astronomy. The reason for this is simple: the vast majority of the information that we receive from astrophysical objects comes to us in the form of electromagnetic radiation of some sort. Moreover, in many astrophysical objects, the structures are not merely probed by the radiation field, they are in fact determined by it. Understanding the interplay between the radiation field and the material of the structure, can tell us something about the processes that are important and the conditions under which they occur.

As many situations that are common in astrophysics cannot be recreated in a laboratory, much of the information we derive from radiation necessarily comes from analytical and numerical modeling of the object under consideration. A rough analysis of this type is usually sufficient to understand the basic configuration of an object, but to understand more precisely the physical processes giving rise to the observed radiation field, one needs to model the object in more detail.

Unfortunately, the radiative transfer equation, although seemingly simple, is a very complicated, non-linear equation for which few analytical solutions exist. The numerical effort involved in solving it for even modest problems is considerable, so that large scale detailed calculations have not been possible until recent advances in computer technology and numerical techniques.

For the most part, this increase in numerical capacity has been used to increase the level of detail in the atomic data, needed to accurately calculate the opacity, electron density and the temperature and density structures. Currently, in 1 dimension (hereafter 1-D) it is possible to calculate the

structure of an object by comparing it to the observed spectrum, with great detail, including hundreds of atomic energy levels explicitly, and millions of spectral lines implicitly using opacity sampling (Anderson 1989), in a matter of hours.

For the vast majority of astrophysical objects, the 1-D plane-parallel approximation, where the object is considered to be infinite and flat, is a good one, and very detailed calculations yielding information about the local structure, gravity, chemical composition, and velocity fields are carried out routinely. Many codes exist that can perform detailed calculations of plane-parallel atmospheres involving many atomic species containing hundreds of levels and millions of lines (for instance TLUSTY (Hubeny 1988), MULTI (Carlsson 1986), PHOENIX (Hauschildt 1992), etc.).

Although few astrophysical objects are actually plane-parallel, there are a few seemingly obviously multidimensional objects that can nonetheless be approximated using a so-called $1\frac{1}{2}$-D method, that is: a series of independent 1-D plane-parallel solutions. For this to be possible, it is necessary that the optical thickness of the object in the direction of the multidimensional variations is much larger than the thickness of the atmosphere, such as in optically thick accretion disks (Hubeny, 1990).

Many objects have been successfully modeled using the methods described above, however, there are limits to their applicability, and there are many objects that are not well described by the 1-D plane-parallel approximation. The most obvious class of objects for which this is true are objects with geometrically extended regions that are neither optically very thick nor thin. The way we interpret the radiation coming from these objects is directly related to the level of realism we use to model them, including the dimensionality of the model. In many cases, the extended nature of the envelope can be appropriately treated by assuming spherical symmetry, in which case the problem can still be treated in 1-D in a spherical coordinate system, although the increase in numerical effort of this approach is appreciable, as the angular dependence of the intensity requires significantly more angular points than the 3 needed in the 1-D plane parallel approximation (Chapman 1966).

Many of the difficulties in dealing with expanding envelopes, high velocities, spherical geometry, etc., were solved in the 2-level atom formalism in the 1970's (Hummer & Rybicky 1971, Castor 1972, Mihalas, Kunanz & Hummer 1975, and many others), enabeling the use of strong spectral lines for diagnostic purposes in stellar winds, supernovae, etc.. Over the years, more detail has been added, so that currently spherically symmetric atmospheric structures including detailed multilevel atomic data can be

accurately calculated (Hillier 1990, Koesterke 2002).

There are, however, situations, where the geometrical configuration simply does not allow for a 1-D treatment. It has been long known from observations of the line spectra of massive stars, that they rotate at a significant fraction of their breakup rotation rate (Slettebak 1948). Even if their structures are assumed to be spherically symmetric (and this is not likely, see for instance Tassoul 2000), the velocity field itself is not spherically symmetric and warrants a multidimensional treatment of the radiation transfer. Additionally, the turbulent velocities in the extended outflows of massive stars, needed to explain the observed line profiles, exceed the sound speed in the wind (Mihalas 1964) and are therefore likely to result in multidimensional density fluctuations due to shocks (Owocki & Puls 2002).

There are astrophysical objects emitting high energy radiation (X, $\gamma$), the thermal and geometrical properties of which can only be explained by material being accreted onto a massive object, thus converting gravitational energy into heat (see e.g. Frank, King & Raine 2002 or Hilditch 2001 for an overview). As accretion processes are rarely spherically symmetric due to conservation of angular momentum, the radiation fields of these flows can only be modeled in 2 or 3 dimensions.

The unprecedented increase in the resolution and sensitivity of telescopes, both earth- and space-based, over the last few decades, has lead to an enormous increase in the level of detail in observations of extended astrophysical structures, much of which cannot be properly analysed using diagnostic tools based on a 1-D structure.

However, the increase in the numerical effort needed to go beyond 1-D are enormous and, apart from several isolated studies, have not been widely used to calculate line profiles or atmospheric structures in detail.

## 1.1 Multidimensional radiative transfer

Multidimensional radiative transfer is not fundamentally different from 1-D radiative transfer. Although the transfer equation itself is fundamentally 1-D, what we classify as a 1-D problem in fact consists of 1 spatial, 1 angular and 1 frequency dimension, and so in fact is 3-D. The large complications in going from 1-D to 2-D or 3-D is the increase in the required amount of work. The step from 1-D to 2-D adds not only the spatial dimension, but also an angular dimension, as rotational symmetry about the spatial dimension, as is the case for 1-D, does no longer exist. In addition, the convenient situation that, in 1-D plane-parallel, every ray intersecting one

point also intersects all other points (or, for 1-D spherical coordinates, that a subset of rays going through one gridpoint intersects a subset of all other gridpoints), does not exist, so that the amount of work scales much less favorably.

Monte-Carlo methods have been in existence for decades and may be favoured due to its close resemblence to the actual process of radiation transfer. It has been successfully applied to many optically thin astrophysical problems and it remains the method of choice for high energy continuum scattering. It is, however, not particularly well suited for problems with large optical depths and strong resonance scattering, such as resonance line formation in stellar outflows, due to the large number of scatterings per photon (Hummer 1964), and the large number of photons needed to get the statistical error down to an acceptable level.

Once the choice has been made to treat the radiation field as a continuum, the main effort is to minimise the amount of work somehow, by solving the radiation field in ways that scale as favorably as possible. Many codes based on various methods have been developed (Mihalas, Auer & Mihalas, 1978; Adam, 1990; Auer, Fabiani Bendicho & Trujillo-Bueno 1994; Fabiani Bendicho, Trujillo-Bueno & Auer, 1997; Papkalla 1996; Botnen 1997; Busche & Hillier 2000; Dullemond & Turolla 2000; to name just a few), that have been shown to be efficient and robust.

Although most of them were extensively tested, an extensive survey of multidimensional effects in astrophysically realistic problems was in many cases left for later, usually due to the limitations in numerical resources.

The potential applications for a multidimensional radiative transfer code can be roughly divided in two types of applications: local and global.

For local applications, the main interest has been on the (time dependent) modeling of complex 3-D structures, such as the convective cells observed on the surface of late type stars like the sun. This is done by considering a small patch of a larger structure, and applying periodic boundary conditions in the horizontal directions (see for instance Skartlien 2000, Dorch & Nordlund 2001), with the aim of understanding line formation and coronal heating found in stars with surface convection. Although the multidimensional character of the problem is undeniable, the impact of this on the radiation field has thus far proved to be limited, although Fabiano (1998) reports important changes for individual lines.

For global applications, the situation looks less promising. Instead of modeling a small patch of a periodic structure, the object needs to be modeled as a whole, introducing a wide range of length scales in the problem. Also the velocity fields involved can range from a few $\mathrm{km\,s^{-1}}$ to a significant

fraction of the speed of light, so that great care has to be taken to treat them accurately.

Most of the work on this type of objects has been done on disks in $1\frac{1}{2}$-D (Hubeny 1990), to produce reliable diagnostic tools for reproducing observations, and in 2-D, in conjunction with structures generated by MHD codes (for instance Stone, Mihalas & Norman 1992), to understand the nature of the turbulent viscosity in accretion disks, the formation of polar outflows in accreting systems, and to investigate Non-LTE spectral line formation in these structures (Proga, Kallman, Drew & Hartley 2002).

However, routinely applying a multidimensional radiative transfer code as a diagnostic tool is far from being realised.

In the following, we will concentrate mainly on the global type of objects, to be specific: massive stars and disks. The multidimensional character of these objects is obvious, yet in many cases their properties have been studied with 1-D or semi-1-D methods only. When, however, multidimensional velocity fields are considered, as is manifestly appropriate for many of these objects, the applicability of the 1-D methods needs to be reconsidered. To deal with this type of object, a fast, efficient code is needed, capable of treating large velocities accurately and able to deal with a large number of points and angles, to resolve the entire object adequately, in a reasonable amount of time.

## 1.2 Thesis outline

This thesis sets out to investigate multidimensional radiative transfer effects in extended structures with large velocities. The aim is to investigate how important multidimensional effects are in these structures and what the qualitative nature is of the error made by the approximate 1-D methods available.

In chapter 2, a new numerical code is described, that can solve the radiative transfer equation in 2 dimensions in Cartesian, cylindrical and spherical coordinate systems, the latter two under the assumption of rotational symmetry, while treating large velocity fields accurately. A new method of parallelization is outlined and tested and the performance of this method is tested on a cluster of networked PCs. The parallelized code is then tested for accuracy by applying it to structures that are 1-D in one coordinate system, but 2-D with rotational symmetry in another.

In chapter 3, a new code is described that can calculate the emergent line profile from a 2-D structure with rotational symmetry using the long

characteristics method. The resolution is automatically managed with an adaptive mesh refinement technique, to ensure accurate results.

In chapter 4 the codes developed in chapters 2 and 3 are applied to the astrophysically interesting problem of the effect of rotation on the radiation field in a differentially rotating stellar wind. The differences between the emergent line profiles and the radiation forces between the non-rotating 1-D and the rotating 2-D methods are discussed for several rotation rates and line strengths.

In chapter 5 the codes developed in chapters 2 and 3 are used to calculate the line profiles of some important diagnostic spectral lines in the disks of cataclysmic variables on detailed LTE structures.

Finally, in chapter 6, some general results from the 2-D calculations are discussed.

# References

1. Adam, J; 1990, A.&A., **240**, 541
2. Anderson, L. S.; 1989, ApJ., **339**, 558
3. Auer, L.; Fabiani Bendicho, P. & Trujillo-Bueno, J.; 1994, A.&A., **292**, 599
4. Botnen, A., 1997, Masters Thesis, Institute of Theoretical Astrophysics, University of Oslo
5. Busche, J.R., & Hillier, D.J. 2000, ApJ, 531, 1071
6. Carlsson, M.; 1986, Uppsala Astronomical Observatory Technical Report, **33**
7. Castor, J.; 1972, ApJ, **178**, 779
8. Chapman, R.; 1966, ApJ, **143**, 61
9. Dorch, S.; Nordlund, Å.; 2001, A.&A., **365**, 562
10. Dullemond, C. & Turolla, R.; 2000, A.&A., **360**, 1187
11. Fabiani Bendicho, P., A.&S.S., 1998, **263**, 223
12. Fabiani Bendicho, P., Trujillo-Bueno, J. & Auer, L.; 1997, A.&A., **324**, 161

13. Frank, J., King, A. & Raine, D.; *Accretion power in astrophysics*, 3rd ed., Cambridge univ. Press, New York, 2002

14. Hauschildt, P.; 1992, J.Q.S.R.T., **47**, 433

15. Hilditch, R.W.; *An introduction to Close Binaries*, Cambridge univ. Press, New York, 2001

16. Hillier, D.J., 1990, A.&A., **231**, 116

17. Hubeny, I., 1988, Computer Physics Comm., **52**, 103

18. Hubeny, I., 1990, ApJ., **351**, 632

19. Hummer, D.G.; 1964, ApJ., **140**, 276

20. Hummer, D.G. & Rybicky, G.; 1971, M.N.R.A.S., **152**, 1

21. Mihalas, D., 1964, ApJ, **140**, 885

22. Mihalas, D., Auer, L.H., & Mihalas, B.W., 1978, ApJ, 220, 1001

23. Mihalas, D., Kunanz P. & Hummer, D.; 1975, ApJ., **202**, 465

24. Koesterke, L., Hamann, W-R, Gräfner, G.; 2002, A.&A., **384**, 562

25. Owocki, S. & Puls, J.; 2002, ApJ., **568**, 965

26. Papkalla, R; 1994, A.&A., **295**, 551

27. Proga, D.; Kallman, T.; Drew, J. & Hartley, L.; 2002, ApJ., **572**, 382

28. Skartlien, R.; 2000, ApJ., **536**, 465

29. Slettebak, A.; 1948, AJ., **53**, 204

30. Stone, J. Mihalas, D. Norman, M.; 1992, ApJS, **80**, 819

31. Tassoul, J.; *Stellar Rotation*, Cambridge University Press, New York, 2000

# Chapter 2

# A Universal 2-D Short-Characteristics Scheme for Cartesian, Spherical, and Cylindrical Coordinate Systems

**An efficient and robust 2-dimensional non-LTE radiation transfer solver appropriate for line transfer in the equivalent-two-level atom formalism was developed. The numerical method applies the Accelerated Lambda Iteration technique, together with the short characteristics scheme. The code presented here incorporates all three standard geometries (Cartesian, cylindrical and spherical) in a transparent way, while allowing for arbitrary (3-dimensional) velocity fields. The geometry-specific parts of the radiative transfer solver are modularized, so that a change of geometry is accomplished by simply setting the appropriate switch. The code was parallelized in spatial sub-domains, and it was shown that such a scheme is sufficiently robust. A number of tests of the performance of the solver in all three geometries were performed and the internal accuracy of the transfer solutions depending on the spatial, angular, and frequency resolution is discussed.**

## 2.1 Introduction

In the past, astronomers were forced, by the lack of adequate computer resources, to model observed objects by assuming a simple 1-dimensional (1-D) geometry. For instance, stellar atmospheres were typically treated as 1-D plane-parallel slabs, or, in some cases, as spherically symmetric media, which are still 1-D. Even circumstellar and interstellar structures were routinely treated by approximating them by means of 1-D structures.

This simplification is quite understandable, and was justified in view of the enormous complexity of modeling multidimensional systems by using numerical simulations. However, many structures in the Universe are complex 3-D, highly dynamical structures, and should be treated as such. Modeling using a simplified geometry of course served its role in the historical development of the field, but one has to always strive to achieve as high a degree of realism as possible. One of the most important features which determines the degree of realism is the adopted geometrical formulation (dimensionality) of the problem.

Detailed 2-D and 3-D hydrodynamic simulations have now become more routine in many branches of applied physics. The progress was spurred by an enormous development of computer technology and fast and ingenious numerical methods. However, in astrophysics we face an additional complication which arises from the special role played by the radiation field. For most astronomical objects (e.g., stellar atmospheres, accretion disks, H II regions), radiation is not only a *probe* of the physical state, but also an *important constituent.* Radiation in fact *determines* the structure of the medium, yet the medium is analyzed *only* by this radiation. Modeling of these astronomical objects has to be done using radiation hydrodynamics, or, if the magnetic fields are important, radiation magneto hydrodynamics. Several efficient and successful codes of this sort exist, one of them being ZEUS-2D (Stone & Norman, 1992a,b; Stone, Mihalas, & Norman 1992). Other codes are ALTAIR (Dykema, Klein, & Castor 1996) which can solve the time-dependent non-LTE radiative transfer equation for a 2-D axisymmetric geometry; radiation hydrodynamic codes of Kley (1989); Eggum, Coroniti, & Katz (1987); Nordlund & Stein (1991 and references therein), to name just a few.

Most of the above mentioned codes (with the exception of ALTAIR) do not treat the radiation adequately. Rather, they employ various approximations to describe the radiation field, e.g., the diffusion approximation, flux-limiters, the escape probability approach. A review of various approaches may be found in the textbook by Mihalas & Mihalas (1984).

The ZEUS-2D code is able to treat the radiation transfer self-consistently, by solving the radiative transfer equation simultaneously with the hydrodynamical equations. However, there are still significant approximations involved. The most important one is that of local thermodynamic equilibrium (LTE), which assumes that the source function in the radiative transfer equation is given by the Planck function.

We have thus begun a long-term study whose final goal is to develop a methodology for self-consistent 3-D, non-LTE, radiation hydrodynamic modeling. The most important intermediate goal is to develop an efficient and robust radiation transfer solver which will calculate the emergent spectrum of already existing MHD models.

Such an effort is by no means new. Multi-dimensional radiative transfer has a long history in astrophysics. We are interested here in numerical methods that are able to provide essentially exact solutions under a wide range of conditions, so we leave aside a vast literature on Monte Carlo methods, as well as on the approximate methods based on the diffusion approximation.

A review of early efforts together with an extensive bibliography is presented by Cram, Durrant, and Kneer (1977). One of the most important papers in the early history of this field is that of Cannon (1970; see also Cannon & Rees 1971), which aimed at essentially exact 2-D, NLTE radiative transfer in a spectral line in the context of a two-level atom. The method represents an extension of the well-known Feautrier (1964) method to two dimensions; it is, however, computationally very demanding which precludes its application to any realistic cases.

An important step further was taken by Mihalas, Auer, & Mihalas (1978; hereafter referred to as MAM), who have introduced the method of short characteristics. The authors used the Rybicki (1971) instead of the Feautrier elimination technique, which led to a considerable saving of computer time with respect to Cannon's method. The MAM approach was essentially an explicit scheme, and was based on difference approximations of the second-order differential equations. Consequently, it was still computationally rather intensive. The use of the difference equation scheme was motivated by a need to achieve a second-order accuracy of the scheme.

In an extremely important paper, Kunasz & Auer (1988) showed that one can achieve a second-order accuracy by using a formulation of the short-characteristics scheme based on a direct integration of the transfer equation over a cell, by using a parabolic interpolation in the optical depth. Kunasz & Auer (1988) considered a formal solution (i.e. a solution with a specified source function), and demonstrated that their scheme yields a significantly

faster numerical scheme for treating radiative transfer in several dimensions than any other existing method. The method was subsequently extended by Kunasz & Olson (1988) to treat 2-D NLTE transfer for 2-level atoms. They were the first who applied the idea of Accelerated Lambda Iteration (ALI); in the context of multi-D radiative transfer. More specifically, Kunasz & Olson applied the idea of a diagonal (local) approximate operator, suggested earlier in the context of 1-D transfer in a seminal paper by Olson, Auer, & Buchler (1986).

A further improvement on the above approaches was developed by Auer & Paletou (1994), who introduced monotonic upwind interpolations that lead to an improved stability of the numerical scheme. The method was further upgraded by Auer, Fabiani-Bendicho, & Trujillo-Bueno (1994) who generalized the short-characteristics method to the astrophysically interesting case of horizontal periodic boundary conditions and developed an efficient multilevel 2-D code based on the MALI scheme of Rybicki & Hummer (1991, 1992).

A different approach was adopted by Trujillo-Bueno & Kneer (1990), based on an earlier paper by Kneer (1981), who consider a direct method for solving 2-D and even 3-D radiative transfer in two-level atom problems. It assumes that the horizontal fluctuations of the physical quantities are small perturbations of the underlying, unperturbed 1-D atmosphere. This allows one to linearize the transfer problem, and thus to end up with a system of equations which is practically as easy to solve as a 1-D problem. An important point is that interpolations are not needed here because one only needs to find the variations of the amplitude of the sinusoidally fluctuating line source function with height.

All the above mentioned papers consider Cartesian geometry. This geometry is very convenient to formulate the short-characteristics scheme in. However, in many cases of interest it is advantageous to consider other geometrical coordinates, that are dictated by the geometrical shape of the objects (essentially spherical stars; cylindrical disks, etc.). Kunasz (quoted e.g. by Steiner 1991) has developed a code, CYL2D, which uses ALI for solving the two-level atom problem in cylindrical coordinates. Unfortunately, a description of the code may be found only as an internal report of the Los Alamos National Laboratory. Recently, Dullemond & Turolla (2000) developed a short-characteristics scheme in spherical coordinates to treat axisymmetric media. Similarly, Busche & Hillier (2000), and Koesterke, Hamann, & Graefener (2001), developed a spherical short-characteristics scheme for solving the transfer equation in spherically expanding atmospheres.

Finally, we mention that fully 3-D NLTE radiative transfer solvers are

rapidly becoming available. Recently, Fabiani-Fendicho & and Trujillo-Bueno (1999) generalized the short-characteristics formal solver of Auer, Fabiani-Bendicho & Trujilo-Bueno (1994) to 3-D Cartesian coordinates, imposing horizontal periodic boundary conditions in two dimensions, with a generalized and improved monotonic upwind interpolation strategy. They incorporated not only the MALI scheme of Rybicky & and Hummer, but also the MUGA (multilevel Gauss-Seidel) scheme of Trujillo-Bueno & Fabiani-Bendicho (1995) that provides a considerably higher convergence rate than the approach based on a local approximate operator. Finally, Fabiani-Bendicho, Trujillo-Bueno, & Auer (1997) developed a non-linear multigrid method (which extends the previously developed linear multigrid method by Steiner 1991), which is of particular interest for the solution of very complex 2-D and 3-D problems because its convergence rate does not deteriorate as the grid size is reduced.

In this chapter, we describe our variant of the 2-D radiative transfer solver. Analogously to most of the above-mentioned techniques, it uses the two usual ingredients, the short-characteristics scheme together with the ALI approach. Our solver differs from the previous ones essentially in two respects; it is formulated in a universal way so that it can be used in all three basic geometrical systems (Cartesian, cylindrical, and spherical), and we have developed a parallel version of the code that uses a parallelization over spatial sub-domains.

In this chapter we outline the general numerical scheme; it is thus inevitably largely technical. In § 2 we outline the general method of treating multi-D radiative transfer using the ALI method; in § 3 we summarize the numerical scheme for the formal solver of the radiative transfer, namely the short-characteristics method. In § 4 we describe the implementation of the method in the three standard coordinate systems, Cartesian, cylindrical, and spherical. § 5 outlines a parallel implementation of the code, and § 6 presents a number of tests and illustrative examples of the actual radiative transfer solutions.

## 2.2 Method

### 2.2.1 Non-LTE radiation transfer in several dimension

In this section we explain how we reduce the numerical complexity of the problem to a manageable size without compromising the underlying physics.

The general radiative transfer equation may be written as (Mihalas 1978)

$$\left(\frac{1}{c}\frac{\partial}{\partial t} + \mathbf{n}\cdot\nabla\right) I(\mathbf{x},\mathbf{n},\nu,t) = \eta(\mathbf{x},\mathbf{n},\nu,t) - \chi(\mathbf{x},\mathbf{n},\nu,t)\, I(\mathbf{x},\mathbf{n},\nu,t)\,, \quad (2.1)$$

where $I$, $\chi$ and $\eta$ are the specific intensity of radiation and the absorption and emission coefficients, respectively, which are functions of position, $\mathbf{x}$, direction of propagation, $\mathbf{n}$, frequency, $\nu$, and time, $t$. In the following, we will assume that any material time scales in the medium under study are large compared to the photon free-flight time; we may then drop the time derivative from the transfer equation. Along any given ray, the radiative transfer equation is written simply as (dropping the explicit indication of functional dependences)

$$\frac{\partial I}{\partial s} = -\chi(I - S)\,, \quad (2.2)$$

where $s$ is a path length along the ray measured in the direction of propagation, and $S \equiv \eta/\chi$ is the source function. The problem is fully specified by the knowledge of the absorption coefficient (monochromatic opacity) and the source function.

In exact LTE, both the opacity and the source function are expressed as a function of basic state parameters; the source function is equal to the Planck function, (a function of the local temperature $T$ only), while the opacity is a function of $T$ and one additional thermodynamic parameter, taken usually as the electron density, $n_e$. The solution of the transfer equation is then almost trivial in 1-D, where the only problem is to devise an efficient and fast numerical scheme for solving an ordinary differential equation; this scheme may depend on the nature of boundary conditions in each specific case. In a 2-D or 3-D case, the problem is non-trivial, because a given ray does not have to intersect the grid points in which the hydrodynamic solution was obtained, and therefore one has to be very careful about the necessary interpolations.

In a general situation, where the approximation of LTE does not apply, neither the opacity nor the source function are specified functions of the state parameters. They generally depend on individual occupation numbers (populations) of energy levels of atoms/ions whose level transitions contribute to the total opacity/emissivity at a given frequency. These are in turn determined by the set of statistical equilibrium equations which, through the radiative transition rates, depend on integrals over the radiation field itself. The integrals are carried over both frequency and direction.

In other words, one is faced with an intricately coupled problem. The coupling is highly non-linear and, because of the very large mean free path of photons compared to that of massive particles, highly non-local.

Let us take the case of an equivalent two-level atom. Its origins can be traced back to the 1920s and 1930s in the work of Rosseland (1926), Strömgren (1935) and Wooley (1934) in an attempt to explain the core intensity of resonance lines. The approximation is fairly good for strong resonance lines and it represents the simplest example of a non-LTE situation. The source function is given by (i.e. Mihalas 1978)

$$S(\mathbf{x}) = [1 - \epsilon(\mathbf{x})]\bar{J}(\mathbf{x}) + \epsilon(\mathbf{x})\, B(\mathbf{x})\,, \tag{2.3}$$

where

$$\bar{J}(\mathbf{x}) = \int_0^\infty d\nu \oint (d\mathbf{n}/4\pi) I(\nu, \mathbf{n}, \mathbf{x}) \phi(\nu - \nu \mathbf{n}\cdot\mathbf{v}/c)\,, \tag{2.4}$$

and where $\phi(\nu)$ is the absorption profile coefficient, normalized so that $\int_0^\infty d\nu\, \phi(\nu) = 1$; $\mathbf{v}$ is the velocity vector of the absorbing atom, and $\epsilon$ and the Planck function $B$ are the sink and the source terms. Notice that in the strict two-level atom approximation, $\epsilon$ is the destruction parameter, $\epsilon \approx C_{ul}/(C_{ul} + A_{ul})$, where $C_{ul}$ is the collisional de-excitation rate and $A_{ul}$ the spontaneous emission rate from upper level $u$ to lower level $l$. In the present context, we view $\epsilon$ and $B$ as given parameters of the problem.

### 2.2.2 Accelerated Lambda Iteration

The high degree of non-linearity and non-locality of the problem is the reason why multidimensional, self-consistent, non-LTE radiation hydrodynamics was viewed until recently as a virtually impossible task. The situation has however changed dramatically with the advent of the Accelerated Lambda Iteration (ALI) method (for reviews, see Rybicki 1991; Hubeny 1992). This is essentially an application of the method of deferred corrections (or operator splitting) long known in numerical analysis.

The formal solution of equation (2.1) may be written as

$$I_\nu(\mathbf{n}) \;=\; \Lambda_\nu(\mathbf{n})[S]\,, \tag{2.5}$$

where $\Lambda$ operates on the quantity within brackets. We also introduce an integrated operator that gives the mean intensity, $J_\nu$, and the frequency-averaged mean intensity, $\bar{J}$, viz.

$$J_\nu \;=\; \Lambda_\nu[S], \quad \text{where} \quad \Lambda_\nu = \oint \Lambda_\nu(\mathbf{n})(d\mathbf{n}/4\pi)\,, \tag{2.6}$$

and

$$\bar{J} = \bar{\Lambda}[S], \quad \text{where} \quad \bar{\Lambda} = \int \Lambda_\nu \phi_\nu d\nu , \tag{2.7}$$

where we call $\Lambda_\nu$ and $\bar{\Lambda}$ the mean and frequency-averaged lambda operator, respectively. In the following, we will omit the bar in $\bar{\Lambda}$ and simply write $\Lambda$.

The ALI method consists of splitting the $\Lambda$ operator into two parts, $\Lambda = \Lambda^* + (\Lambda - \Lambda^*)$, where $\Lambda^*$ is an appropriately chosen *approximate operator*. Determination of the mean intensity is then understood as an iterative process,

$$J^{(n+1)} = \Lambda^*[S^{(n+1)}] + (\Lambda - \Lambda^*)[S^{(n)}], \tag{2.8}$$

i.e. the approximate operator is acting on the new iterate of the source function, while the correction is applied on the previous (i.e. known) iterate of the source function. The latter term is determined by a set of *formal solutions* of the transfer equation, in other words *solving the transfer equation with fully specified source function*, i.e. solving a single linear differential equation at a time.

The ALI method is efficient if the $\Lambda^*$ operator incorporates all the essential properties of the exact $\Lambda$ operator, but at the same time is easy (and cheap!) to invert. As was rigorously demonstrated by Olson, Auer, & Buchler (1986) in the case of 1-D radiation transfer, a nearly optimum approximate operator is the diagonal (i.e. local) part of the exact $\Lambda$. In the case of multidimensional radiative transfer, the choice of *local* approximate operator is in fact more or less mandatory, as even a first order approximation of the non-local part of $\Lambda$ results in inverting a large matrix. The first application of the ALI technique to 2-D radiative transfer was done by Kunasz & Olson (1988), using the *short characteristics* method for the formal solution developed by Kunasz & Auer (1988). Later, the method was upgraded by Auer & Paletou (1994) and Auer et al. (1994).

The crucial feature of the ALI method is that the coupled problem is numerically reduced to a *set of formal solutions* of the transfer equations. The coupling itself is treated iteratively. This makes the method ideally suited for a modular application in any radiation hydrodynamic code. This also shows that the formal solution routine is an absolutely crucial ingredient of the whole approach, because the speed of an individual formal solution determines the overall time consumption.

The $\Lambda$ operator, which plays the central role in the theory, has in fact never to be constructed explicitly; we may think of $\Lambda$ operator as a *process* of obtaining a formal solution of the transfer equation by any method. However, since we take the approximate $\Lambda^*$ as the diagonal (i.e. local) part

of the exact $\Lambda$, we have to be able to evaluate the local part explicitly. In the 1-D case, a very efficient method was suggested by Rybicki & Hummer (1991). A generalization of this idea to multidimensional transport was outlined by Auer & Paletou (1994). It is based on the observation that

$$\Lambda_{dd} = \Lambda[\delta_{d,d'}]\,, \tag{2.9}$$

i.e. the diagonal part of $\Lambda$ operator is equal to its action on the source function having a non-zero value in only one single grid point. So, it can be evaluated by the exactly same procedure as the formal solution, and the actual coding may always be done in such a way that the evaluation of $\Lambda^*$ is done along any individual formal solution with a negligible increase of the total computer time.

The iteration proceeds as follows

(a) For a given $S^{(n)}$ (with the initial estimate $S^{(0)} = B$, or some other suitable value), we perform a formal solution of the transfer equation by the method of short characteristics, described in the next section. We obtain new values of the specific intensity $I_\nu(\mathbf{n})$, and also new values of the frequency- and angle-dependent elementary $\Lambda^*$-operator.

(b) We calculate a new source function $S^{\rm FS}$ using the new values of the specific intensity (superscript FS stands for formal solution), using equations (2.3) and (2.4), and also the integrated $\Lambda^*$-operator – equations (2.6) and (2.7).

(c) We then calculate a new iterate of the source function, $S^{(n+1)}$ from

$$S^{(n+1)} = S^{(n)} + \frac{S^{\rm FS} - S^{(n)}}{1 - (1-\epsilon)\Lambda^*}\,, \tag{2.10}$$

which follows from equations (2.3) and (2.8), and from the fact that we are using a diagonal (local) $\Lambda^*$ -operator.

(d) Because the source function found in step (*c*) differs from that used in step (*a*), we iterate steps (*a*) through (*c*) to convergence.

Finally, to increase the speed of convergence, we use the Ng acceleration (Auer 1989, 1991), typically after every fourth iteration. The approach consists of constructing an accelerated estimate of the source function based on its values in several previous iterates.

## 2.3 Short Characteristics

As we have shown in the previous section, the ALI method allows us to reduce a general non-linear coupled problem essentially to a set of formal solutions of the transfer equation. Therefore, the formal solution is in a sense a critical component of the overall scheme, because it is done typically thousands to millions of times, and thus has to be as efficient and fast as possible.

### 2.3.1 Basic Principles

Let us first consider the formal solution of the radiative transfer equation along a ray in the absence of velocities. The intensity $I_\nu(s)$ at any position $s$ on the ray is given by the formal solution

$$I_\nu(s) = I_\nu(s_0)\, e^{-\Delta\tau_\nu} + \int_0^{\Delta\tau_\nu} S_\nu(t)\, e^{-(\Delta\tau_\nu - t)}\, dt\,, \tag{2.11}$$

where $\nu$ is the frequency, $S_\nu(t)$ the source function, and $\Delta\tau_\nu$ is the optical depth difference between $s_0$ and $s$, viz.

$$\Delta\tau_\nu = \int_{s_0}^{s} \chi_\nu(s')ds'\,. \tag{2.12}$$

The intensity at any point in space, angle, and frequency can be calculated from equation (2.11), provided $S_\nu$ is known everywhere.

Equation (2.11) can be applied globally to the whole medium under interest. That is, for every grid point one sets up a number of rays that is sufficiently large to reproduce the angular variation of the specific intensity with desired accuracy. Every ray connects the grid point with the boundary, and the intensity in the given grid point is found from equation (2.11). This method is known as the *long characteristics method*; it is quite straightforward, but numerically very costly.

As shown by Mihalas, Auer, & Mihalas (1978 – MAM) and Kunasz & Auer (1988), a significantly more efficient scheme is provided by the *short characteristics method*. Essentially, the method consists of terminating each ray at the closest intersection with a cell boundary. One has thus to solve the transfer equation (i.e., use equation 2.11) only within a given cell. This method clearly involves less work, as the source function needs to be evaluated only in a few points and the integration is simple.

We illustrate the method in the simple case of a Cartesian grid in Figure 2.1. To evaluate the radiation intensity in point 2, we need to know the

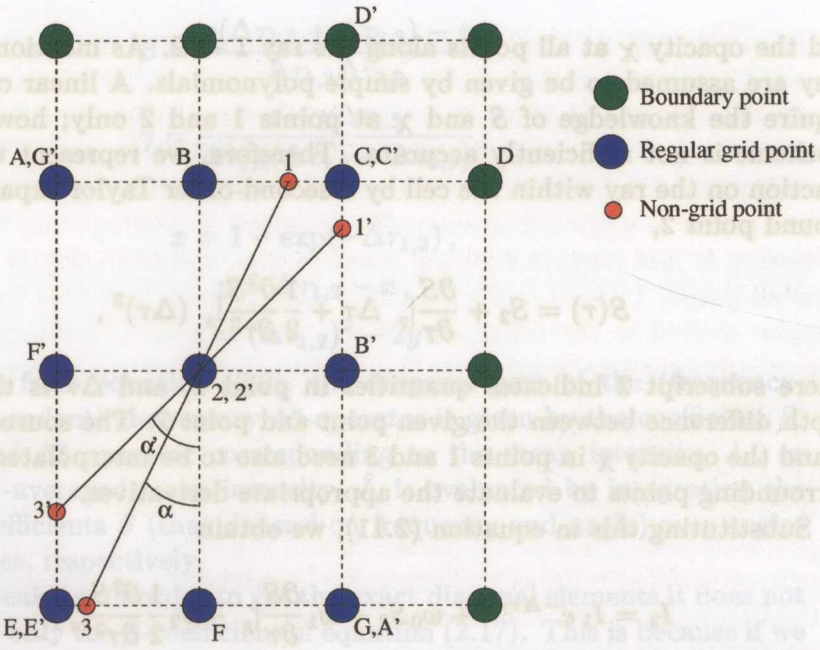


Figure 2.1: *Grid for a sweep over the grid from right to the left (fast loop) and then from top to the bottom (slow loop); or from top to the bottom (fast loop) and then from right to the left (slow loop).*

specific intensity in point 1 (called the upwind end of the short characteristic), after which equation (2.11) can be used, where the spatial variation of the source function between the grid points is assumed to be represented by a simple polynomial.

Since point 1 is in general not a grid point, the intensity needs to be interpolated from values in the closest grid points. If we choose a linear interpolation, the intensities in points B and C are sufficient. However, a linear interpolation is generally not very accurate, so that a large number of spatial points would be required to achieve a sufficient accuracy. A parabolic interpolation is therefore preferable. MAM used an interpolation using the specific intensities in points B, C, and A. This leads to an implicit scheme, because if we follow the prescription that intensities are evaluated in the order which follows the direction of propagation of the radiation, the intensity at point A is not yet known. In the present case, we use the intensity in the next upwind point D, which leads to an explicit scheme, as first suggested by Kunasz & Auer (1988).

Solving equation (2.11) requires the knowledge of the source function $S$

and the opacity $\chi$ at all points along the ray $1 \rightarrow 2$. As mentioned above, they are assumed to be given by simple polynomials. A linear case would require the knowledge of $S$ and $\chi$ at points 1 and 2 only; however such a scheme is not sufficiently accurate. Therefore, we represent the source function on the ray within the cell by a second-order Taylor expansion in $\tau$ around point 2,

$$S(\tau) = S_2 + \frac{\partial S}{\partial \tau}|_2 \ \Delta\tau + \frac{1}{2}\frac{\partial^2 S}{\partial \tau^2}|_2 \ (\Delta\tau)^2 \,, \tag{2.13}$$

where subscript 2 indicates quantities in point 2, and $\Delta\tau$ is the optical depth difference between the given point and point 2. The source function $S$ and the opacity $\chi$ in points 1 and 3 need also to be interpolated from the surrounding points to evaluate the appropriate derivatives.

Substituting this in equation (2.11), we obtain

$$I_2 = I_1 \, e^{-\Delta\tau_{1,2}} + w_0 S_2 + w_1 \frac{\partial S}{\partial \tau}|_2 + w_2 \frac{1}{2}\frac{\partial^2 S}{\partial \tau^2}|_2 \,, \tag{2.14}$$

where

$$\begin{aligned} w_0 &= 1 - e^{-\Delta\tau_{1,2}} \,, \\ w_1 &= w_0 - \Delta\tau_{1,2} \, e^{-\Delta\tau_{1,2}} \,, \\ w_2 &= 2w_1 - (\Delta\tau_{1,2})^2 \, e^{-\Delta\tau_{1,2}} \,, \end{aligned}$$

are the integration weights and $\Delta\tau_{1,2}$ is the optical depth difference between points 1 and 2. The derivatives of $S$ in (2.13) can be approximated by 2nd-order finite difference approximations,

$$\frac{\partial S}{\partial \tau}|_2 = \frac{(S_2 - S_3)(\Delta\tau_{1,2}/\Delta\tau_{2,3}) - (S_2 - S_1)(\Delta\tau_{2,3}/\Delta\tau_{1,2})}{\Delta\tau_{1,2} + \Delta\tau_{2,3}} \,, \tag{2.15}$$

$$\frac{1}{2}\frac{\partial^2 S}{\partial \tau^2}|_2 = \frac{(S_3 - S_2)/\Delta\tau_{2,3} + (S_1 - S_2)/\Delta\tau_{1,2}}{\Delta\tau_{1,2} + \Delta\tau_{2,3}} \,, \tag{2.16}$$

where $\Delta\tau_{2,3}$ is the optical depth difference between points 2 and 3.

Equation (2.14) may also be written as

$$I_2 = I_1 \, e^{-\Delta\tau_{1,2}} + \alpha S_1 + \beta S_2 + \gamma S_3 \,, \tag{2.17}$$

where (cf. Kunasz & Auer 1988)

$$\alpha = x + \frac{z - y(\Delta\tau_{2,3} + 2\Delta\tau_{1,2})}{\Delta\tau_{1,2}(\Delta\tau_{1,2} + \Delta\tau_{2,3})} \,,$$

$$\beta = \frac{y(\Delta\tau_{1,2} + \Delta\tau_{2,3}) - z}{\Delta\tau_{1,2}\Delta\tau_{2,3}},$$

$$\gamma = \frac{z - y\Delta\tau_{1,2}}{\Delta\tau_{2,3}(\Delta\tau_{1,2} + \Delta\tau_{2,3})},$$

where

$$x = 1 - \exp(-\Delta\tau_{1,2}),$$

$$y = \Delta\tau_{1,2} - x,$$

$$z = (\Delta\tau_{1,2})^2 - 2y.$$

As follows from equation (2.9), the diagonal part of the (frequency- and angle-dependent) elementary $\Lambda^*$-operator is given by the coefficient $\beta$. The integrated $\Lambda^*$ operator corresponding to the mean intensity, $J_\nu$, or the frequency-averaged mean intensity, $\bar{J}$, is evaluated by integrating the individual coefficients $\beta$ (that depend on frequency and angle) over angles and frequencies, respectively.

Strictly speaking, in order to get the exact diagonal elements it does not suffice to take only the $\beta$-coefficient of equation (2.17). This is because if we take a unit pulse at point 2, then the ensuing $I_1$ intensity (which should be taken into account in order to end up with the exact diagonal) is *negative*. If this negative contribution is neglected, one ends up with an overestimation of the diagonal elements which could potentially be numerically unstable (we are indebted to the referee for pointing this out to us). Nevertheless, in practice it turns out to be quite safe to neglect this negative contribution to the $\Lambda^*$-operator. This may be because the contribution decreases exponentially with increasing $\Delta\tau_{1,2}$, so that it is always small compared to the other contributions in optically thick situations, where acceleration is important. In fact, for $\Delta\tau_{1,2} > 25$, the contribution is generally smaller than the numerical accuracy of a double precision floating point number. Moreover, neglecting this contribution only introduces an error in a quantity that amplifies *corrections* to the source function and not in the source function itself, so that the final solution is not affected by it. We therefore use the approximate operator given by the $\beta$-coefficient.

The optical depth increments $\Delta\tau_{1,2}$ and $\Delta\tau_{2,3}$ are evaluated by integrating $\exp(\ln\chi(s))$ along the path $s$, where $\ln\chi(s)$ is a linear approximation to the natural logarithm of the opacity along $s$.

### 2.3.2 Treatment of Velocity Fields

In the previous section, we have assumed a static medium. This simplifies the integration and interpolation processes considerably, since all quantities

can be evaluated at a single frequency. However, in most actual situations velocities cannot be neglected. In principle, the short-characteristics method described above may be used even in the presence of velocity fields. However, if significant velocity gradients are present, it is quite possible that a straightforward application of the method may miss a significant fraction of the opacity at a given frequency. For instance, if the frequency under consideration is just outside a strong spectral line, and the velocity difference between points 1 and 2 in Figure 2.1 is large enough that this frequency is Doppler shifted to the other side of the line in point 1, a straightforward interpolation may underestimate the opacity along the ray by several orders of magnitude.

It is therefore important to implement an efficient method that will detect these cases and treat velocities correctly, regardless of the magnitude of the velocity gradient. A straightforward way to handle this problem is to put additional, "subgrid", points on the ray within the cell so that the velocity difference between any two subgrid points is always small compared to the thermal velocity. However, this means that we face additional spatial interpolations to obtain values of $S_\nu$, $\chi_\nu$, and the projected relative velocity, at all the subgrid points on the ray. The costs of calculating the formal solution thus increases considerably. Once the points are set up on the ray and the values in the points are calculated, integration of all quantities proceeds as in a 1-D problem.

## 2.4 Implementation: Description of the Code

The code presented in this paper aims to provide an efficient 2-dimensional, two-level atom solver to be used as the central engine in a more sophisticated spectral synthesis context. It incorporates all three standard geometries (Cartesian, cylindrical and spherical) in a transparent way, while allowing for arbitrary (3-dimensional) velocity fields, as required for general applicability in realistic astrophysical situations.

### 2.4.1 General Approach

The code uses a locally-comoving-frame approach, where the velocity at the grid point under consideration is taken to be zero. This is *not* equivalent to adopting the standard comoving-frame formulation (e.g., Mihalas 1978). In the present formulation, only the central point of a current short characteristic (point 2 in Figure 2.1) is at rest; all the other points on the short characteristic have generally a non-zero velocity.

To ensure a correct treatment of all three standard geometries, we have modularized the geometry-specific parts of the radiative transfer solver. This has the distinct advantage that it takes no more than changing an appropriate switch to change the geometry. To accomplish this, the calculations were split up in four separate stages; three of which involve geometry-specific details:

1. Finding the point where a short characteristic intersects with a grid boundary at the upwind side.
2. Setting a sampling of additional points along a short characteristic to ensure an accurate representation of variations of all quantities along the characteristic.
3. Calculating the intensity at the upwind end of the short characteristic. In the case of curved coordinates with velocities, this involves spatial as well as angular and frequency interpolations. This has to be done as accurately as possible, because in optically thin situations the accuracy of the code depends almost exclusively on the accuracy with which the intensity is interpolated.

After these three steps, the problem is reduced to one-dimensional integrations that are identical for all geometries.

Along the set of formal solutions that yield the specific intensity, an elementary $\Lambda^*$ operator is also evaluated, and all the needed partial integrals over frequencies and angles (to obtain the mean intensity, and the integrated $\Lambda^*$) are evaluated and stored. We note that in the case of an equivalent-two-level atom with a background continuum, which is the case we consider here, equations (2.6) and (2.7) for the integrated approximate $\Lambda^*$-operator have to be generalized to read

$$\bar{\Lambda}^*(\mathbf{x}) = \oint (d\mathbf{n}/4\pi) \int_0^\infty d\nu \, \frac{\phi(\nu, \mathbf{n}, \mathbf{x})^2}{\phi(\nu, \mathbf{n}, \mathbf{x}) + r(\mathbf{x})} \Lambda^*(\nu, \mathbf{n}, \mathbf{x}) \,. \tag{2.18}$$

where $r$ is the ratio of the continuum opacity to the frequency-averaged line opacity [see also equations (2.39) and (2.40)].

## 2.4.2 Cartesian Coordinates

Cartesian coordinates are by far the easiest to treat. Since photons (in the absence of general relativistic effects) move along straight lines, this is also a "natural" coordinate system for the radiation. Nevertheless, this model,

although being two-dimensional, is still not very realistic, as it implies an infinitely stretched structure along one coordinate. This coordinate system is included essentially for completeness and for testing purposes. There are several existing codes for 2-D radiative transfer in planar geometry (MAM; Kunasz & Auer 1988); we have performed a comparison of our results with selected test cases computed by MAM – see §2.6.

However, Cartesian coordinates are very advantageous and useful in a general 3-D geometry.

#### 2.4.2.1 Finding the upwind endpoint

Finding the location of the first intersection of a short characteristic with a cell boundary is trivial. Since all coordinates are flat, there are only two possible cell boundaries to intersect for every quadrant of $\varphi$, as shown in Figure 2.2, right panel; the angles are defined in the left panel of Figure 2.2. Although the direction in which to spatially interpolate $S_\nu$, $\chi_\nu$ and $I_\nu(\varphi, \theta)$

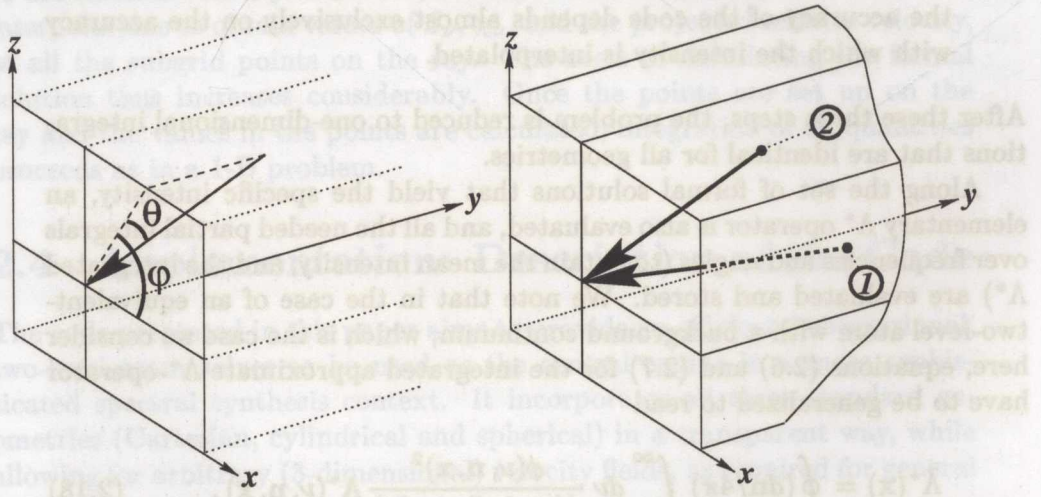


Figure 2.2: **Left panel:** *Definition of angles in Cartesian coordinates.* **Right panel:** *Different types of characteristics in Cartesian coordinates. In a projection to the $(x, z)$ plane, the type-1 characteristic corresponds to $1' \rightarrow 2'$ characteristic in Figure 2.1; and analogously type 2 corresponds to $1 \rightarrow 2$.*

to the upwind endpoint of the characteristic is dictated by the side with which the characteristic intersects (i.e., the type of the characteristic), the direction of computation across the grid is only dependent on the quadrant

of $\varphi$. This means that the only requirement for the grid is to be rectangular, but not necessarily regular.

#### 2.4.2.2 Interpolating the intensity

Typically, the angles at which the intensities are evaluated are chosen globally; i.e., the angles at all grid points are the same, and thus there is no need to interpolate in angle. However, in some applications it may be advantageous to choose different sets of angle points for different grid points. In such a case, it is necessary to interpolate in angles as well. In the present code, we have implemented a possibility of having different sets of angles at different grid points. However, setting angles by hand is extremely cumbersome; one thus needs some kind of adaptive-mesh treatment to automatically select angles. We postpone such a refinement to the future; in present applications we place angles where they are most likely needed based on simple assumptions regarding the radiation field.

### 2.4.3 Cylindrical Coordinates

Many astronomical objects have an essentially axially-symmetric structure. Typical examples are accretion disks, rotating stars, and other objects. For these applications, a 3-D Cartesian rectangular grid can be used but is rather inefficient, while 2-D cylindrical coordinates are more natural coordinates to the problem.

We have therefore implemented a radiative transfer solver that applies the method of short characteristics in cylindrical coordinates. This is nontrivial because the characteristics projected on the $(r, z)$ plane are not straight lines. Although the material properties can still be adequately represented by a 2-D rectangular grid, the radiative transfer has now a fully 3-D structure which has to be taken into account explicitly. An additional complication is that the velocity vector can now have a meaningful, non-negligible, third component. This requires that at every spatial point the integral of the intensity over angles has to be carried out over the full $(4\pi)$ solid angle, and with a sufficient resolution to represent all possible intensity variations accurately.

Additional complications arise from the curvature of the characteristics. This in turn leads to complications when calculating the intensity at the upwind end of the characteristic, as well as in determining the variation of quantities along the characteristic. The angles that specify the direction of a given characteristic at a given grid point may be quite different from

the angles with which the characteristic intersects the cell boundary; this feature makes the angular interpolations inevitable. Moreover, the value of any quantity along a ray that is strongly curved when projected onto the $(r, z)$ plane can be very different from that obtained by an interpolation that assumes a straight line.

### 2.4.3.1 Curved Characteristics

The $z$-axis is assumed to be the axis of symmetry, the angle $\phi$ in the coor-

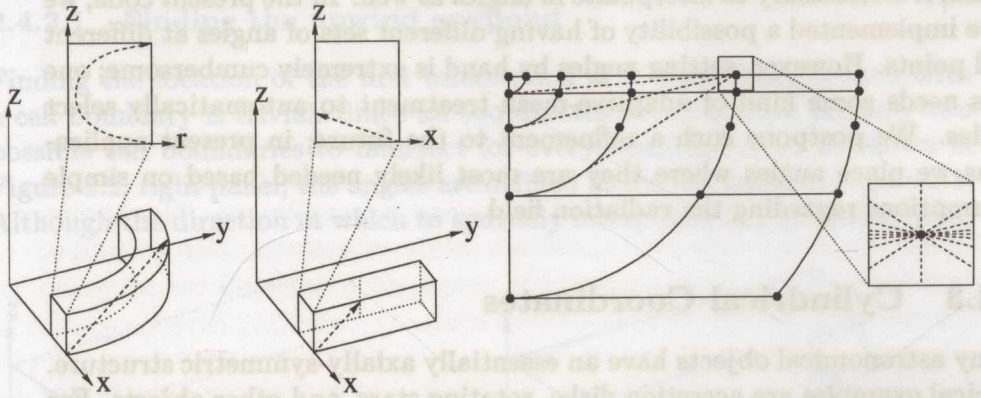


Figure 2.3: **Left panel:** *Projection of the $(x, y, z)$ value of a straight line on the $(x, z)$ plane in Cartesian coordinates is still a straight line. In curved coordinates the projection of the $(r, \phi, z)$ value of a straight line on the $(r, z)$ plane is curved.* **Right panel:** *Illustration of the tangent-ray method. The solid lines are the rays in which radiative transfer is calculated in plane geometry. By choosing a ray tangent to each cylinder going through any two points on the original ray, a substantial number of angles (dashed lines) can be calculated in plane geometry. The intensity never needs to be interpolated in angle.*

dinate system is defined counter-clockwise going from 0 to $2\pi$. There are several ways to take into account the curvature of a characteristic. One way is to use a "rotating-plane" method (e.g., Dullemond & Turolla 2000) – see Figure 2.3, left panel. Consider a point moving along a straight line in 3-D space. At every position of the point, construct a plane that goes through the point and the $z$-axis; when the point moves, the plane rotates about the $z$-axis. The curved characteristic is now a trajectory of the point in this plane. However, when general velocity fields are assumed, a polynomial approximation of several quantities has to be integrated along this

path, resulting in very complicated expressions.

Another way to solve the problem is to use the "tangent-plane" method, a 2-dimensional analogue of the tangent-ray method developed by Hummer & Rybicky (1971) – see Figure 2.3, right panel. In this case, all characteristics can be treated in plane geometry. The angular resolution is now determined by the number of radial grid points between any point and the $z$-axis. This results either in a poor angular resolution of the radiation intensity close to the $z$-axis, or necessitates the use of many angles where only a few angles would suffice. Furthermore, in the presence of velocities, the angles are determined by the spatial distribution of grid points and may thus be inappropriate for the problem at hand. Consequently, the most efficient choice of angles is impossible without altering the spatial distribution of grid points. However, perhaps the most serious problem is that the average radius of a ray tangent to a cylinder intersecting a larger cylinder is considerably smaller than the average of the two radii. This means that if the quantities along a tangent ray are assumed to vary from point to point as a function of the distance on the ray in the same way they vary as a function of radius, systematic interpolation errors are introduced.

Due to the above problems, there is no universally convenient way to formulate the short characteristic scheme in cylindrical coordinates. A practical way is to choose a method that provides the best compromise between computational speed and numerical accuracy. We have adopted the following procedure: To avoid complicated path integrals, the short characteristics are treated in Cartesian (flat) space, as in the tangent-ray method. In this case, all expressions remain simple, and their evaluation is fast. However, unlike the tangent-ray method, the angular sphere can be sampled arbitrarily, so that angles can be placed where they are needed. To integrate along the characteristics, we first evaluate the values of the curved coordinates for all the subgrid points. Then, we interpolate the values of all needed quantities along the characteristic in the curved coordinates, where all quantities are assumed to vary smoothly. This is essentially the same as integrating along a curved characteristic, but the complicated path-integral is replaced by a simple quadrature along a straight path.

#### 2.4.3.2 Finding the Upwind Endpoint

Before proceeding to calculating the endpoint of a ray it is practical to transform the angles as they are defined in the problem (Figure 2.4, left panel), to angles as they are defined in the cylindrical coordinate system. This can be most conveniently done by looking at Figure 2.4, right panel.

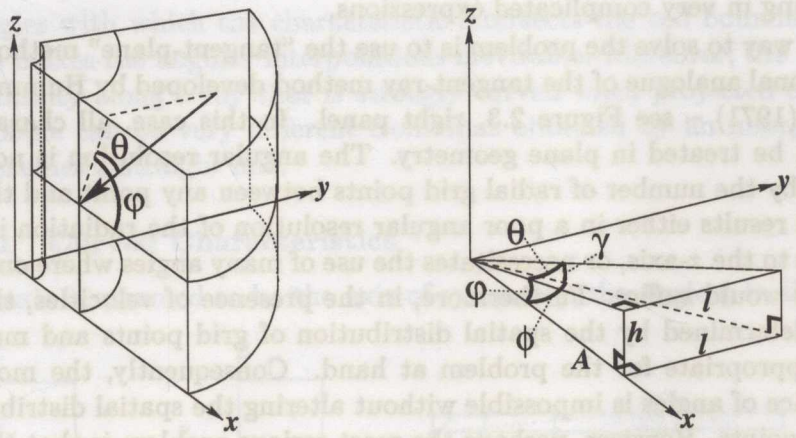


Figure 2.4: **Left panel:** *Definition of the "problem" angles in cylindrical coordinates.* **Right panel:** *Transforming the "problem" angles to the cylindrical coordinate angles (see the text for explanation).*

Expressing $l/A$ in terms of $\varphi$ and $\theta$, and in terms of $\phi$, we obtain

$$\tan\phi = \frac{l}{A} = \frac{\tan\theta}{\cos\varphi}\,, \tag{2.19}$$

so that

$$\phi = \arctan\left(\frac{\tan\theta}{\cos\varphi}\right)\,, \tag{2.20}$$

and similarly

$$\gamma = \arcsin(\cos\theta\sin\varphi)\,, \quad \varphi = \arctan\left(\frac{\tan\gamma}{\cos\phi}\right)\,, \quad \theta = \arcsin(\cos\gamma\sin\phi)\,. \tag{2.21}$$

All angles can thus be easily expressed through one another.

The maximum length of the characteristic projected onto the $x$-$y$ plane, $\Delta R_{\rm max}$, can now easily be found for a given angle $(\phi, \gamma)$ from the projection of the situation on the $x$-$y$ plane - see Figure 2.5 - left panel. By taking the radius of arrival $R_{\rm arr}$, the radius of departure $R_{\rm dep}$, the arrival angle $\phi$, and applying the cosine rule we get

$$R_{\rm dep}^2 = R_{\rm arr}^2 + \Delta R_{\rm max}^2 - 2R_{\rm arr}\Delta R_{\rm max}\cos(\pi - \phi)\,, \tag{2.22}$$

so that $\Delta R_{\rm max}$ may be expressed as

$$\Delta R_{\rm max} = -R_{\rm arr}\cos\phi \pm \sqrt{R_{\rm dep}^2 - R_{\rm arr}^2\sin^2\phi}\,. \tag{2.23}$$

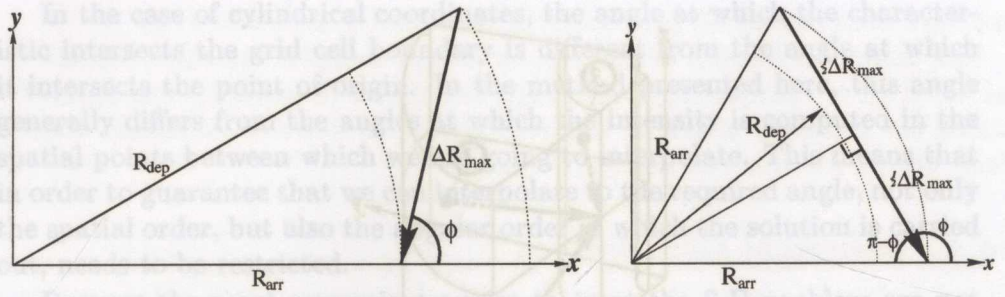


Figure 2.5: **Left panel:** $\Delta R_{\max}$ *can be calculated from this projected situation in the x-y plane.* **Right panel:** *Determining the minimum radius reached by a characteristic.*

For "inward" characteristics ($0 \leq \phi \leq \pi/2$ and $3\pi/2 \leq \phi < 2\pi$), the root is always real as $R_{\rm arr} \leq R_{\rm dep}$, and the positive root solution clearly needs to be taken, as $\Delta R$ has to be positive. The negative root solution refers to the *downwind* intersection point with the cylinder with $R = R_{\rm dep}$.

For "outward" characteristics ($\pi/2 < \phi < 3\pi/2$), either both the positive and negative root give positive solutions, or the root is imaginary as $R_{\rm dep} \leq R_{\rm arr} \mid \sin\phi \mid$. If the root is real the characteristic reaches $R = R_{\rm dep}$ twice, where the "plus" solution refers to the distance where the characteristic enters, and the "minus" solution refers to the distance where it leaves the interior of the cylinder with $R = R_{\rm dep}$ (the latter is the value of interest). If the root is imaginary, the characteristic never reaches the radius $R = R_{\rm dep}$ and in fact intersects the cylinder with $R = R_{\rm arr}$ – see Figure 2.5, right panel. In that case the value of $\Delta R$ can be calculated from

$$\Delta R_{\max} = 2R_{\rm arr}\cos(\pi - \phi) = -2R_{\rm arr}\cos\phi\,, \tag{2.24}$$

corresponding to case 3 in Figure 2.6. Once $\Delta R_{\max}$ is known, $\Delta z_{\max}$ can be calculated from

$$\Delta z_{\max} = \Delta R_{\max}\tan\gamma\,, \tag{2.25}$$

corresponding to case 1 in Figure 2.6. In case the cell we are considering has a vertical extent $\Delta z < \Delta z_{\max}$, the ray is terminated before it reaches $\Delta R_{\max}$ and the length of the projection in the $x$-$y$ plane can be calculated from

$$\Delta R_{\max} = \frac{\Delta z}{\tan\gamma}\,, \tag{2.26}$$

corresponding to case 2 in Figure 2.6.

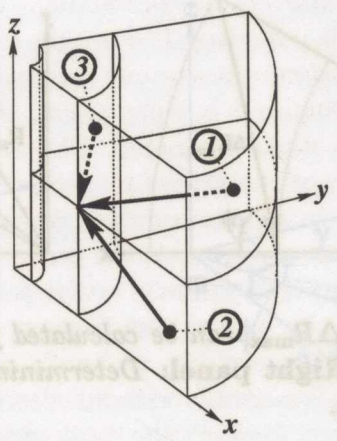


Figure 2.6: *Different types of characteristics in cylindrical coordinates.*

#### 2.4.3.3 Integration along the Short Characteristic

Once the upwind endpoint is found, the rest of the process is straightforward. The middle position on the ray between the beginning and endpoints is found by taking the average of the Cartesian coordinates of the two points. From these the cylindrical coordinates of this point are then derived at which the value of all quantities is subsequently calculated. All values except that of the projected relative velocity are taken to be independent of $\phi$ (because of cylindrical symmetry).

If the interpolated values of all quantities differ from the values derived from interpolating between the points already on the ray by less than a small fraction (typically 5%), the resolution is considered adequate. Otherwise, another point is added to the ray between the new point and the previous one and the process is repeated. In addition, it is mandatory to require that the difference in the projected relative velocity between any two points on the characteristic is significantly smaller than one thermal Doppler width, otherwise, one can easily introduce large errors in the opacity, as explained in § 2.3.2.

#### 2.4.3.4 Interpolation of the Intensity

We now need to calculate the intensity at the upwind end of the characteristic in order to evaluate the intensity from equation (2.11). The easiest way to obtain this information is by interpolating the intensity from grid points closest to the upwind end of the characteristic.

In the case of cylindrical coordinates, the angle at which the characteristic intersects the grid cell boundary is different from the angle at which it intersects the point of origin. In the method presented here, this angle generally differs from the angles at which the intensity is computed in the spatial points between which we are going to interpolate. This means that in order to guarantee that we can interpolate to the required angle, not only the spatial order, but also the angular order in which the solution is carried out, needs to be restricted.

Because the most convenient angles to treat the 2-D problem are not necessarily convenient for the problem in 3-D, the definition of angles is such that $0 \leq \varphi < 2\pi$, whereas $-\pi/2 \leq \theta \leq \pi/2$ (see also Figure 2.4 - left panel). Unfortunately this is not the best choice of angles for a cylindrical coordinate system, because in general they both change. However, once we transform our angles to a local cylindrical coordinate system by means of equations (2.20) and (2.21), it becomes immediately clear – see Figure 2.7, that only one angle, $\phi$, changes. Moreover, $\phi$ changes in such a way that the

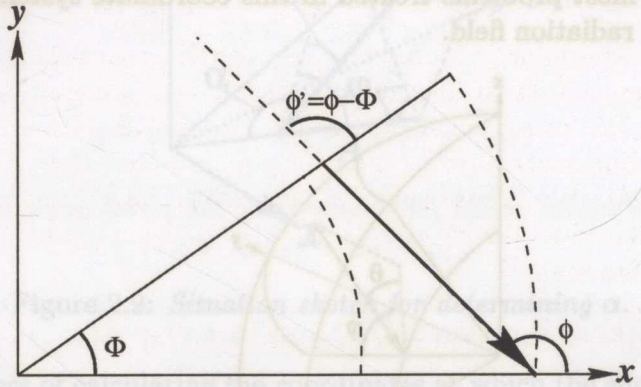


Figure 2.7: *Change of angle $\phi$ in cylindrical coordinates. $\gamma$ is in the r-z plane only and therefore does not change.*

angle at which we need to know the intensity is always smaller than the one we are calculating. Indeed, by calculating the intensity in a fixed angular order, the intensity is guaranteed to be calculated before it is needed and there are no causality problems, such as those reported by Dullemond & Turolla (2000) for spherical geometry.

Even in case 3 in Figure 2.6, where interpolating the intensity in the point of intersection involves intensities at the same spatial point we are calculating the intensity at, we are guaranteed that the angle is smaller than the one we are calculating, so that we can interpolate it from values

that have been calculated previously, provided we include $\theta = \pi/2$.

The unavoidable result of the angular interpolations is increased numerical diffusion of the intensity. Although the effects in astrophysical applications are generally speaking relatively small, in extreme situations the effects on the solution can be clearly seen.

### 2.4.4 Spherical Coordinates

Spherical coordinates are obviously suitable for spherical or near-spherical objects. However, the fact that two out of three coordinates are curved makes this system rather awkward for solving the transfer problem. Since the grid itself is now curved, special situations, like symmetric boundary conditions, become more difficult to handle. The definition of the angles in spherical coordinates was chosen to be local, i.e. the angle $(\varphi, \theta) = (0, 0)$ is set up to point radially inward – see Figure 2.8. This was found preferable over a global definition adopted for the Cartesian and the cylindrical coordinates, because most problems treated in this coordinate system have an essentially radial radiation field.

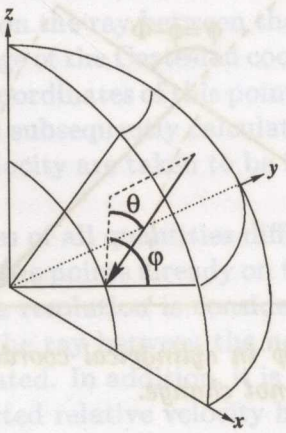


Figure 2.8: *Definition of angles in spherical coordinates.*

#### 2.4.4.1 Finding the Upwind Endpoint

Finding the endpoint of a characteristic in spherical coordinates involves not only the arrival angles, the size of the grid box, and the radii of the grid points, it is now also necessary to consider the grid coordinate angle, $\Theta$ (in the global coordinate system) of the grid points under consideration.

To determine which of the grid cell boundaries the given characteristic intersects is now more complicated than in cylindrical coordinates, as there are now two curved coordinates instead of only one. This means that where the angles $(\varphi, \theta = \pi/2)$ only needed to be considered "inward" in cylindrical coordinates, $\varphi$ now needs to be considered in quadrant 4 for $\Theta > 0$ and in quadrant 1 for $\Theta < 0$ due to the curvature of the second coordinate. Since the code is currently limited to handle $\Theta > 0$, all angles $(\varphi, \theta = \pi/2)$ are always considered to have $\varphi$ in quadrant 4. The grid points $(r, \Theta = \pi/2)$ are a special case that needs to be treated separately, as all characteristics with angles $(\phi, \gamma)$ map onto the same angle for all values of $\phi$ due to the rotational symmetry around the $z$-axis.

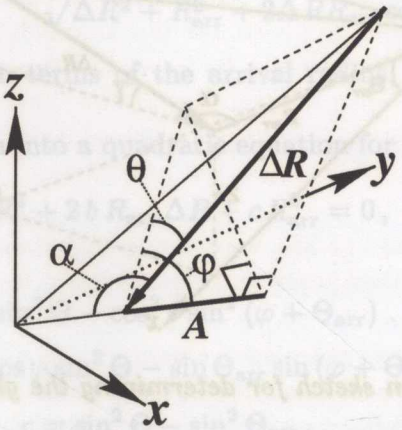


Figure 2.9: *Situation sketch for determining* $\alpha$.

The process of calculating the coordinates at which the short characteristic terminates can be split in several steps. First a useful auxiliary angle, $\alpha$, is calculated. Given a generic situation as in Figure 2.9 with given values of $\varphi$ and $\theta$, we can express $A$ in terms of $\Delta R$, $\varphi$ and $\theta$, viz.

$$A = \Delta R \cos\theta \cos\varphi \,, \tag{2.27}$$

and in terms of $\alpha$,

$$A = \Delta R \cos(\pi - \alpha) = -\Delta R \cos(\alpha) \,, \tag{2.28}$$

so that

$$\alpha = \arccos(-\cos\varphi \cos\theta) \,. \tag{2.29}$$

Analogously to the case of cylindrical coordinates, the spherical radial coordinate, $r$, can now be calculated as a function of the length of the characteristic, $\Delta R$, using the cosine rule – see Figure 2.10,

$$\begin{aligned} r(\Delta R) &= \sqrt{\Delta R^2 + R_{\text{arr}}^2 - 2\Delta R\, R_{\text{arr}} \cos\alpha} \\ &= \sqrt{\Delta R^2 + R_{\text{arr}}^2 + 2\Delta R\, R_{\text{arr}} \cos\varphi \cos\theta}\,, \end{aligned} \tag{2.30}$$

where only the positive root needs to be considered since $r$ must be positive. Inversely we can solve for $\Delta R$ as a function of $r$ which gives the two

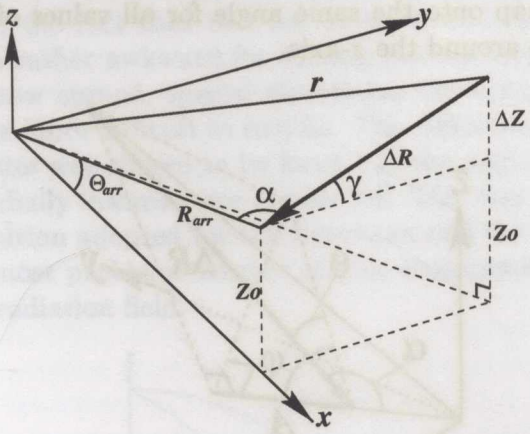


Figure 2.10: *Situation sketch for determining the global angle* $\Theta(\Delta R)$.

solutions,

$$\Delta R(r) = R_{\text{arr}} \cos\alpha \pm \sqrt{R_{\text{arr}}^2 \cos^2\alpha + r^2 - R_{\text{arr}}^2}\,. \tag{2.31}$$

It is now trivial to calculate the smallest positive value of $\Delta R(R_{\text{dep}})$ as in cylindrical coordinates, giving three different types of characteristics according to where they originate.

To determine whether the characteristic is limited by a cell boundary in $\Theta$ is less trivial than to determine whether it is limited by a cell boundary in $z$, since merely determining that the $\Theta$ value of the endpoint for a given $\Delta R_{\max}$ is within the $\Theta$ limits of the cell is not sufficient to exclude an earlier intersection with a cell boundary, since $\Theta$ is a curved coordinate. For this we need to calculate the smallest positive value of $\Delta R(\Theta)$ as was necessary for $\Delta R(r)$.

From Figure 2.10 we see that the $z$-coordinate of the endpoint of the given characteristic as a function of $\Delta R$ is given by

$$z(\Delta R) = z_0 + dZ = Z_0 + \Delta R \sin\gamma\,, \tag{2.32}$$

where $\gamma$ is the angle between the ray and the $x$-$y$ plane, which is indeed equal to the transformed angle $\gamma$ from (2.20) and (2.21), but with $\varphi \to \varphi + \Theta_{\text{arr}}$, where $\Theta_{\text{arr}}$ is the grid coordinate angle of the grid point under consideration. We can therefore write

$$z(\Delta R) = Z_0 + \Delta R \sin(\varphi + \Theta_{\text{arr}}) \cos\theta \,. \tag{2.33}$$

The coordinate angle $\Theta(\Delta R)$ as a function of $\Delta R$ can now be expressed in terms of $z(\Delta R)$ from equation (2.33), and $r(\Delta R)$ [from equation (2.30)], given $\theta$, $\varphi$, $R_{\text{arr}}$ and $\Theta_{\text{arr}}$,

$$\sin\Theta(\Delta R) = \frac{z(\Delta R)}{r(\Delta R)} = \frac{R_{\text{arr}} \sin\Theta_{\text{arr}} + \Delta R \sin(\varphi + \Theta_{\text{arr}}) \cos\theta}{\sqrt{\Delta R^2 + R_{\text{arr}}^2 + 2\Delta R R_{\text{arr}} \cos\varphi \cos\theta}} \,, \tag{2.34}$$

where $Z_0$ is expressed in terms of the arrival radius, $R_{\text{arr}}$, and the grid coordinate angle, $\Theta_{\text{arr}}$.

This can be rewritten into a quadratic equation for $\Delta R(\Theta)$,

$$a\,\Delta R^2 + 2\,b\,R_{\text{arr}}\,\Delta R + c\,R_{\text{arr}}^2 = 0 \,, \tag{2.35}$$

where

$$a = \sin^2\Theta - \cos^2\theta \sin^2(\varphi + \Theta_{\text{arr}}) \,.$$

$$b = \cos\theta \left[\cos\varphi \sin^2\Theta - \sin\Theta_{\text{arr}} \sin(\varphi + \Theta_{\text{arr}})\right] \,,$$

$$c = \sin^2\Theta - \sin^2\Theta_{\text{arr}} \,,$$

which has the explicit solution

$$\Delta R(\Theta) = \frac{R_{\text{arr}}}{a} \left[-b \pm \sqrt{\sin^2\Theta \left[(\sin^2\varphi \cos^2\Theta_{\text{arr}} - c\cos^2\varphi)\cos^2\theta + c\right]}\right] \,. \tag{2.36}$$

For the characteristics limited by the value of $\Theta$ they arrive on (i.e. the characteristics limited by the cell boundary $\Theta = \Theta_{\text{arr}}$, case 3 and 4 in Figure 2.11), this expression can be written as a linear equation for $\Delta R$,

$$\begin{aligned} &\left[\sin^2\Theta_{\text{arr}} - \cos^2\theta \sin^2(\varphi + \Theta_{\text{arr}})\right] \Delta R + \\ &2R_{\text{arr}} \left[\cos\theta \cos\varphi \sin^2\Theta_{\text{arr}} - \cos\theta \sin\Theta_{\text{arr}} \sin(\varphi + \Theta_{\text{arr}})\right] = 0',, \end{aligned} \tag{2.37}$$

since the solution $\Delta R = 0$ is trivial. This can be simplified to

$$\begin{aligned} \Delta R &= -2R_{\text{arr}} \frac{\cos\theta \sin\Theta_{\text{arr}} [\cos\varphi \sin\Theta_{\text{arr}} - \sin(\varphi + \Theta_{\text{arr}})]}{\sin^2\Theta_{\text{arr}} - \cos^2\theta \sin^2(\varphi + \Theta_{\text{arr}})} \\ &= R_{\text{arr}} \frac{\cos\theta \sin\varphi \sin 2\Theta_{\text{arr}}}{\sin^2\Theta_{\text{arr}} - \cos^2\theta \sin^2(\varphi + \Theta_{\text{arr}})} \,. \end{aligned} \tag{2.38}$$

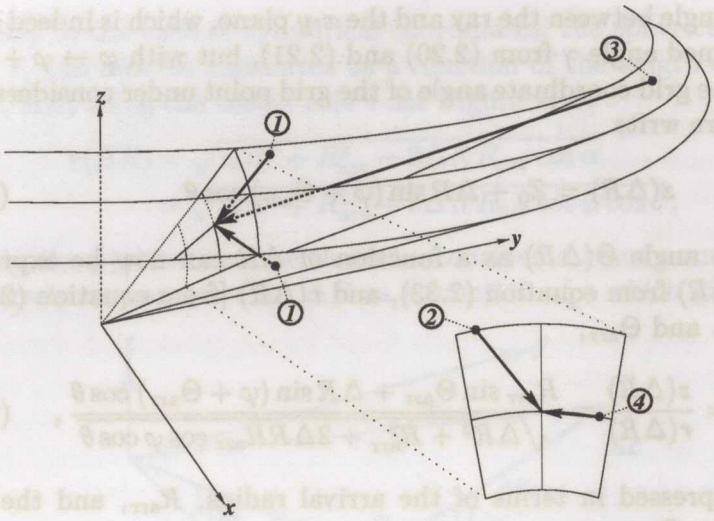


Figure 2.11: *Different types of characteristics in spherical coordinates.*

Using equations (2.36) and (2.38), we can now calculate the smallest positive $\Delta R(\Theta_{\text{dep}})$, i.e. the smallest positive, nonzero value for $\Delta R$ limited by $\Theta_{\text{dep}}$ and $\Theta_{\text{arr}}$.

From the four solutions calculated above, the smallest, positive, nonzero $\Delta R$ larger than 0 indicates the first *upwind* point of intersection with a cell boundary. Given $\Delta R$, $\varphi$ and $\theta$ it is now straightforward to calculate the Cartesian displacements $\Delta x$, $\Delta y$ and $\Delta z$ and from these the system coordinates $r$, $\Theta$ and $\Phi$.

In general, it is not only necessary to store the coordinate values of the endpoint, but also the type of characteristic that it belongs to. This information is vital in determining the grid points to be used in the spatial interpolation of the intensity.

### 2.4.4.2 Interpolation of the Intensity

To calculate the angles at which we need to calculate the incoming intensity at the end of the characteristic, we start by computing the transformed angles $\phi$ and $\gamma$ from (2.20) and (2.21) with $\varphi \rightarrow \varphi + \Theta_{\text{arr}}$ at the point of arrival – see Figures 2.12 and 2.4, right. By rotating the grid-plane around the $z$-axis to the departure angle $\Phi_{\text{dep}}$, $\phi$ changes to $\phi' = \phi - \Phi_{\text{dep}}$ while $\gamma$ does not change. We can now convert back to local coordinates using (2.20) and (2.21) and $\varphi' + \Theta_{\text{dep}} \rightarrow \varphi'$ to arrive at $(\varphi', \theta')$, the desired local angles

at which to interpolate the intensity. The angle $(\varphi',\theta')$ obtained in this way is strictly local, so that there are two ways to proceed.

The first one is to blindly use this angle to interpolate the intensity in angle in the closest spatial points – see Figure 2.13, middle. This seems

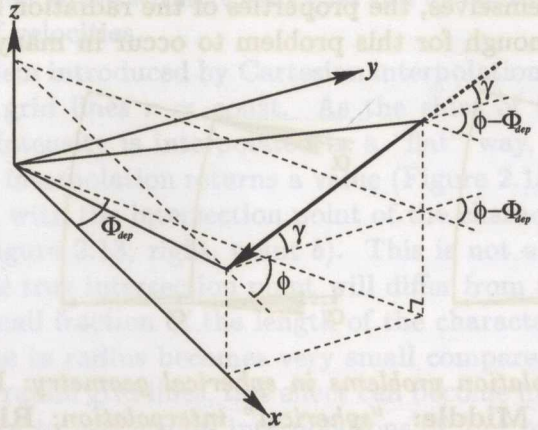


Figure 2.12: *Angle conversion from departure angles to arrival angles.*

to be reasonable in spherical coordinates, as all quantities are assumed to behave in a more or less "spherical" way. There is, however, no guarantee that the radiation will behave similarly, as its natural coordinate system is Cartesian. If the radiation field is strongly non-spherical, as in disk or jet problems, this method is therefore not the best one to use. One advantage of the "spherical" interpolation method is that it is never necessary to include the intensity being calculated in the intensity interpolation, as long as the angle $(\varphi,\pi/2)$ is included in the angular grid. In that case the intensity on an outward ray will always need to be computed at an inward angle if it curves back on itself, so that there are no complications.

The second one is to interpolate in the Cartesian coordinates, by adjusting the angles in which to interpolate so that the angles in all spatial points used for interpolation are parallel (see Figure 2.13, left). Although for general radiation fields this may be the correct solution, for radiation fields in central object problems, where the radiation field becomes more radially peaked with distance from the central object, this method can give very large interpolation errors. This can be easily understood, as in the spherical coordinates the geometrical distance between grid points with the same radius increases with radius. The distance between two parallel characteristics going through neighboring grid points therefore also increases with radius, so that there is always a radius where the separation between

the two is larger than the size of the source object. This means the smooth variation condition needed to interpolate accurately may break down when one characteristic probes a source region but the next one does not. Although the characteristics are short, and are thus unlikely to actually probe the source region themselves, the properties of the radiation field are propagated accurately enough for this problem to occur in many situations of

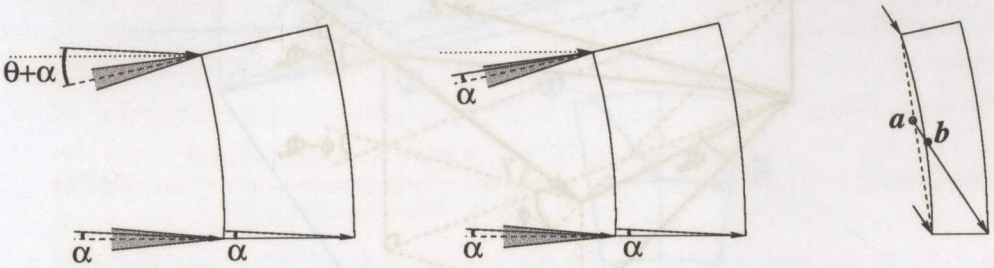


Figure 2.13: *Interpolation problems in spherical geometry:* **Left:** *"Cartesian" interpolation;* **Middle:** *"spherical" interpolation;* **Right:** *"Cartesian" interpolation location error.*

interest. This problem does not exist in rectangular coordinate systems (Cartesian, cylindrical), since the coordinates do not converge and the angular separation of two grid points as seen from the origin decreases with distance to the origin.

Since in the spherical coordinate system some characteristics curve back toward their point of origin (cases 3 and 4 in Figure 2.11), a "Cartesian" interpolation introduces the possibility that the interpolation of the intensity at the upwind endpoint involves the intensity we are trying to calculate in the first place. To avoid undefined values in this process, the angular order in which the intensities are calculated should be such that all intensity values but the one that is being calculated are calculated before. If this can be done, even in the case the intensity being calculated is needed in the interpolation, it can still be solved explicitly. A close look at the formal solution of the radiative transfer equation reveals that as the only contribution of the intensity calculated is in $I_0$, we can simply calculate the contribution of this intensity to $I_0$ and bring that term to the left hand side. The system is then fully determined and can be solved without any problems, provided that $\tau > 0$. Although this method can result in poorly determined intensities in optically thin regions, it does not require the Extended Short Characteristics method developed by Dullemond & Turolla (2000). This means that we do not need an extra row of cells on the boundaries to complete the extended part of the characteristic, which is helpful

when adopting a spatial parallelization. Since general velocities are allowed, not only the angular order in which the intensities are calculated needs to be fixed, also the frequency order may need to be restricted. This can actually be helpful when interpolating, since many cases that needed to be treated specially as outlined above without velocities can be considered "normally" in the presence of velocities.

Another problem introduced by Cartesian interpolation is related to the curvature of the grid lines $r = \text{const}$. As the sides of the grid cell are curved, and the intensity is interpolated in a "flat" way, the location for which the spatial interpolation returns a value (Figure 2.13, right, point $a$) does not coincide with the intersection point of the characteristic with the cell boundary (Figure 2.13, right, point $b$). This is not a real problem in most cases, as the true intersection point will differ from the assumed one only by a very small fraction of the length of the characteristic. However, when the step size in radius becomes very small compared to the angular separation of two radial grid lines, this effect can become important. In this case it is necessary to use surface interpolations of four or more points to calculate the intensity value in the correct location.

In general, the problem at hand dictates which one of these possibilities to use, but there will be cases where a choice is difficult to make. A general solution would involve tracing the origin of the intensity at a specific angle and matching it up with intensity from the same region in the other spatial points (for instance by means of a least squares comparison of the intensity in the two points). From this, a dependence of the intensity on angle as a function of grid coordinate can be estimated, and from that the correct angles to interpolate at can be deduced.

## 2.5 Parallel Implementation

To enhance the performance of the code, it is desirable to parallelize it in some way so that a large number of processors can be used to solve the problem. The parallelization is not only useful as it increases the speed of the solver, but becomes absolutely necessary for very large problems (many spatial, frequency, and/or angular grid points), which would otherwise require excessive amounts of memory per processor.

However, there is no obvious way of splitting the tasks, as the radiative transfer is non-local and all the grid points in principle communicate with all other grid points. Furthermore, since multi-CPU supercomputers are expensive, while networked PC clusters are becoming more commonly

available, an ideal method of parallelization should not rely heavily on fast communications. This last requirement limits the type of quantity that is to be exchanged. Communicating any quantity that depends on all variables (space, angle, and frequency) will generate very large data streams, and will thus dominate the total execution time. Therefore, communicating appropriately selected *integrated* quantities is much more efficient.

In this light, parallelizing in frequency does not seem to be a practical choice. To calculate the frequency-averaged mean intensity, $\bar{J}(\mathbf{x})$, for a single line, the individual frequency-dependent mean intensities, $J_\nu(\mathbf{x})$, need to be collected in one or several central places, where the integration to obtain $\bar{J}(\mathbf{x})$ is performed. This can easily result in one or a few overloaded processors that dominate the execution time. Furthermore, $\bar{J}(\mathbf{x})$ has then to be redistributed among all processors. A similar problem occurs when parallelizing in angle, because in order to compute $\bar{J}(\mathbf{x})$ we now need to communicate $I_\nu(\mathbf{x}, \mathbf{n})$ from all processors to all other processors.

We are thus left with a spatial parallelization, which promises to reduce the amount of communication because $I_\nu(\mathbf{x}, \mathbf{n})$ needs to be communicated only between spatial points that are shared by more than one processor. The relatively low cost of communication is due to the fact that communication is now only required between processors calculating spatially adjacent parts of the problem, and is thus essentially local.

### 2.5.1 Spatial parallelization

Spatial parallelization is done by dividing the total computational domain in a number of *sub-domains*, each of which contains a significant number of individual grid points – see Figure 2.14. The boundary of each sub-domain is shared with another sub-domain, so that for all points the intensity across the whole angular sphere can either be calculated or is specified by boundary conditions. Sharing a single point between two or more sub-domains was chosen over having an extra row of inactive grid points around all sub-domains, since the latter requires more memory.

Because communication among sub-domains is now local, the non-local nature of the radiation field has to be taken into account iteratively. Starting with an initial guess for the incoming intensities on these boundaries, a formal solution in the sub-domains is calculated completely independently. The resulting intensities in the boundary points are then communicated, resulting in improved boundary conditions in the next formal solution.

Even though at first glance it may seem to be a very poor approximation to regard subproblems of a non-local problem as local, the method

converges almost as fast as the fully non-local problem in a single computational domain. This surprising behavior can be explained as follows. Roughly speaking, in a typical astrophysical problem there are two fundamental regions, the source region, and an optically thin envelope. The source region is usually optically thick, and thus the local approximation holds. The radiation in the optically thin regions primarily originates in the source region, and so only a few iterations are required to propagate the information through all the optically thin sub-domains once the source region

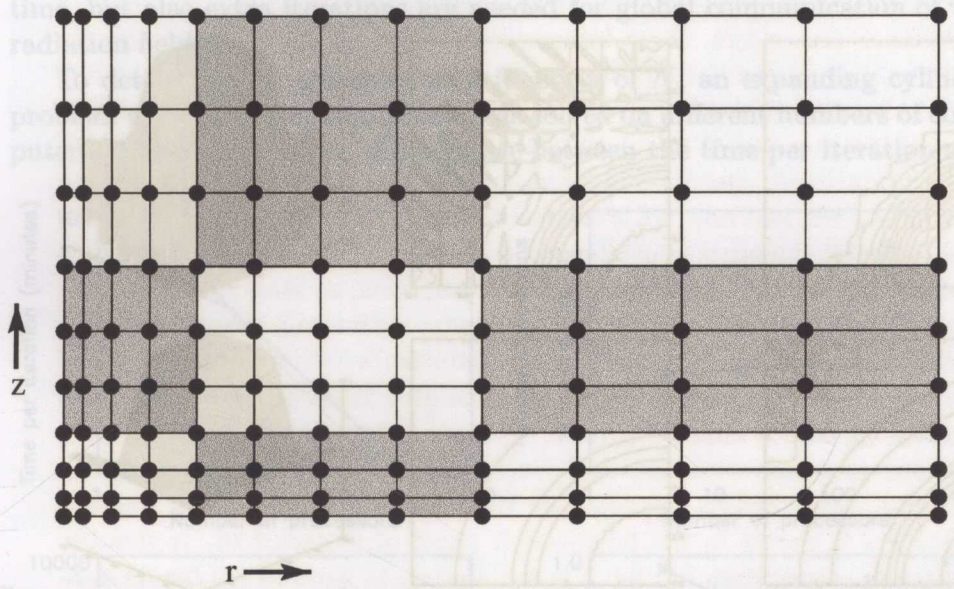


Figure 2.14: *Schematic example of a division of the total domain into sub-domains. The parts with different filling pattern indicate different sub-domains.*

has converged. This is illustrated in Figure 2.15, where the source function for an expanding cylinder is plotted after progressively larger number of iterations.

### 2.5.2 Acceleration

To accelerate the iteration process, the usual Ng acceleration is applied. However, one needs to be careful about the boundaries of the sub-domains. All the global features of the problem are essentially stored in the sub-domain boundaries. Therefore, accelerating only the local source function and not the boundary intensities would be inefficient, because in the next

iteration all the non-locally dominated sub-domains would return to the situation of the previous ALI iteration. Instead, it is most effective to create acceleration coefficients not only from the convergence record of the source function, but also from that of the boundary intensities.

As usual, there is a price to be paid. In this case the boundary intensities need to be stored up to three iterations back to enable acceleration. This increases the memory requirements considerably, especially if the sub-domains that are used are very small so that a large fraction of the points

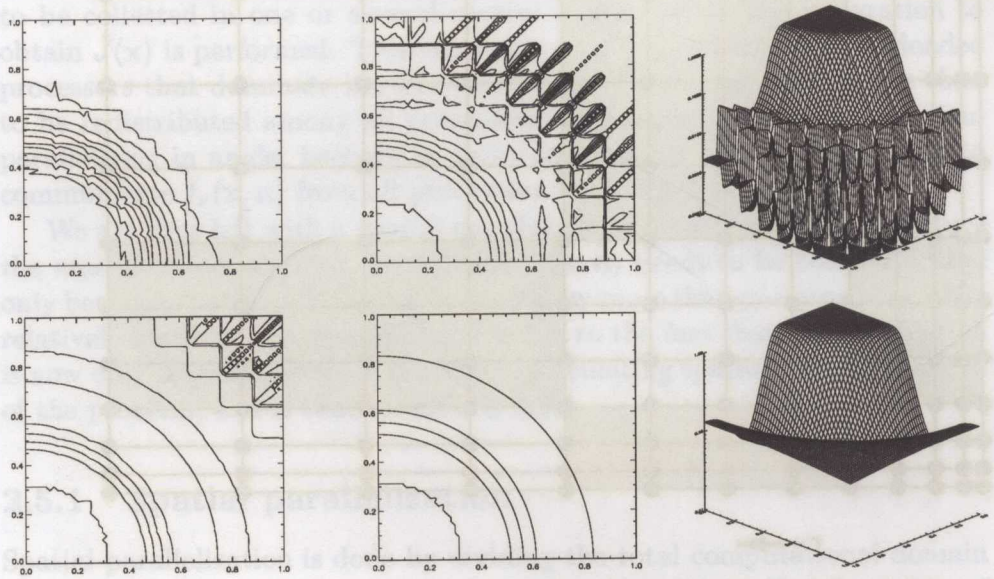

Figure 2.15: *Example of the convergence of a solution on 64 sub-domains. Four panels on the left display the source function as a surface plot, from left to right and from top to bottom, starting at the upper left, for iterations 1, 4, 8, and 29 (final); the two panels on the right display the source function as a 2-D plot after the 5th iteration (top), and 29th iteration (bottom). The adopted physical model is a line formation in a two-level atom with* $\epsilon = 10^{-4}$, $B = 1$, *in an expanding cylinder in Cartesian coordinates – see also § 2.6.1.4.*

lie on the boundaries. Also, once the source function is determined, it is not easily possible to resume the calculations from that point on, since the matching boundary conditions are no longer available and need to be calculated again.

### 2.5.3 Efficiency

The efficiency of the method is defined here as the time it takes to calculate the problem on a single CPU divided by $N$ times the time it takes to calculate it on $N$ CPUs. This is almost never equal to 1, but it can be close to 1 for well parallelized problems. In general, however, it depends on $N$ as well as on the problem under consideration. The efficiency of a spatially parallelized radiative transfer solver must obviously be lower than 1, because not only the communication of boundary intensities takes extra time, but also extra iterations are needed for global communication of the radiation field.

To determine the efficiency as a function of $N$, an expanding cylinder problem with $64 \times 64$ spatial points was solved on different numbers of computers. It is instructive to differentiate between the time per iteration and

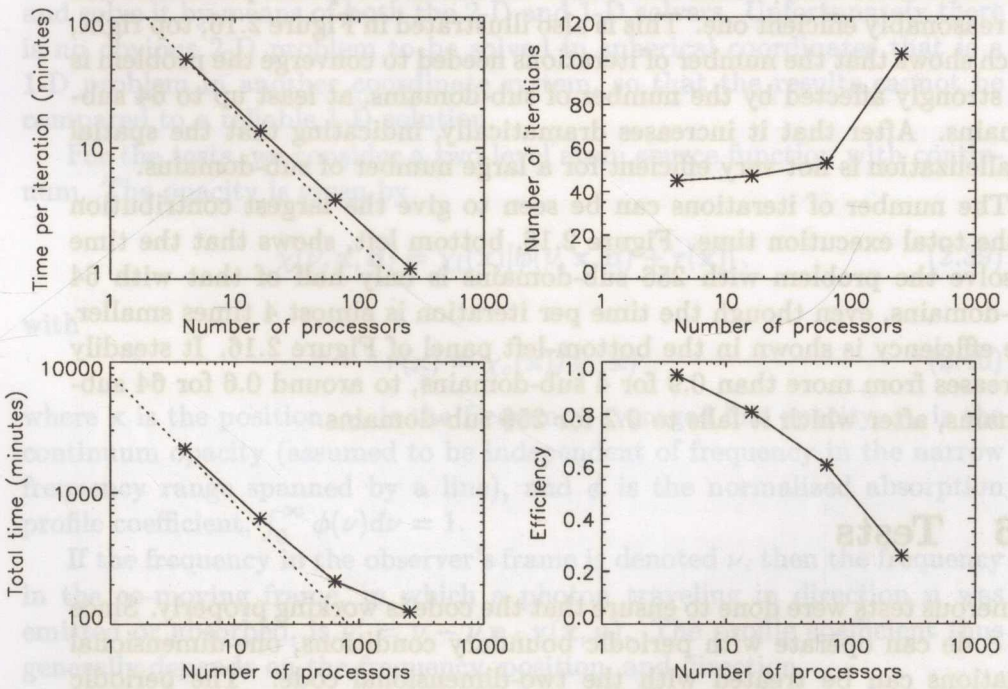


Figure 2.16: **Top left:** *Time per iteration as a function of the number of sub-domains (or processors).* **Top right:** *Number of iterations needed to converge the problem.* **Bottom left:** *Total time needed to solve the problem.* **Bottom right:** *Efficiency.*

the total convergence time, as the two quantities describe different limita-

tions of the method. Differences in the time per iteration are dominated by the communication of the sub-domains, whereas the total execution time is determined by both the communication, and a slower convergence of the iteration method. The former is constant for all problems and can be improved by increasing the communication speed, while the latter is inherent to the method and can only be improved by either choosing different sub-domains (i.e. different shape and/or location), or by reducing the number of sub-domains.

In Figure 2.16, top left, the time per iteration is plotted as a function of the number of processors. Since we use spatial parallelization, the number of processors is equal to the number of spatial sub-domains. The dotted line shows the theoretical limit of an efficiency of 1. The time per iteration as a function of the number of sub-domains does not deviate strongly from the $1/N$ theoretical limit, which shows that the scheme of spatial parallelization is a reasonably efficient one. This is also illustrated in Figure 2.16, top right, which shows that the number of iterations needed to converge the problem is not strongly affected by the number of sub-domains, at least up to 64 sub-domains. After that it increases dramatically, indicating that the spatial parallelization is not very efficient for a large number of sub-domains.

The number of iterations can be seen to give the largest contribution to the total execution time. Figure 2.16, bottom left, shows that the time to solve the problem with 256 sub-domains is only half of that with 64 sub-domains, even though the time per iteration is almost 4 times smaller. The efficiency is shown in the bottom-left panel of Figure 2.16. It steadily decreases from more than 0.9 for 4 sub-domains, to around 0.6 for 64 sub-domains, after which it falls to 0.2 for 256 sub-domains.

## 2.6 Tests

Numerous tests were done to ensure that the code is working properly. Since the code can operate with periodic boundary conditions, one-dimensional situations can be treated with the two-dimensional code. The periodic boundary conditions were implemented by iteratively updating the boundary conditions on the periodic boundaries with the intensity values calculated in the previous iteration. Although this can converge very slowly in optically thin situations, convergence is greatly helped by applying Ng acceleration to the boundaries. A very convenient property of changing coordinate systems is that certain problems that are one-dimensional in one coordinate system become two-dimensional in another. This enables us to

efficiently test the implementation of the code in all geometries.

To test the Cartesian code, simulating a 1-D plane-parallel situation can be conveniently done by applying periodic boundary conditions to a 2-D slab with zero gradients in the periodic direction. The results can then easily be compared with the results from an existing, well-tested 1-D code. Furthermore, the case of an infinite cylinder, a true 2-D problem in Cartesian coordinates, can be compared to the solution obtained with a cylindrical 1-D solver.

The cylindrical code can then be tested by calculating the source function in an infinite cylinder, using both a 2-D solver (again, with periodic boundary conditions in the $z$-direction), and with a 1-D cylindrical solver. Similarly, a solution of a sphere, a true 2-D problem in cylindrical coordinates, can be compared to that of a spherical 1-D solver.

The spherical code can be tested by using a sphere as the test structure, and solve it by means of both the 2-D and 1-D solvers. Unfortunately there is no obvious 2-D problem to be solved in spherical coordinates that is a 1-D problem in another coordinate system, so that the results cannot be compared to a reliable 1-D solution.

For the tests, we consider a two-level atom source function with continuum. The opacity is given by

$$\chi(\nu, \mathbf{x}, \mathbf{n}) = \chi_l(\mathbf{x})[\phi(\nu, \mathbf{x}, \mathbf{n}) + r(\mathbf{x})], \tag{2.39}$$

with

$$r(\mathbf{x}) = \chi_c(\mathbf{x})/\chi_l(\mathbf{x}) \tag{2.40}$$

where $\mathbf{x}$ is the position, $\chi_l$ is the frequency-averaged line opacity, $\chi_c$ is the continuum opacity (assumed to be independent of frequency in the narrow frequency range spanned by a line), and $\phi$ is the normalized absorption profile coefficient, $\int_0^\infty \phi(\nu) d\nu = 1$.

If the frequency in the observer's frame is denoted $\nu$, then the frequency in the co-moving frame, in which a photon traveling in direction $\mathbf{n}$ was emitted or absorbed, is $\nu' = \nu - \nu\,\mathbf{n} \cdot \mathbf{v}(\mathbf{x}, \mathbf{n})$. The profile coefficient thus generally depends on the frequency, position, and direction.

For all the following tests, we assume a depth-independent Doppler profile,

$$\phi(\nu') = \frac{1}{\sqrt{\pi}\,\Delta\nu_D} \exp\left[-\left(\frac{\nu' - \nu_0}{\Delta\nu_D}\right)^2\right], \tag{2.41}$$

where $\Delta\nu_D = \nu_0 v_{\text{th}}/c$ is the Doppler width, with $v_{\text{th}}$ being the thermal velocity, and $\nu_0$ the frequency of the line center. As usual, we will use a

dimensionless frequency

$$x = (\nu' - \nu_0)/\Delta\nu_D\,, \tag{2.42}$$

so the profile coefficient becomes

$$\phi(x) = \exp(-x^2)/\sqrt{\pi}\,. \tag{2.43}$$

Analogously, the velocity is expressed in units of the thermal velocity.

The total source function is given by

$$S = \frac{\phi}{\phi + r} S_l + \frac{r}{\phi + r} S_c = \frac{\phi}{\phi + r} [(1 - \epsilon)\bar{J} + \epsilon B] + \frac{r}{\phi + r} S_c\,, \tag{2.44}$$

where $S_l$ and $S_c$ are the line and the continuum source function, respectively (we drop here an explicit indication of a dependence of quantities on frequency, position, and angle).

Although our formalism allows for a general positional dependence of $\epsilon(\mathbf{x})$, $B(\mathbf{x})$, and $\mathbf{v}(\mathbf{x}, \mathbf{n})$, we take here for simplicity constant $\epsilon$, chosen as a free parameter of the problem, and constant $B$, set up for convenience to $B = 1$. We also set the continuum source function $S_c = B = 1$ and when we refer to an optical depth, we always mean the one corresponding to the frequency-averaged line opacity,

$$d\tau = \chi_l\, ds\,, \tag{2.45}$$

where $ds$ it the element of path length in a given direction.

When an angular resolution is quoted, this is always done in the form $N_\phi \times N_\theta$, where $N_\phi$ is the total number of angles in the $\phi$ direction but $N_\theta$ is the number of angles in one quadrant of $\theta$ only, since the second quadrant of $\theta$ does not need to be considered if the velocity vector has a zero tangential component (e.g., in the case of no rotation). Also when angles are said to be distributed homogeneously, this means that the values of $\phi$ and $\theta$ are each distributed homogeneously, and thus the angular points projected onto a sphere are not.

Finally, all test problems are converged until the maximum relative change in the line source function per iteration anywhere on the grid is less than $10^{-3}$.

### 2.6.1 Tests of the Cartesian Solver

We have performed the following six individual tests: (*i*) box test, i.e., a numerical evaluation of the emergent radiation from a homogeneous Cartesian

box, compared to the analytical solution; (*ii*) a horizontally-homogeneous plane-parallel slab infinite in the $x$-direction (recall that in our 2-D solver the $y$-direction is always infinite), solved by the 2-D solver (with periodic boundary conditions in the $x$-direction), and by a 1-D plane-parallel solver; (*iii*) a static cylinder, infinite in $y$-direction, solved by the 2-D Cartesian solver and by a 1-D cylindrical solver; (*iv*) the same, but for radially expanding cylinder; (*v*) the same, but for a cylinder with a differential rotation about the axis of symmetry; (*vi*) finally, a comparison with two test cases from the Mihalas, Auer, & Mihalas (1978) study.

#### 2.6.1.1 Box test

The simplest test of the Cartesian solver is a homogeneous-box test: we assume opacity and the source function constant within the computational box (set for convenience to unity, $\chi = S = 1$), so that one can easily obtain

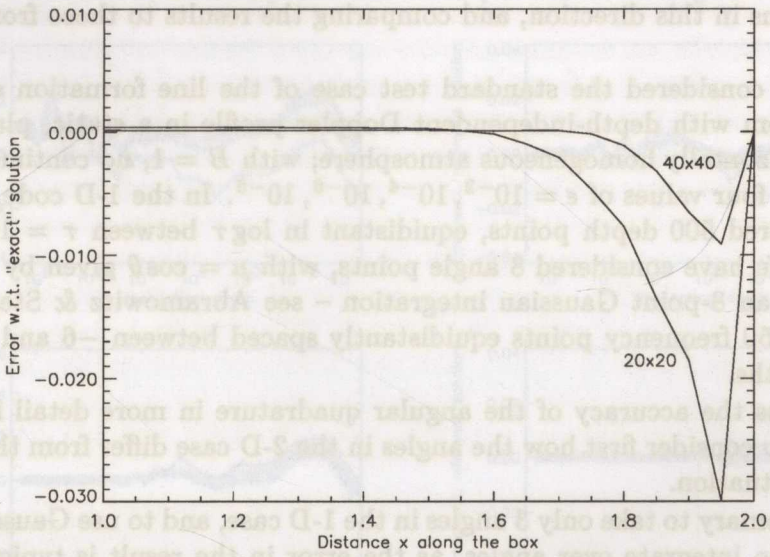


Figure 2.17: *Relative error of the emergent intensity from a homogeneous Cartesian box as a function of $x$. The lower and upper curves are for the* $20 \times 20$ *and* $40 \times 40$ *spatial grid points.*

an analytical solution for the emergent mean intensity. Comparing the analytical results with the numerical results using our 2-D Cartesian solver, we can assess the magnitude of spatial and angular interpolation errors.

The result for a box with the total optical thickness in the $x$- and $z$-direction set to $\tau_x = \tau_z = 2$, is displayed in Figure 2.17, where we plot

the error of the numerical solution as a function of $x$, for two spatial resolutions, $20 \times 20$ and $40 \times 40$ spatial grid points. In both cases, we have used $60 \times 16$ homogeneously distributed angles. The error in the emergent mean intensity obviously depends on the number of $x$ and $z$ grid points; for $20 \times 20$ points the error reaches 3%, while for $40 \times 40$ points the maximum error decreases to about 1%. The solution for $40 \times 40$ spatial points was also computed with $80 \times 21$ homogeneously distributed angles, giving an essentially identical result to the solution with $60 \times 16$ homogeneously distributed angles, indicating that the remaining error is primarily due to the spatial resolution.

#### 2.6.1.2 Comparison to a 1-D plane-parallel static solution

As mentioned above, one can test a 2-D solver by considering a problem which is homogeneous in one of the two directions by using periodic boundary conditions in this direction, and comparing the results to those from a 1-D solver.

We have considered the standard test case of the line formation of a two-level atom with depth-independent Doppler profile in a static, plane-parallel, horizontally homogeneous atmosphere; with $B = 1$, no continuum ($r = 0$), and four values of $\epsilon = 10^{-2}, 10^{-4}, 10^{-6}, 10^{-8}$. In the 1-D code, we have considered 500 depth points, equidistant in $\log\tau$ between $\tau = 10^{-5}$ and $10^{12}$. We have considered 8 angle points, with $\mu = \cos\theta$ given by the abscissae of an 8-point Gaussian integration – see Abramowitz & Stegun (1973), and 50 frequency points equidistantly spaced between $-6$ and $+6$ Doppler widths.

To discuss the accuracy of the angular quadrature in more detail it is instructive to consider first how the angles in the 2-D case differ from those in the 1-D situation.

It is customary to take only 3 angles in the 1-D case, and to use Gaussian quadrature to integrate over angles, as the error in the result is typically only about 1%. This is due to the fact that in static 1-D the points on the grid actually represent infinite planes with angular size $2\pi$. The angular variation of the intensity within this $2\pi$ is therefore due only to angular variation of the monochromatic optical depth $\tau_\nu/\mu$ and is thus predictable. It is therefore possible to choose quadrature points that *always* describe this variation accurately, such as Gaussian quadrature points.

In a true 2-D problem with rotational symmetry, like a cylinder or a sphere, the angular variation of the intensity can be due to variations of the angular size of the source object as a function of distance to the object as

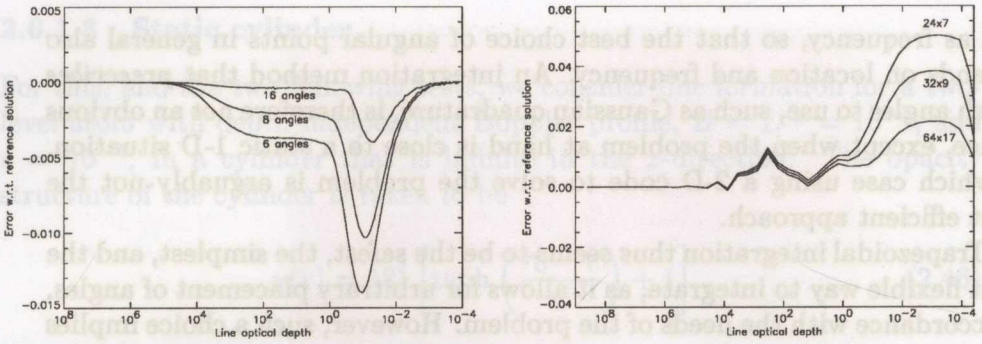


Figure 2.18: *Effects of angular resolution.* **Left panel:** *Relative error of the 1-D plane-parallel solution with trapezoidal integration in angles for various numbers of angles (6, 8, 12).* **Right panel:** *Relative error of the 2-D solution (with periodic boundary conditions in one direction) for several angular resolutions. In all cases, the reference ("exact") solution is a 1-D plane-parallel model with 8-point Gaussian quadrature in angles.*

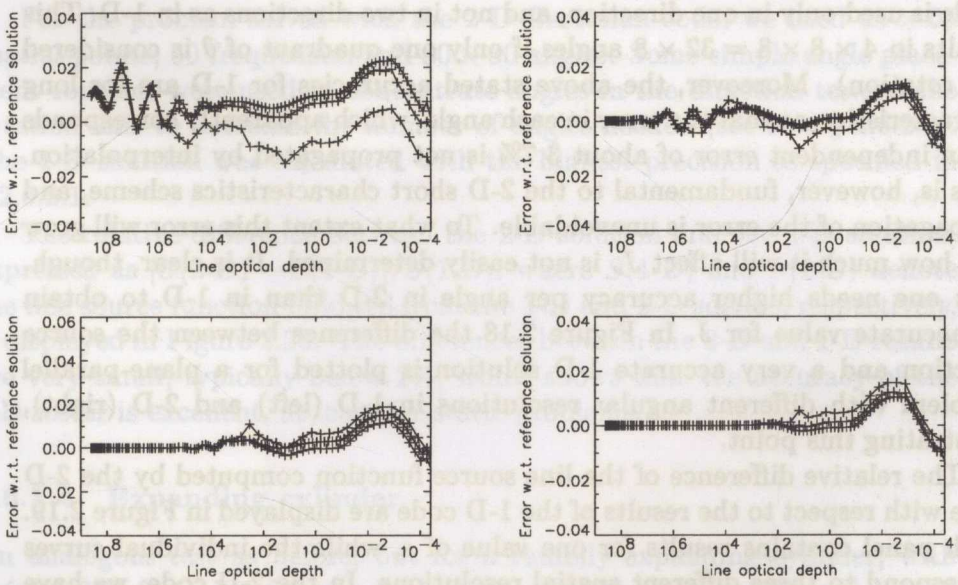


Figure 2.19: *Relative differences of the source function of a 1-D plane-parallel problem computed by the 2-D Cartesian solver (with periodic boundary conditions in one direction), and by the 1-D solver, are displayed as a function of the line optical depth in the z-direction for several spatial resolutions (with 65, 97, and 145 points in the z-direction, and 5 points in the x-direction). Clock-wise from the upper left panel:* $\epsilon = 10^{-8}$, $10^{-6}$, $10^{-2}$, $10^{-4}$.

well as frequency, so that the best choice of angular points in general also depends on location and frequency. An integration method that *prescribes* which angles to use, such as Gaussian quadrature, is therefore not an obvious choice, except when the problem at hand is close to a static 1-D situation, in which case using a 2-D code to solve the problem is arguably not the most efficient approach.

Trapezoidal integration thus seems to be the safest, the simplest, and the most flexible way to integrate, as it allows for arbitrary placement of angles, in accordance with the needs of the problem. However, such a choice implies that one inevitably needs more angular points to achieve an accuracy similar to that obtained with Gaussian quadrature. We have found that in the 1-D case, the accuracy of the solution with trapezoidal angular integration (for $\epsilon = 10^{-4}$) is typically 1.5% for 6 angle points, 0.8% for 8 points, and 0.4% for 16 points, as shown in Figure 2.18, left.

For a 2-D problem, this means that to achieve a similar accuracy, each quadrant in $\phi$ and $\theta$ needs the same number of angles as in 1-D, as each angle is used only in one direction, and not in two directions as in 1-D. This results in $4 \times 8 \times 8 = 32 \times 8$ angles if only one quadrant of $\theta$ is considered (no rotation). Moreover, the above stated accuracies for 1-D are for long characteristics, so that the error in each angle, which apparently corresponds to an independent error of about 3.7% is not propagated by interpolation. This is, however, fundamental to the 2-D short characteristics scheme, and propagation of the error is unavoidable. To what extent this error will grow and how much it will affect $J_\nu$ is not easily determined. It is clear, though, that one needs higher accuracy per angle in 2-D than in 1-D to obtain an accurate value for J. In Figure 2.18 the difference between the source function and a very accurate 1-D solution is plotted for a plane-parallel problem with different angular resolutions in 1-D (left) and 2-D (right), illustrating this point.

The relative difference of the line source function computed by the 2-D code with respect to the results of the 1-D code are displayed in Figure 2.19. Each panel contains results for one value of $\epsilon$, while the individual curves correspond to three different spatial resolutions. In the 2-D code, we have considered 5 points in the $x$-direction, and 65, 97, and 145 points points in the $z$ direction, 72 angles in the $xz$ plane, and 32 angles out of the $xz$ plane; for simplicity the angles were equidistantly spaced. The frequency points were the same as in the 1-D case.

#### 2.6.1.3 Static cylinder

For this, and the two following tests, we consider line formation for a two-level atom with depth-independent Doppler profile, $B = 1$, $r = 10^{-4}$, and $\epsilon = 10^{-4}$, in a cylinder that is infinite in the $z$-direction. The opacity structure of the cylinder is taken to be

$$\chi(r) = 10^4 \left[ \tanh\left( \frac{r_0 - r}{w} \right) + 1 \right], \tag{2.46}$$

where $r_0 = 0.2$ and $w = 0.06$, so that the total optical thickness of the structure is roughly $10^8$ in the line and $10^4$ in the continuum. The structure is calculated in the region $0 \leq x \leq 1$ and $0 \leq z \leq 1$ with the 2-D Cartesian solver and in the region $0 \leq r \leq 1.5$ with a 1-D cylindrical solver, which we have specifically written for this purpose. We will describe this code, and the sensitivity of the results on the number of radial and frequency points, in § 2.6.2.1.

For the problem solved with the 2-D Cartesian code, we used $65 \times 65$ spatial points, 50 frequencies and $80 \times 30$ angles. Some simple angle placement routines were used to concentrate angles in the direction toward the rotation axis to decrease the number of angles needed (see also § 2.6.2.2). The 1-D solution was calculated with the highest precision as specified in § 2.6.2.1.

The relative difference between the 2-D solution and the 1-D solution, expressed as $[S(\text{2-D}) - S(\text{1-D})]/S(\text{1-D})$, where $S(\text{1-D})$ and $S(\text{2-D})$ denote the line source function followed from the 1-D and 2-D solvers, respectively, is displayed in Figure 2.20. The differences between the 2-D and 1-D results are very small, typically below 2%, which shows that the accuracy of the 2-D solver is excellent, at least for static problems.

#### 2.6.1.4 Expanding cylinder

An analogous test as before, but for a radially expanding cylinder, with $v_r(r) = 10\,r$ (in units of thermal velocity), and with $v_z = v_\phi = 0$, is displayed in Figure 2.21. This problem was solved with $65 \times 65$ spatial points, 80 frequencies distributed between -5 and +20 Doppler widths, and $80 \times 30$ angles. The difference between the 1-D and the 2-D solutions is substantially larger than in the static case, which can be attributed both to the 1-D and the 2-D solution (see also § 2.6.2.1). Nevertheless, the solutions still agree to within 4%, which is quite reasonable given the limited resolution, especially in frequency.

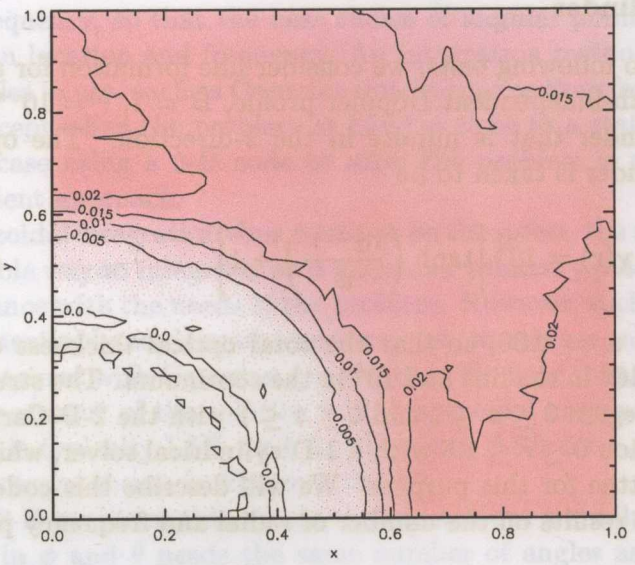


Figure 2.20: *Relative difference of the source function for a static cylinder, infinite in the z-direction, computed by the 2-D and 1-D solvers.*

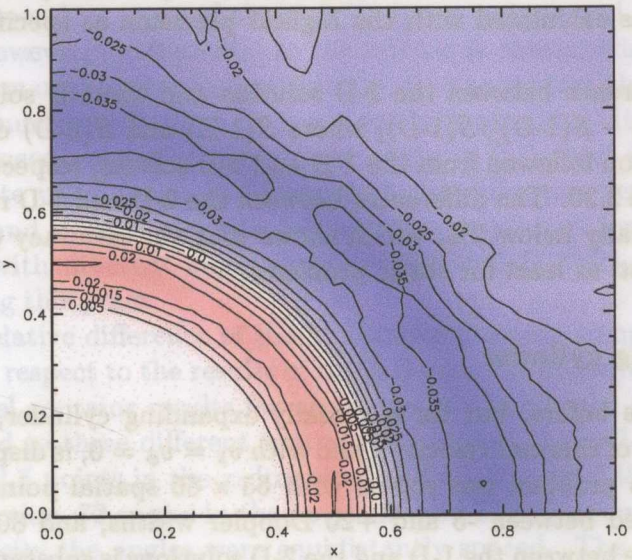


Figure 2.21: *Relative difference of the source function for a radially expanding cylinder, infinite in the z-direction, computed by the 2-D and 1-D solvers.*

#### 2.6.1.5 Rotating cylinder

An analogous test, but for a cylinder rotating about the axis of symmetry is displayed in Figure 2.22. The rotational velocity is a smoothly varying combination of rigid and Keplerian rotation,

$$v_\phi(r) = \frac{\Omega r}{2}\left[\tanh\left(\frac{r_0 - r}{v}\right) + 1\right] + \frac{\Omega r_0}{2r}\left[1 - \tanh\left(\frac{r_0 - r}{v}\right)\right], \quad (2.47)$$

where $\Omega = 10$, $r_0 = 0.2$, and $v = 10^{-1}$.

The problem was solved with 127 × 127 spatial points, 70 frequencies distributed between -9 and +9 Doppler widths, and 70 × 20 angles. The difference compared with a 1-D cylindrical solution is not much larger that that for the static cylinder test (see § 2.6.1.3), indicating that velocities are treated accurately when they are relatively small compared to the thermal velocity.

#### 2.6.1.6 Comparison to the Mihalas-Auer-Mihalas results

Finally, we have computed several representative models with the same parameters as analogous models computed by MAM. We show the results of two of these models in Figure 2.23. The first is the MAM test case I, with $\epsilon = 10^{-3}$, $r = r_0/[1 - 0.5\cos(2\pi x/X)]$ with $r_0 = 1$; $X$ being the total extent of the slab in the $x$-direction. The MAM solution is displayed in their Figure 3a; notice that there is likely a numerical typo in their caption: their $\beta_0$, which is our $1/r_0$, is stated to be $10^2$, whereas our models agree with theirs only for $\beta_0 = 1$. The second model is the MAM test case IIIc (their Figure 5c) with $\epsilon = 10^{-3}$, $r = 10^{-4}$, and a velocity of the form $v_z(x,z) = v_{z0}\exp(0.001z)\cos(2\pi x/X)$, with $v_{z0} = 2$.

The adopted spatial resolution for case 1 could not be found in MAM, so we took it to be 20 × 20. We used 50 frequencies and 24 × 6 angles, which is more than MAM did (they used Carlsson angular quadrature set B with only 6 points per quadrant), but homogeneously (and thus less favorably) distributed in both angles and with trapezoidal (and thus less accurate) integration weights. The spatial resolution for case 3c is taken to be 19 × 28, identical to that of MAM; the frequency and angular resolution were again taken to be 50 and 24 × 6, respectively. A visual inspection of their figures and ours indicates that the agreement is quite reasonable. Our curves are somewhat smoother which may be the result of the larger number of angles and/or frequencies.

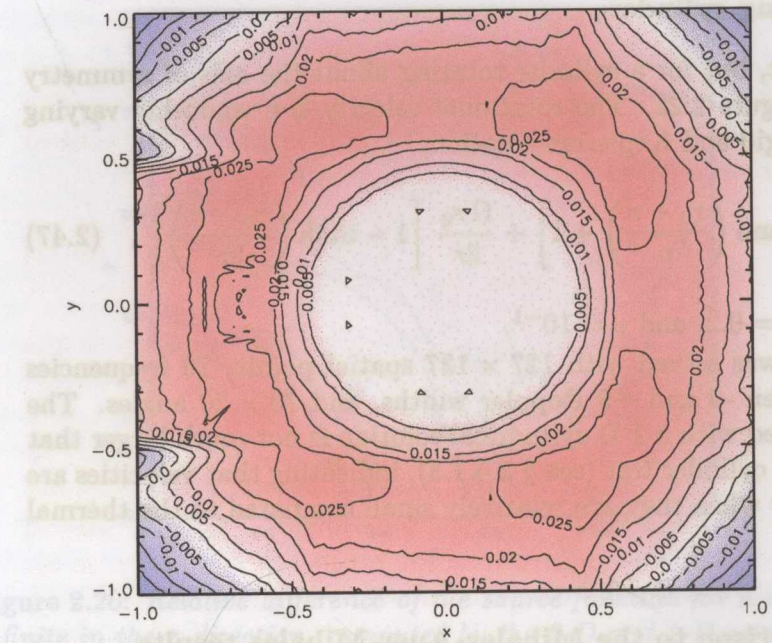


Figure 2.22: *Relative difference of the source function for a rotating cylinder, infinite in the z-direction, computed by the 2-D and 1-D solvers.*

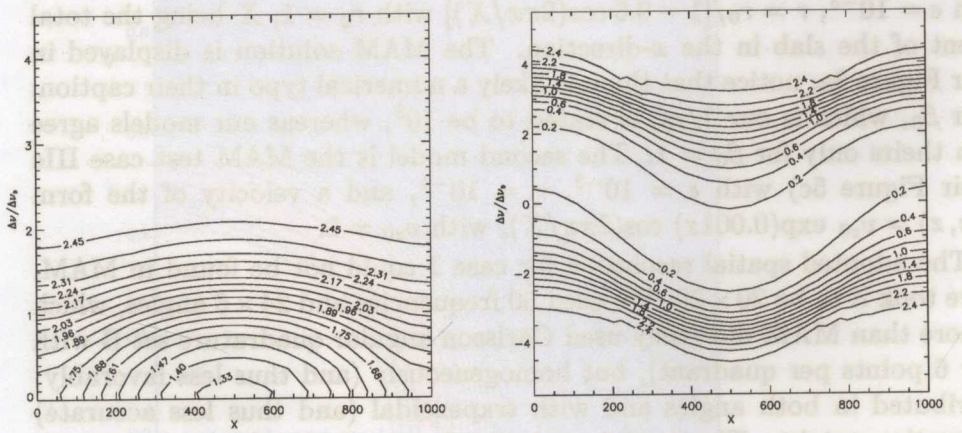


Figure 2.23: *Two representative models computed for the same parameters as in Mihalas, Auer, & Mihalas (1978) as specified in the text. The left panel is to be compared to their Figure 3a; the right panel to their Figure 5c.*

### 2.6.2 Tests of 2-D Cylindrical Solver

We have performed the following five tests: (*i*) line transfer in a static cylinder, infinite in the $z$-direction, computed with the 2-D solver (with a periodic boundary condition in the $z$-direction), and with a 1-D cylindrical solver; (*ii*) the same, but for radially expanding cylinder; (*iii*) the same, but for a cylinder with a differential rotation about the axis of symmetry; (*iv*) line transfer in a static sphere, computed by the 2-D cylindrical solver, and by a 1-D spherical solver; (*v*) the same as before, but for a radially expanding sphere.

#### 2.6.2.1 1-D cylindrical solver

In order to be able to perform the above outlined tests, we first had to develop a 1-D cylindrical solver. We have used the ALI method, analogously as for 1-D plane-parallel solver. The individual formal solutions of the transfer equation were accomplished by the tangent-ray method. To include velocities easily, we use the short characteristic method. The program considers an arbitrary number of radial points, frequencies, and out-of-plane (that is, out of the plane perpendicular to the $z$-axis) angles, which are the only three free parameters of the specification of the computational grid.

As the aim of the 1-D code, in the present context, was to provide an essentially "exact" solution, we have extensively studied the accuracy of the solution, and its dependence on the number of radial points, out-of-plane angles, and frequency points. Recall that in the tangent ray method, the in-plane angles are determined by the choice of radial points, so that they cannot be chosen independently. For the present tests, the radial points were set up equidistantly between $r = 0$ and 1.5. The frequency points were placed equidistantly between the corresponding frequency limits, which were chosen to be -6 to 6 Doppler widths for the static cylinder, -26 to +6 Doppler widths for the expanding cylinder, and -12 to +12 Doppler widths for the rotating cylinder.

Some representative results are displayed in Figure 2.24, which shows that the maximum error of the source function for the static cylinder is quite small for a reasonable number of points, but decreases rather slowly with increasing number of radial points (and thus the number of angles) for an expanding cylinder. This can be attributed both to the unsatisfactory selection of angles that is provided by the tangent-ray method, and consequently large projected velocity differences for the individual rays. Interestingly, even a model with 500 radial points differs from the reference solution of 1000 radial points by several tenths of a percent, indicating that

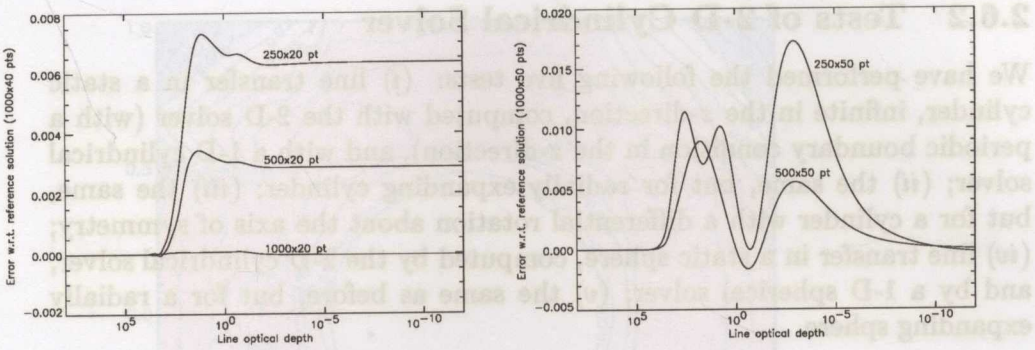


Figure 2.24: *Relative differences of the solution of a static cylinder (left), and an expanding cylinder (right) solved in 1-D cylindrical coordinates with different spatial resolutions.*

the reference solution may still contain a significant error (see also §2.6.3.1). The main source of this error can be attributed to the actual tangent angles in each point. This is because the angular bin for these angles is largest – see Figure 2.3, right – and the projected relative velocity difference between the tangent point and the next point on the tangent ray is also largest.

### 2.6.2.2 Static cylinder

The models adopted here have the same radial opacity structure as the cylinder taken in the tests of the 2-D Cartesian code (§ 2.6.1.3 - 2.6.1.5), and are taken to be infinitely stretched in the $z$-direction by applying periodic boundary conditions. All computed models are calculated with 97 radial points and 5 points in the $z$-direction.

First, we investigate a dependence of the accuracy of the solution on different angular resolutions in the out-of-plane angle for a given angular positioning. The difference between the 1-D cylindrical solution of a static cylinder and the 2-D solutions is displayed in Figure 2.25 left, for models with 60 in-plane angles, and 10, 20, 30 and 40 out-of-plane angles. The results are not very sensitive to the number of angles; even for only $60 \times 10$ angles, the accuracy is still better than about 1%.

The accuracy of the solution for a fixed number of $60 \times 20$ in-plane angles. but positioned differently, was tested for several different angular distributions in the out-of plane angle $\theta$. These distributions were calculated

following an angle density distribution of the form:

$$\rho(\theta, r) = \exp\left[-\left(\frac{\theta - \theta_0}{\sigma(r)}\right)^2\right], \tag{2.48}$$

where $\theta$ is the current angle, $\theta_0$ is the angle corresponding to the direction to the axis of symmetry, and $\sigma$ is the estimated angular size of the "source region". The latter is understood here as the region that provides most of the incoming radiation as seen from the current position $r$.

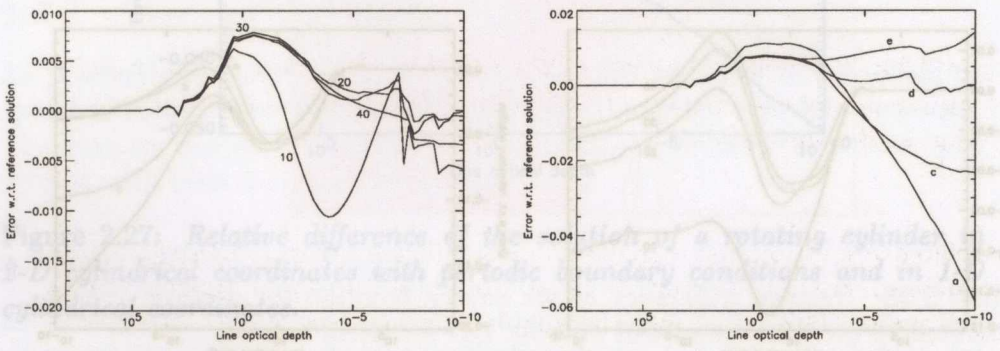


Figure 2.25: *Relative difference of the solution of a static cylinder solved in 2-D cylindrical coordinates with periodic boundary conditions, and in 1-D cylindrical coordinates as a function of the angular resolution (left) and the angular positioning (right). The annotation refers to the number and positioning of angles defined in § 2.6.2.2. Model b would lie very close to model a, and is thus not displayed.*

Five different distributions were calculated this way, distribution $a$, with $\sigma(r) = \infty$ (homogeneous distribution), and distributions $b$-$e$ with

$$\sigma = \begin{cases} f\pi r_0/(r - r_0)\,, & \text{for } r > r_0\,, \\ \infty\,, & \text{for } r \leq r_0\,, \end{cases} \tag{2.49}$$

where $r_0$, the distance where the radiation field is expected to become anisotropic, was taken to be 0.6, and $f = 10, 1, 0.5$ and $0.25$ for distributions $b$-$e$, respectively.

The sensitivity to the positioning of the angles gives a very different picture from varying the angular resolution, as can be seen in Figure 2.25, right. The accuracy of the solution deteriorates rapidly with distance to the cylinder if the angles are not aimed at the source object. Concentrating the angles toward the source region proves to be a very efficient method of increasing the accuracy of the solution at no additional computational cost.

### 2.6.2.3 Expanding cylinder

Analogous tests were done for a radially expanding cylinder, with a velocity and opacity structure as in Cartesian test case (*iv*) (§2.6.1.4). The accuracy of the solution of an expanding cylinder by the 2-D cylindrical solver is much more sensitive to the number of angles than in the case of a static cylinder. The accuracy of the case with the fewest angles now has an error of about 12%, where the static model gave an error of only 1%. Even with the largest number of angles ($60 \times 40$), the error remains around 5%, as can

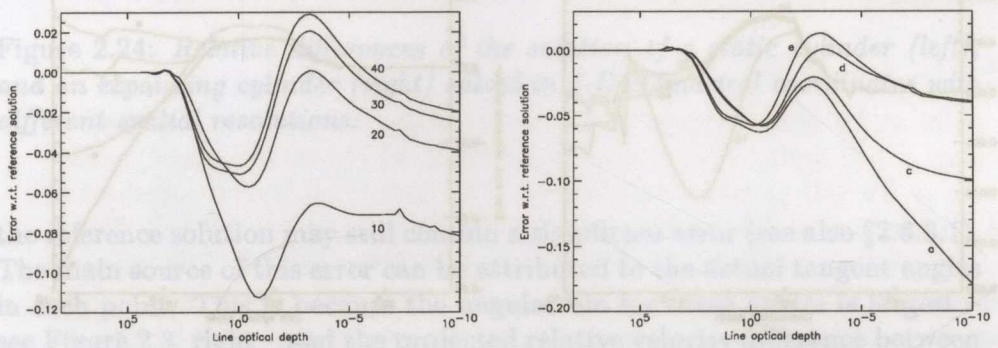


Figure 2.26: *Relative difference of the solution of a radially expanding cylinder in 2-D cylindrical coordinates with periodic boundary conditions and in 1-D cylindrical coordinates as a function of the angular resolution (left) and the angular positioning (right). The annotation refers to the number and positioning of angles defined in § 2.6.2.3. Model b would lie very close to model a, and is thus not displayed.*

bee seen in Figure 2.26, left panel.

For the test of accuracy of the angle positioning accuracy, the same positioning was taken as for the static cylinder tests. The right panel of Figure 2.26 shows that a selective placement of angles improves dramatically the accuracy of the solution at no additional computational cost, analogously to the case for the static cylinder.

### 2.6.2.4 Rotating cylinder

Due to the additional computational cost of including rotation, only one model was calculated with the best estimated angle positioning, distribution *d* above, and with $60 \times 20$ angles. Since the velocity has now a non-zero tangential component, both quadrants of $\theta$ need to be considered, so the intensity is actually evaluated at $60 \times 39$ angles. The difference between the

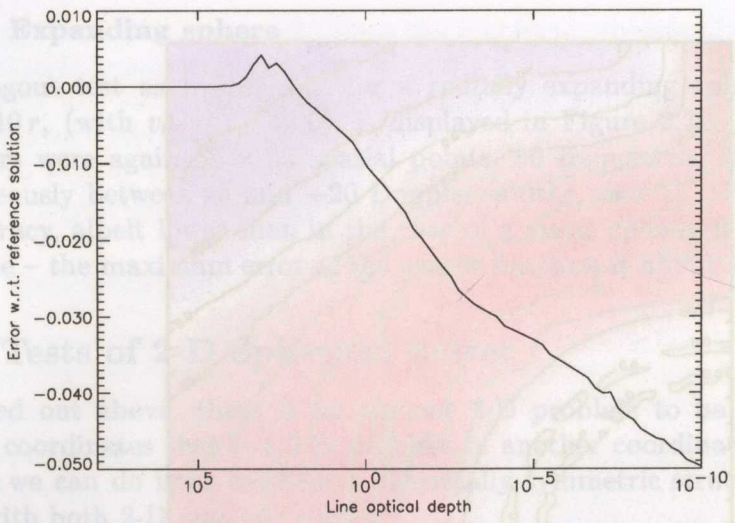


Figure 2.27: *Relative difference of the solution of a rotating cylinder in 2-D cylindrical coordinates with periodic boundary conditions and in 1-D cylindrical coordinates.*

2-D and the 1-D solution is displayed in Figure 2.27. The accuracy of the 2-D solver is about 5%, which is comparable to the solution of an expanding cylinder with a similar angular resolution and positioning.

### 2.6.2.5 Static sphere

Here we present a comparison of the results of the line transfer in a static sphere, computed with the 2-D cylindrical solver, and with a 1-D spherical solver (see § 2.6.3.1 for more details). The opacity structure is given by equation (2.46), where $r$ now denotes the spherical radius rather than the cylindrical radial coordinate. The computational domain of the 2-D solution is taken to be $0 \leq r \leq 1$ and $0 \leq z \leq 1$, and that of the 1-D spherical solution $0 \leq r \leq 1.5$.

The test case was calculated with $65 \times 65$ spatial points, 50 frequencies distributed homogeneously between -6 and +6 Doppler widths, and $80 \times 30$ angles. The difference between the 2-D cylindrical and the 1-D spherical solutions is displayed in Figure 2.28. The differences are very small, which again demonstrates an excellent accuracy of our 2-D cylindrical code.

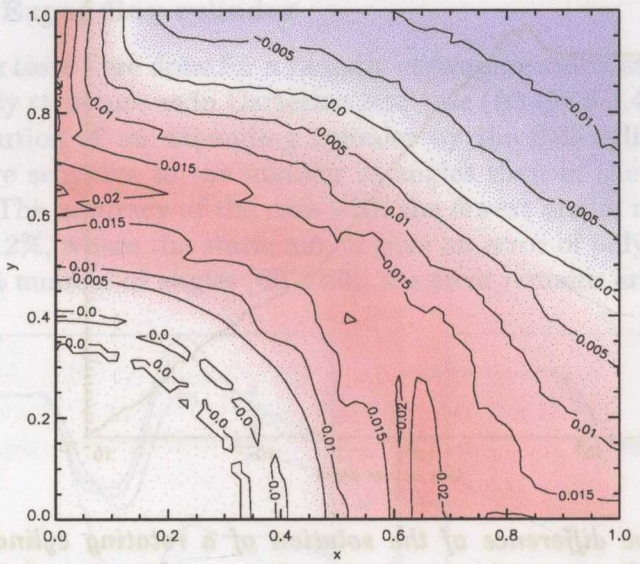


Figure 2.28: *Relative difference of the source function for a static sphere computed by the 2-D cylindrical and the 1-D spherical solvers.*

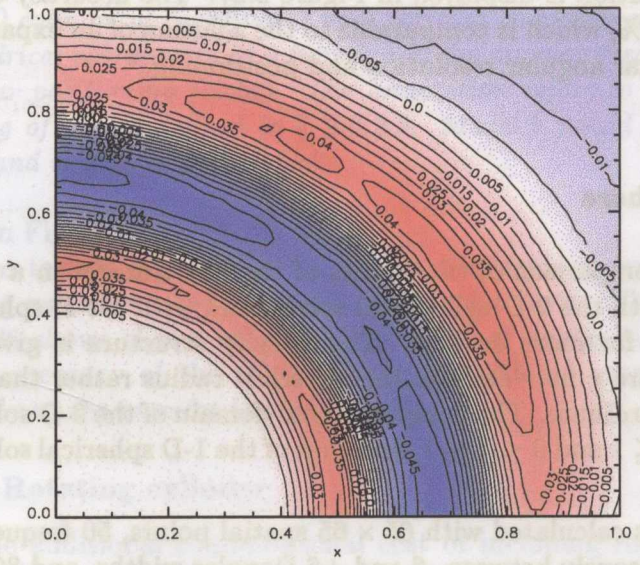


Figure 2.29: *Relative difference of the source function for an expanding sphere computed by the 2-D cylindrical and the 1-D spherical solvers.*

#### 2.6.2.6 Expanding sphere

An analogous test as before, but for a radially expanding sphere, with $v_r(r) = 10\,r$, (with $v_\theta = v_\phi = 0$), is displayed in Figure 2.29. The grid parameters were again 65 × 65 spatial points, 80 frequencies distributed homogeneously between -5 and +20 Doppler widths, and 72 × 32 angles. The accuracy, albeit lower than in the case of a static sphere, is still very reasonable – the maximum error of the source function is about 4%.

### 2.6.3 Tests of 2-D Spherical Solver

As pointed out above, there is no obvious 2-D problem to be solved in spherical coordinates that is a 1-D problem in another coordinate system. The best we can do is to consider a spherically-symmetric structure, and solve it with both 2-D and 1-D solvers.

#### 2.6.3.1 1-D spherical solver

As in the case of cylindrical coordinates, we have first developed a 1-D spherical code. This code is very similar to the 1-D cylindrical code described above; in fact the only difference is to drop any reference to the out-of-plane angles. Consequently, the spherical solver is much faster than the analogous 1-D cylindrical solver.

We have performed a number of tests in order to study the sensitivity of the results on the number of radial points. Some representative results are displayed in Figure 2.30, which is analogous to Figure 2.24. Again, as in the case of the 1-D cylindrical solver, the maximum error of the source function decreases only slowly with increasing number of radial points, especially if velocities are present.

The maximum number of radial points considered for an expanding sphere was 4000; however the difference from the solution with 2000 points was still around 1%. This means that it is likely that even more points are needed to achieve a converge to an almost "exact" solution, which may still differ from the 4000-point solution by as much as a few percent.

#### 2.6.3.2 Static sphere

In Figure 2.31, we present a comparison of the results of the line transfer in a static sphere, computed with the 2-D spherical solver, and with the 1-D spherical solver. The structure is again calculated from equation (2.46), with $r$ being the spherical radius. The computational domain is taken to be

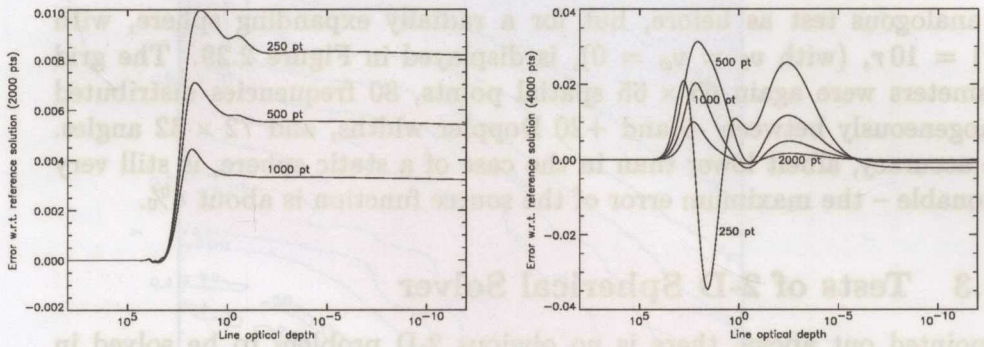


**Figure 2.30:** *Relative differences of the solution of a static sphere (left) and an expanding sphere (right) solved in 1-D spherical coordinates with different spatial resolutions.*

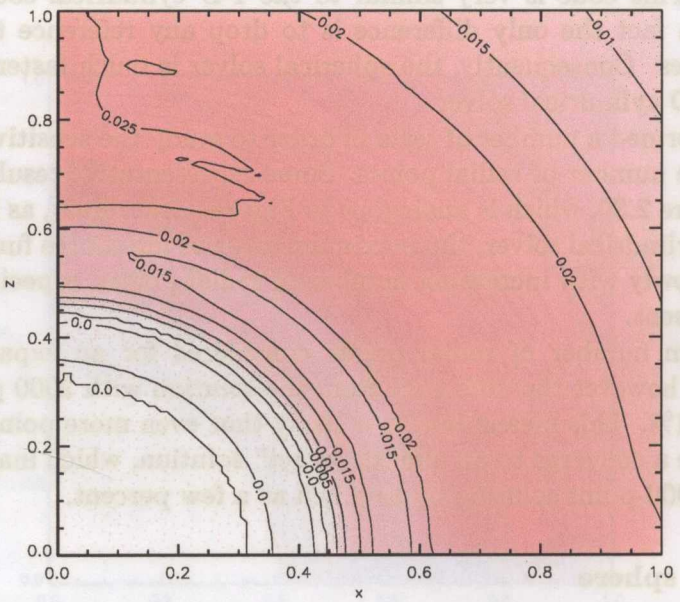


**Figure 2.31:** *Relative difference of the source function for a static sphere computed by the 2-D and the 1-D spherical solvers.*

$10^{-2} \leq r \leq 1.5$ and $0 \leq \Theta \leq \pi/2$. Since the problem is spherically symmetric, a substantially smaller number of $\Theta$-points than radial points is needed. The solution was calculated with 97 radial and 33 $\Theta$-points, 50 frequencies distributed homogeneously between from -6 and +6 Doppler widths, and 80 × 30 angles. The differences are very small, which demonstrates an excellent accuracy of our 2-D spherical code.

### 2.6.3.3 Expanding sphere

Finally, we consider an analogous test as before, but for a radially expanding sphere with $v_r(r) = 10\,r$ (in the units of thermal velocity) – see Figure 2.32. The grid parameters are 97 radial and 33 $\Theta$-points, 100 frequencies distributed homogeneously between -5 and +20 Doppler widths, and 72 × 32 angles. Again, the accuracy, albeit lower than in the case of static sphere, is still very reasonable - the maximum error of the source function is about 4%.

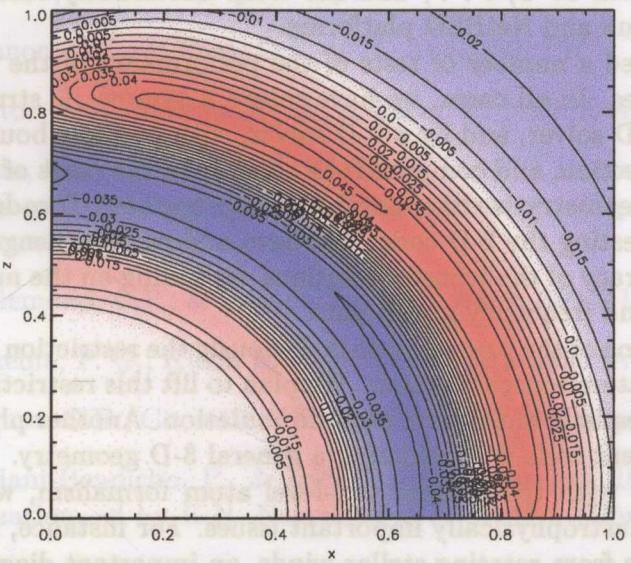


Figure 2.32: *Relative difference of the source function for an expanding sphere computed by the 2-D and the 1-D spherical solvers.*

## 2.7 Conclusion

We have developed an efficient and robust 2-dimensional radiative transfer solver appropriate for line transfer in the equivalent-two-level atom formal-

ism. The numerical method is based on application of the short characteristics scheme, together with the Accelerated Lambda Iteration technique. To increase the speed of convergence, we use standard Ng acceleration.

Our computer code presented in this paper incorporates all three standard geometries (Cartesian, cylindrical and spherical) in a transparent way, while allowing for arbitrary (3-dimensional) velocity fields. The geometry-specific parts of the radiative transfer solver are modularized, so that the change of geometry can be accomplished by simply setting the appropriate switch. We have also developed a parallel version of the code. We have shown that the only practical way is a parallelization in spatial sub-domains, and showed that such a scheme is surprisingly robust and efficient.

The code is written in C/C++, and has been successfully tested on Alpha, SUN, PC-Linux and NetBSD platforms.

We have performed a number of tests of the performance of the solver in all three geometries. In all cases, we have solved a symmetric structure by an appropriate 1-D solver, and by a 2-D solver, with periodic boundary conditions in one direction, and compared the results. In the cases of cylindrical and spherical geometry, we have developed appropriate 1-D codes just for the purposes of testing the 2-D code. We have addressed at length the issue of internal accuracy of the transfer solutions depending on the number of spatial, angular, and frequency grid points.

The basic limitation of the present code is obviously the restriction to the equivalent two-level atom source function. We plan to lift this restriction by considering a more realistic multi-level atom formulation. Another planned extension of the present code is considering a general 3-D geometry.

However, already with the present two-level atom formalism, we can address a number of astrophysically important issues. For instance, in the predicted line profiles from rotating stellar winds, an important diagnostic issue is the differences between the predicted line profiles when calculated by a 2-D code, and by a 1-D code which computes line profiles from a non-rotating stellar wind, and convolved with a rotational broadening kernel (i.e., with no influence of rotation on the line source function, nor with the effects of differential rotation). Similarly, we will address the importance of 2-D effects in predicting line profiles from accretion disks.

# References

1. Auer, L.H. 1987, in Numerical Radiative Transfer, ed. by W. Kalkofen (Cambridge: Cambridge Univ. Press), 101

2. Auer, L.H. 1991, in Stellar Atmospheres: Beyond Classical Models, ed. by L. Crivellari, I. Hubeny, and D.G.Hummer, NATO ASI Series C 341 (Dordrecht: Kluwer), 9

3. Auer, L. H., Fabiani-Bendicho, P., & Trujillo-Bueno, J. 1994, A&A, 292, 599

4. Auer, L. H., & Paletou, F. 1994, A&A, 285, 675

5. Balbus, S.A., & Hawley, J.F. 1991, ApJ, 376, 214

6. Busche, J.R., & Hillier, D.J. 2000, ApJ, 531, 1071

7. Cannon, C.J. 1970, ApJ, 161, 255

8. Cannon, C.J., & Rees, D.E. 1971, ApJ, 169, 157

9. Castor, J. I., Dykema, P. G., & Klein, R. I. 1992, ApJ,, 387, 561

10. Cram, L.E., Durrant, C.J., & Kneer, F. 1977, Report from the Workshop on Pluridimensional Radiative Transfer (Naples: Osservatorio Astronomico di Capodimonte)

11. Dullemond, C.P., & Turolla, R. 2000, A&A, 360, 1187

12. Dykema, P. G., Klein, R. I., & Castor, J. I. 1996, ApJ,, 457, 892

13. Eggum, G.E., Coroniti, V.F., & Katz, J.I. 1987, ApJ,, 323, 634

14. Fabiani-Bendicho, P., & and Trujillo-Bueno , J. 1999, in Solar Polarization, ed by K.N. Nagendra & J. Stenflo, (Dordrecht: Kluwer), 219

15. Fabiani-Bendicho, P., Trujillo-Bueno, J., & Auer, L.H. 1997, A&A, 324, 161

16. Feautrier, P. 1964, Compt. Rend. Acad. Sci. Paris, 258, 3189

17. Hubeny, I. 1992, in The Atmospheres of Early-Type Stars, ed. by U. Heber & C.J. Jeffery, Lecture Notes in Phys. 401, (Berlin: Springer), 377

18. Hummer, D. & Rybicky, G.; 1971, M.N.R.A.S., **152**, 1

19. Klein, R.I., Castor, J. I., Greenbaum, A., Taylor, D., & Dykema, P. 1989, J.Q.S.R.T., 41, 199

20. Kley, W. 1989, A&A, 208, 98

21. Kneer, F. 1981, A&A, 93, 387

22. Koesterke, L., Hamann, W.R., & Graefener, G. 2001, A&A, **384**, 562

23. Kunasz, P.B., & Auer, L.H. 1988, J.Q.S.R.T., 39, 67

24. Kunasz, P.B., & Olson, G.L. 1988, J.Q.S.R.T., 39, 1

25. Mihalas, D. 1978, Stellar Atmospheres, San Francisco: Freeman

26. Mihalas, D., & Mihalas, B.W. 1984, Foundations of Radiation Hydrodynamics, (New York: Oxford Univ. Press)

27. Mihalas, D., Auer, L.H., & Mihalas, B.W. 1978, ApJ, 220, 1001

28. Nordlund, Å., & Stein, R.F. 1991, in Stellar Atmospheres: Beyond Classical Models, ed. by L. Crivellari, I. Hubeny, and D.G.Hummer, NATO ASI Series C 341 (Dordrecht: Kluwer), 263

29. Olson, G.L., Auer, L.H., & Buchler, J.R. 1986, J.Q.S.R.T., 35, 431 (OAB)

30. Olson, G.L., & Kunasz, P.B. 1987, J.Q.S.R.T., 38, 325

31. Rosseland, S.; 1926, ApJ., **64**, 218

32. Rybicki, G.B. 1971, J.Q.S.R.T., 11, 489

33. Rybicki, G.B., & Hummer, D.G. 1991, A&A, 245, 171

34. Rybicki, G.B., & Hummer, D.G. 1992, A&A, 262, 209

35. Steiner, O. 1991, A&A, 242, 290

36. Stone, J.M., Mihalas, D., & Norman, M.L. 1992, ApJS, 80, 819

37. Stone, J.M., & Norman, M.L. 1992a, ApJS, 80, 753

38. Stone, J.M., & Norman, M.L. 1992b, ApJS, 80, 791

39. Strömgren B. 1935, Zs.f.Ap., **10**, 237

40. Trujillo-Bueno, J., & Fabiani-Bendicho, P. 1995, ApJ, 455, 646

41. Trujillo-Bueno, J., & Kneer, F. 1990, A&A, 232, 135

42. Wooley, R.v.d.R.; 1934, M.N.R.A.S., **94**, 631

# Chapter 3

# Line profile synthesis with Long Characteristics and Adaptive Mesh Refinement

**A code is presented that can generate a line profile or a monochromatic image of a multidimensional object with rotational symmetry, given the source function and opacity. It uses the Long Characteristics method to accurately solve the emergent intensity on a "screen" at a specified distance. Features in the image are automatically resolved by employing an adaptive mesh refinement technique. The agreement between the line profile calculated for a one-dimensional source function and atmospheric structure and that calculated with a 1-D long characteristics code is $\sim 1\%$.**

## 3.1 Introduction

In the previous chapter, a code was presented that can calculate the source function, given an underlying density, temperature and velocity structure, in 2-dimensions assuming rotational symmetry, using the short characteristics scheme and the Accelerated Lambda Iteration (ALI) technique (van Noort, Hubeny & Lanz, 2002).

Although this code effectively solves the 2-level atom radiative transfer problem under the stated conditions, one needs to process this information further to arrive at observable quantities.

The most significant observable in most astrophysical objects is the line profile of the spectral line for which the transfer problem has been solved. Although the code itself needs to compute the specific intensity $I_{\nu,\mu,\phi}$, the main interest ultimately is the angular averaged, line profile averaged intensity

$$\bar{J} = \int_0^\infty \int \varphi_\nu I_{\nu,\mu,\phi} \, \mathrm{d}\Omega \, \mathrm{d}\nu, \tag{3.1}$$

which does not require accurate representation of $I_{\nu,\mu,\phi}$ everywhere, but only where the contribution of $I_{\nu,\mu,\phi}$ to $\bar{J}$ is largest. Furthermore, the propagation of interpolation errors in the optically thin envelope of an object can result in considerable errors in $I_{\nu,\mu,\phi}$ and therefore in $\bar{J}$. Although this can result in a similar error in the line source function $S_l$, the effect on the line profile is usually small, as the envelope is optically thin and contributes little to the emergent intensity.

This means that a line profile calculated from $I_{\nu,\mu,\phi}$ at the surface directly from the code is not likely to be very accurate. In fact, to calculate the emergent line profile, it is better to calculate the emergent intensity at the surface by applying the long characteristics scheme for a single angle at a sufficient number of points at the surface.

## 3.2 Long characteristics

In the long characteristics scheme, the intensity at a point in a given direction is calculated by integrating the transfer equation along a photon path, a *characteristic* of the transfer equation, from the boundary of the computational grid to the point under consideration.

The long characteristics scheme does not suffer from the numerical diffusion that the short characteristics scheme does. It also has no need for the interpolation of the intensity for every grid cell the characteristic crosses,

so that accumulation of interpolation errors, which can easily grow to large values while propagating through the grid, can be avoided. There is obviously still the need to interpolate local quantities, such as the opacity, source function, velocity, etc., but the errors in these interpolates do not grow by propagation, but rather they average out.

Although these are all advantageous properties, the price to be paid for them is unattractive scaling with the number of grid points, which makes this method slow. The characteristic may intersect many grid lines and the value of the various quantities can vary by many orders of magnitude along the path. For an accurate value of the intensity to be calculated, these variations need to be properly sampled by a sufficient number of points, in each of which the value of several local quantities needs to be interpolated.

Moreover, it is easy to "miss" a compact source with a small angular size, so that adequate measures need to be taken to ensure that the intensity is accurately resolved.

Fortunately, in generating a line profile we only need to consider a single angle and much fewer spatial points than there are grid points, so that the extra cost may be reduced considerably. Nevertheless, this is a costly method and calculations of this type are orders of magnitude slower than equivalent 1-D methods.

## 3.3 Adaptive Mesh Refinement

In 1-D, the adaptive placement of points where they are needed most is an almost trivial affair. The points can be places at arbitrary positions, and the variation of the quantities that need to be described can be very large without generating any difficulties.

In multi-D, accurate representation of strongly varying quantities is not as easy, as placing many points on a localized object will unavoidably increase the resolution in other places where this is not needed. This is not only a waste of computer time, it may also lead to very inhomogeneous grid cells in some locations, which may cause numerical errors due to changes in numerical diffusion coefficients, etc.

Berger & Oliger (1984) developed a method, adaptive mesh refinement (AMR), that attempts to address this problem by assuming square cells everywhere. Instead of moving grid lines in one dimension to suit the quantities to be represented best, the grid lines remain fixed and the cells in which some quantity is not represented accurately enough is divided in a certain number of sub-cells, i.e. *refined*. If some quantity is then still not

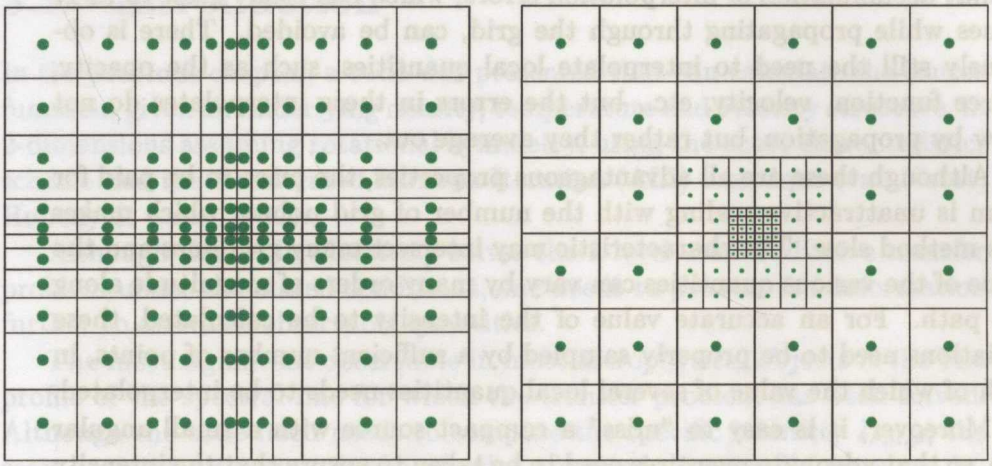

Figure 3.1: *Single grid (left) and AMR grid (right) methods of adaptive resolution management. The AMR method reaches twice the resolution of the single grid method with only half the total number of points.*

accurately represented, each of these new cells is refined again, etc., until all quantities are accurately represented everywhere.

It is obvious that fewer points are wasted where they are not needed, but the grid now has a new kind of inhomogeneity. The AMR grid has several refinement levels, in each of which there is an arbitrary number of grid points with an irregular spatial distribution. A given grid point may or may not have neighbours in the same refinement level, so that to maintain the hierarchy and to assess the accuracy of representation of a variable on the grid becomes more complicated.

To reduce the complexity of these tasks, an additional requirement is imposed on the grid structure, that the difference in refinement level between two adjacent grid cells can be no larger than 1, so that the resolution changes smoothly. In this way one can assume that even though a neighbour may not exist, it's parent does exist and can be used as a substitute.

The AMR method is particularly well suited to resolve structures that scale similarly in all dimensions. If the variation of a quantity in one dimension is very different from that in another, the method will automatically apply the same resolution to all dimensions, thereby overresolving the slowly varying direction and wasting points. To avoid this problem, however, the use of non-rectangular methods is needed, which introduces many complications and will not be dealt with here.

In astrophysics, the AMR method was pioneered by Klein, McKee & Colella (1994) for resolving interstellar shocks and graviationally collapsing clouds. A large amount of work has taken place in the past decade, mostly focusing on solving the MHD equations on an adaptively refined mesh, however, in the current context, the AMR technique will be regarded and applied as an established numerical concept, indepedent of this work.

## 3.4 The code

To generate a line profile, a series of monochromatic images is calculated and integrated across the image. The images are generated by projecting the emergent intensity onto a virtual "screen" with initially fixed size and square cells. Depending on the wavelength, the image then needs to be

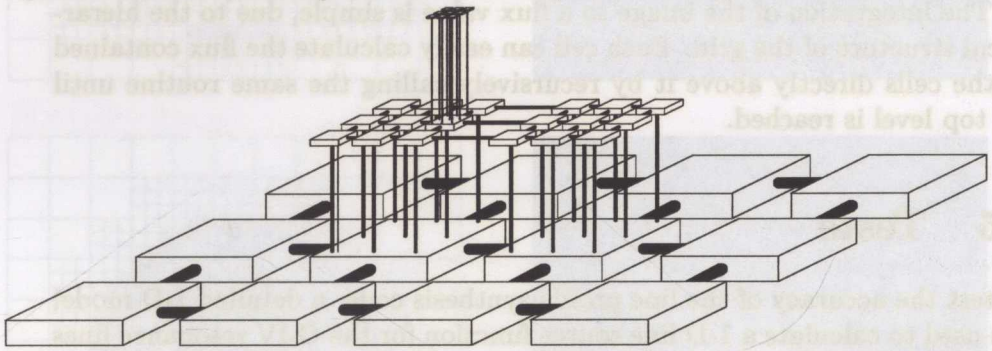

Figure 3.2: *Grid hierarchy in AMR: each block represents a grid cell. There are horizontal levels of cells of the same size, and a vertical tree structure of positional inheritance.*

resolved further in some of the cells. This was done by using the AMR technique.

The code was written in C++, so that full advantage could be taken of the ease with which hierarchical structures can be maintained with object oriented programming. Figure 3.2 illustrates the structure of the AMR part of the code, each of the blocks indicating an object representing a "pixel" in the image. Function calls on the objects are automatically passed on to the highest refinement level, so that the grid can be dealt with as if it is a simple matrix.

The dimensions and distance of the screen are first specified, then the intensity is calculated on the base grid. The accuracy is then assessed by interpolating the intensity in a cell from the intensity in the neighbouring

cells and requiring the relative difference between the interpolated value and the true value to be smaller than a specified accuracy goal. The cells that do not meet this requirement are found to be inaccurately represented and flagged for refinement.

In the next step all flagged cells are refined by a factor $3 \times 3$. The refinement factor was chosen to be odd, so that the central intensity does not need to be calculated again and no results need to be discarded.

This procedure is repeated a fixed number of times for a single image, or until no more cells need to be added. Since we integrate across the image, very sharp gradients do not need to be resolved completely, as the exact position of a feature is unlikely to change the integral by more than a small fraction, and an upper limit to the refinement level can safely be imposed to reduce the work load.

The integration of the image to a flux value is simple, due to the hierarchical structure of the grid. Each cell can easily calculate the flux contained by the cells directly above it by recursively calling the same routine until the top level is reached.

## 3.5 Tests

To test the accuracy of the line profile synthesis code, a detailed 1-D model was used to calculate a 1-D line source function for the C-IV resonance lines at 1551 and 1548Å. The line profile was then calculated with a 1-D line profile synthesis code and the multi-D long characteristics line profile synthesis code. For the multi-D code, the line and continuum source functions and the model atmosphere structure were first converted to spherically symmetric 2-D versions, to ensure that identical values for all variables were used.

The maximum level of refinement was chosen by calculating line profiles with increasing maximum refinement level, until relative change in the flux levels is less than 0.01 from one level to the next. The model was taken to be an $8.2\,M_\odot$ star with radius $8.4\,R_\odot$, $\dot{m}= 3 \cdot 10^{-7}\,M_\odot\,y^{-1}$, $T_{\rm eff}$=30000K and $V_\infty = 1960\,km\,s^{-1}$.

Grey scale images of the logarithm of the monochromatic intensity are shown in Figure 3.3, together with the grid used in the calculations. It can be clearly seen that the mesh appropriate for the continuum image is quite different from that appropriate for the image around flux maximum.

The relative difference between the line profile calculated with a 1-D code and that calculated with the multi-D code is plotted in Figure 3.4. The difference is very small and changes very little for increased maximum

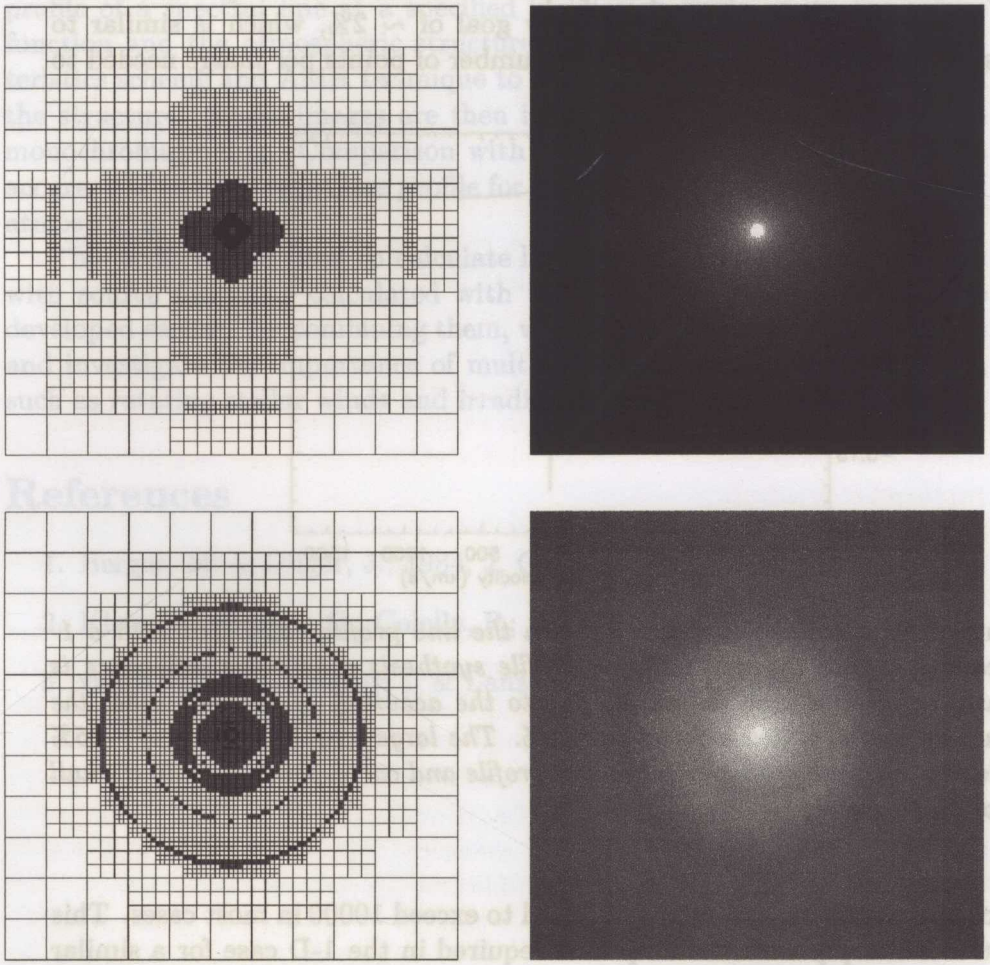

Figure 3.3: *Adaptive Mesh Refinement for the same stellar structure and source function (see text), in the continuum (top) and at flux maximum (bottom). The left column shows the grid cells used in the calculation, the right column is an image of the log of the monochromatic intensity of the object at the specified frequency, normalized to the maximum intensity in the continuum.*

refinement levels or accuracy goal. The large difference around the line centre is due to the large gradient in the line profile and corresponds to only a small difference in frequency space. The difference may well be from the 1-D code, which had an accuracy goal of $\sim$ 2%, which is similar to most of the difference observed. The number of points per image needed to

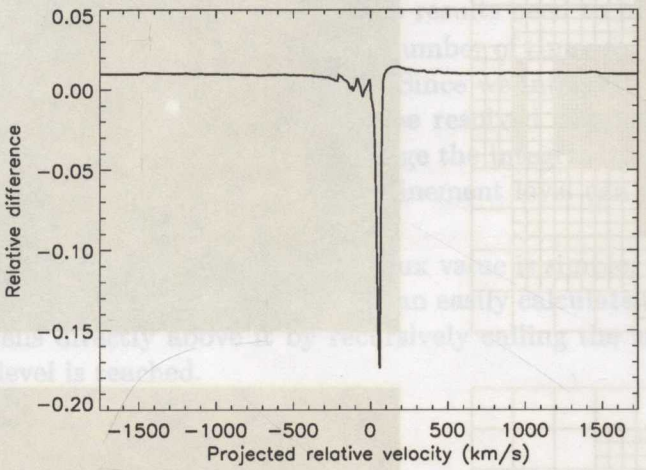


Figure 3.4: *Relative difference between the line profile calculated with a 1-D code and with the multi-D line profile synthesis code. The difference is clearly small and may in fact be due to the accuracy of the 1-D code, the accuracy goal of which was set to* $\sim$ *1%. The large local difference of* $\sim$*15% is due to the large gradient in the line profile and corresponds to only a small error in frequency.*

reach this accuracy, however, was found to exceed 10000 in most cases. This contrasts sharply with the 50 points required in the 1-D case for a similar accuracy, and indicates that for steep gradients surrounding a slowly varying plateau, as is the case in the continuum, the AMR technique is not very efficient.

As no effort has been made to optimize the code, the numerical load is substantial, as can easily be inferred from the large number of points needed per image. The time it takes to render one image obviously depends strongly on the contrast within the image and the accuracy required. On average, a single monochromatic image of around 10000 points takes approximately 1 minute on a 1.7 GHz Pentium 4, so that several hours are needed to generate a single line profile of a few hundred frequency points.

## 3.6 Conclusion

The code presented here is able to very accurately calculate the emergent profile of a spectral line at a specified inclination angle, given the source function and the atmospheric structure. The code uses the long characteristics scheme and AMR technique to generate monochromatic images of the structure. These images are then integrated to calculate the emitted monochromatic flux. Comparison with 1-D models indicates an excellent accuracy of the emergent line profile for identical given source function and atmospheric structure.

This code will be used to calculate line profiles of 2-D and 3-D objects with source functions calculated with the 2-D short characteristics code developed earlier. By combining them, we can generate reliable line profiles and investigate the importance of multi-D effects on extended structures, such as rotating stellar winds and irradiated accretion/excretion disks.

## References

1. Berger, M. & Oliger, J.; 1984, J. Comp. Phys., **53**, 484
2. Klein, R.; McKee, C.; Colella, P.; 1994, ApJ., **420**, 213
3. van Noort, M., Hubeny, I. & Lanz, T., 2002, ApJ, **568**, 1066

# Chapter 4

# NLTE Radiative Transfer in Rotating Winds

**We apply the 2D Short Characteristics and the line profile synthesis codes, presented in chapters 2 and 3, to the problem of rotating stellar winds. We use the codes to calculate the line profiles of a set of resonance lines of different strengths for a star representative of stellar type B0 and investigate the direct effect of rotation on the line profile and radiation force. We then investigate the effect of deformation of the wind structure due to rotation on the line profile and the radiation force. The deformation of the stellar surface was found to change the results qualitatively and was therefore included in the models. The changes in the normalized line profiles were found to be surprisingly small, with a maximum change at 90% of the breakup rotation rate of $\sim 20\%$. The effect of the rotation on the non-radial radiation force were found to be of a similar magnitude, with maxima in the latitudinal and tangential radiation forces of $\sim 0.17$ and $\sim 0.05$ times the radial radiation force respectively.**

## 4.1 Introduction

The first reported realization of the rotation of the sun were inferred from observations of the movement of sunspots across the solar disk on July 13, 1611 by Fabricius (Germany, 1587-c.1617). The rotation of stars other than the sun was subsequently the subject of many studies and discussions, but the actual detection of rotation in stars other than the sun was not possible until the arrival of modern astronomical observing techniques in the early parts of the 20th century (Tassoul, 2000).

Thanks to a vast body of work dedicated to stellar rotation, spanning many decades, we now know that in fact many stars rotate at appreciable velocities (see Tassoul, 2000, for a nice review of the history of the field). The average rotation rate peaks in late A type stars at a period of $\sim 1.3 \cdot 10^{-4}\,\mathrm{rad\,s^{-1}}$ or about 14 hours, whereas the average equatorial velocity peaks at early B type stars at around $200\,\mathrm{km\,s^{-1}}$ (McNally, 1965), however, individual stars have been observed to rotate at velocities up to $400\,\mathrm{km\,s^{-1}}$.

The theory of the stellar evolution of rotating stars was developed over a period of many decades by a large group of individuals, although the observational consequences of many theoretical models were difficult to verify due to observational limitations. A significant step forward was made by the development of helioseismology in the 1980s (Bonnet, 1983; Deubner & Gough, 1984), which provided the first look into the interior of the sun. It is now possible to measure the velocity distribution *inside* a star, making direct comparison with theoretical models possible.

Measurements of the angular velocity inside the sun are consistent with rigid rotation (Tassoul, 2000), which is perhaps not surprising, as the mantle of the sun is convective and quickly levels velocity gradients. Although the distance prohibits spatially resolving most stars other than the sun, and the flux levels are still a limiting factor, stellar seismology is now being developed as a new tool to derive information about the interiors of stars other than the sun. Observational data of more massive stars with radiative envelopes are also consistent with rigid rotation, and several instability mechanisms have been proposed by which sufficient mixing could be generated to explain this, of most of which the time scale is still quite uncertain.

Observationally, it is difficult or, in most cases, impossible, to determine the true rotation rate of a star from the spectrum alone, as the rotational velocity is projected onto the line of sight, i.e. $V_p = V_\varphi \sin i$, which depends on the unknown inclination angle $i$. Even if a star is observed to be slowly rotating, it may in fact be rotating at a significant rotation rate, but viewed

pole-on (i.e. $i = 0$). It is, however, not clear how this "unseen" rotation affects other properties determined from the line profiles in the spectrum, such as mass loss rate, surface gravity, etc.

The way one historically included rotational effects in emergent line profiles, was to convolve the emergent flux with a rotational broadening kernel (Mihalas & Auer, 1970). Although this is a good approximation for 1-D plane-parallel atmospheres, in extended atmospheres with differential rotation this may be far from correct for strong lines. In order to quantify the error introduced, the radiative transfer in the stellar atmosphere needs to be calculated in 2-D with rotational symmetry, or in 3-D.

In chapter 2 we presented a code that can solve the transfer equation for a 2-level atom in 2 dimensions under rotational symmetry in Cartesian, cylindrical and spherical coordinates. It uses the short characteristics scheme and was specifically designed to treat large velocities, such as those occurring in stellar winds, accurately. We set out to calculate the properties of the radiation field in rotating stellar winds with this code, and to calculate the emergent line profiles as a function of inclination angle. In section 4.3 the assumptions and methods we use to construct the structure of a rotating stellar wind are explained, in section 4.4.1 we test the accuracy of the code for the conditions we encounter in our model atmospheres, and we discuss the results in section 4.4.

## 4.2 Line formation in stellar winds

Before dealing with rotation effects in stellar winds, it is perhaps appropriate to examine the physics of a non-rotating stellar wind.

The atmospheres of massive stars are fundamentally different from those of less massive stars in that the radiation pressure at the surface is large enough to lift material off the surface and accelerate it beyond the escape velocity. This creates a stellar "wind", which can extend the atmosphere of the star by several times the stellar radius (i.e. the radius of the base of the wind). The acceleration of the wind results mainly from the radiative driving of a large number of weak lines (Lucy & Solomon 1970, Castor, Abbott & Klein, 1975; Abbott 1982; Pauldrach, Puls & Kudritzki 1986), of all ion species present in the wind.

The formation of spectral lines in extended atmospheres is fundamentally different from that in plane-parallel atmospheres. Where the formation of a spectral line profile in the plane-parallel case is usually the result of radiative transfer effects only, the emergent line profile from an extended

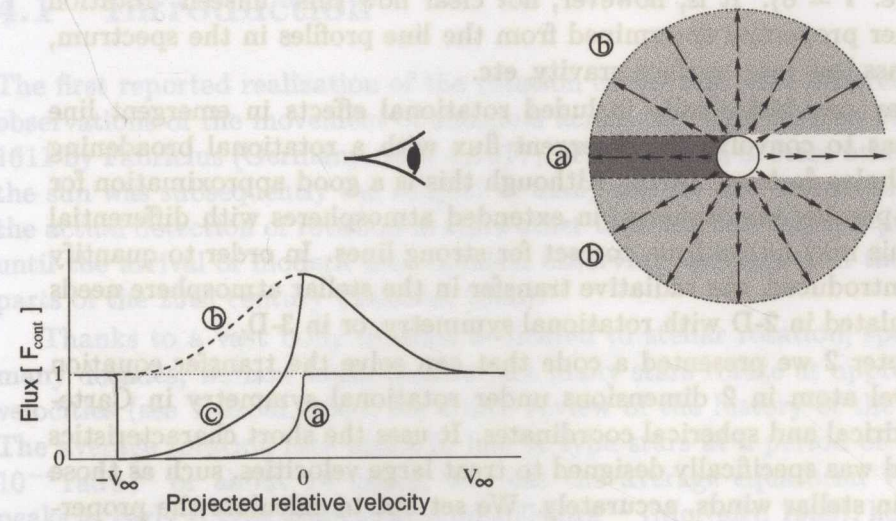


Figure 4.1: *Formation of a strong spectral line in an extended wind (after Lamers & Cassinelli, 1999). The emission line from region b) and the absorption line from region a) combine to form line c).*

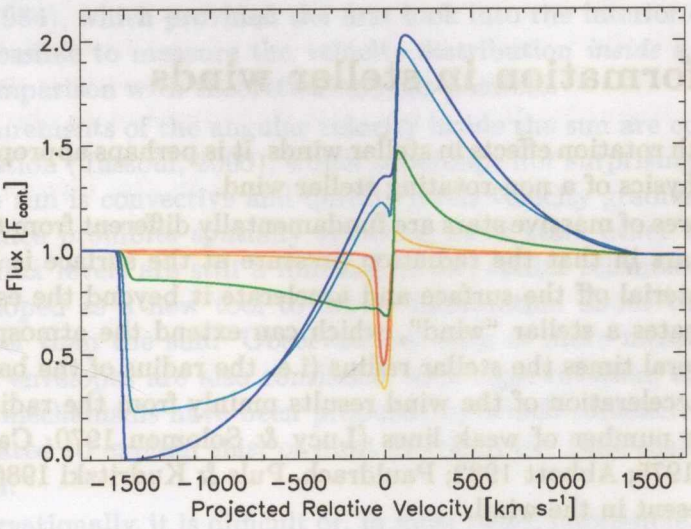


Figure 4.2: *Line profiles for a star with* $M = 8.2\,M_\odot$, $R = 8.4\,R_\odot$, $\dot{m} = 3 \cdot 10^{-7}\,M_\odot\,y^{-1}$ *and* $V_\infty = 1500\,km\,s^{-1}$, *for lines with continuum to line opacity ratio,* $r_{cl}$, *of approximately* **5**, **50**, $5 \cdot 10^2$, $5 \cdot 10^3$, $\mathbf{5 \cdot 10^4}$.

atmosphere can be determined by geometrical projection effects as well as radiative transfer effects.

The classical way to describe the formation of a strong spectral line in an extended stellar wind, is by regarding the star and the wind as separate entities (see Figure 4.1). The star radiates as normal in the continuum, providing a central source of radiation for the wind. The wind is optically thick in the line, and therefore blocks radiation at the line frequency coming from the star. However, since the material is moving outward, the frequency at which the continuum radiation is blocked is Doppler-shifted to higher frequency in the observers frame. As the wind is gradually accelerated from low velocities to $V_\infty$, the absorption from the wind cuts out a wide absorption trough in the observers frame from $v = 0$ to $v = V_\infty$ with respect to the line frequency.

At the same time, the wind radiates at the line frequency, but at a much lower intensity level than the continuum. Since the wind is much more extended than the star, this intensity is scaled up by the geometrical projected surface area, thus providing a significant or even dominant contribution to the line profile. This contribution is spread in frequency due to Doppler shifting of the local line profile, between $-V_\infty$ and $V_\infty$ in the observers frame with respect to the line frequency.

The addition of these two contributions results in the classical P-Cygni profile (see Figure 4.1, left).

To get a good reference solution for the results from the 2-D code, a 1-D spherical, 2-level atom, long characteristics, ALI, AMR code, was specifically written for this purpose. As the code was developed to provide an essentially "exact" solution, an adaptive mesh refinement technique was used along the long characteristics, as well as for the angular grid. This ensures good control over the error in the solution, which was set to approximately 1%.

The normalized line profiles, calculated with the spherical 1-D code, are plotted for a number of line strengths in Figure 4.2. The strongest lines clearly show the classical P-Cygni line shape, but for weaker lines, transition forms between the classical profile shape and the usual absorption profile can be seen.

## 4.3 Rotating stellar winds

To calculate the structure of a rotating star, requires the modeling of the entire star, not just the atmosphere, as the star deforms as it rotates. This

is a complex undertaking, even when treating the radiation transport only approximately, as the interior structure of the star develops complex circulation patterns. Additionally, the radiative acceleration of material at the surface is unstable, resulting in an inhomogeneous, time dependent, 3-D structure (see for instance Owocki & Puls, 2002). Needless to say, we are currently not able to deal with this, and we will therefore use approximate model atmospheres, based on a stationary, time-independent model.

Much work has been done on modelling the time-independent structure of stellar winds, with varying degrees of sophistication. Although the line driving mechanism of the wind as described by Castor, Abbott & Klein (1975) and Abbott (1982) is 1-D and therefore cannot include rotation effects, a modified 1-D formulation approximately including the effect of rotation, but excluding deformation of the star has been developed by Friend & Abbott (1986).

Although this method appears to be in good agreement with observations, it underestimates the mass loss and wind properties of the most massive stars. Much work has been done by Pauldrach (1985), Friend, Poe & Cassinelli (1987) and Cassinelli (1991), among others, to improve this situation, but rotation in massive stars has a great influence on the wind structure (see for instance Bjorkman & Cassinelly 1993, Owocki, Cranmer & Blondin 1994, Owocki, Cranmer & Gayley 1998 Maeder 1999 and Maeder & Meynet 2000) and requires a multidimensional treatment.

In the following, we will try to construct an approximate analytic 2-D model of the stellar wind of a rotating massive star. The aim is to generate a structure, suitable for solving the radiative transfer equation and derive theoretical line profiles, but without simultaneously solving the MHD equations and the radiation transfer self-consistently.

The most obvious change in a star when it rotates is that it becomes oblate. Due to the change in the effective gravity caused by the rotation, more material is needed to generate the same pressure at the equator than at the poles. We can assume that surfaces of equal gravitational potential have equal pressure, as otherwise the pressure gradient would accelerate material along equipotential surfaces until the pressure *is* constant. If we assume that the surface of the star is defined approximately by a surface of equal pressure, the radius of the star can be calculated by equating the centrifugally reduced gravitational potential at colatitude $\theta$ to the gravitational potential at radius of the star at the pole, $R_p$, at which location we assume that the effect of the rotation on the star is negligible, i.e. $R_p = const.$, which seems to be a good approximation from more sophisticated models

(Papaloizou & Whelan 1973, Maeder & Meynet 2000). We thus have

$$-\frac{GM}{R_p} = -\frac{GM}{R} - \frac{1}{2}(\Omega R \sin\theta)^2, \tag{4.1}$$

where we neglect the reduction in the gravity by the radial component of the radiation force.

From the structure of (4.1), we can infer that there are two types of solution: one where the first term on the right hand side dominates the second term, and another where the second term on the right hand side dominates the first. Physically it is evident that the first type of solution is bound, the gravitational term dominates, whereas the second type is not, the centrifugal term dominates. In the latter case, there must be a positive and a negative solution, as only the square of the centrifugal term enters the dominant part of the equation. Moreover, since the gravitational term *decreases* with radius, whereas the centrifugal term *increases* with radius, for a given value of $\Omega \sin\theta$ the bound solution will be the one having the smallest positive value of $R$.

The general theory of cubic equations tells us (see Numerical Recipes in C, p184) that if for the cubic equation:

$$x^3 + ax^2 + bx + c = 0 \tag{4.2}$$

the quantities

$$U = \frac{2a^3 - 9ab + 27c}{54} \tag{4.3}$$

and

$$V = \frac{a^2 - 3b}{9} \tag{4.4}$$

are computed, for $U^2 < V^3$, there are three real roots, otherwise only one real and two complex roots. From the above reasoning, the real radius of the star is thus given by the real solution with the smallest positive value.

At the critical point $U^2 = V^3$, bound and unbound solutions are indistinguishable, i.e. the bound solution itself becomes unbound. This occurs first at the equator ($\theta = \pi/2$), at the lowest value of $\Omega$ for which this can happen, the *breakup* rotation rate $\Omega_{br}$. For (4.1), since $a = 0$, $U = c/2$ and $V = -b/3$, this gives

$$\Omega_{br} = \sqrt{\frac{8GM}{27R_p^3}}. \tag{4.5}$$

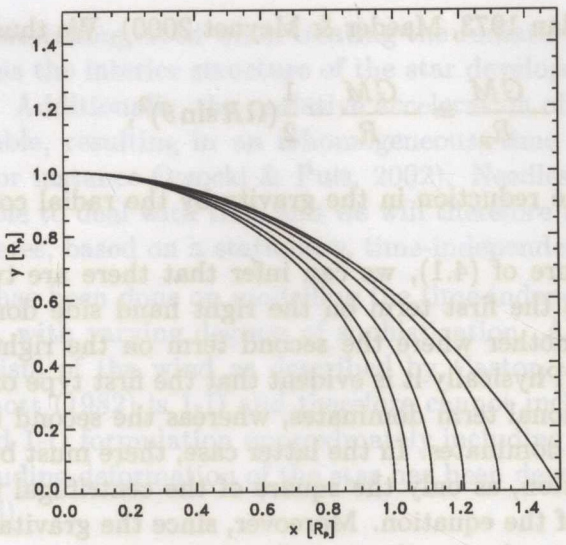


Figure 4.3: *Stellar surface for different rotation rates (from inside out: 0,0.5,0.75,0.90,0.97 and 0.999 $\Omega_{br}$) for a $M = 15\,M_\odot$, $R_p = 16\,R_\odot$ star.*

The corresponding breakup velocity at the equator is easily found by substitution of the above in (4.1):

$$V_{br} = \frac{3}{2}\Omega_{br} R_p = \sqrt{\frac{3GM}{4R_p}}. \tag{4.6}$$

The radius of a $M = 15\,M_\odot$, $R_p = 16\,R_\odot$ rotating star (see §4.4) is plotted in Figure 4.3 for a number of rotation rates. Due to the deformation of the surface, the rotation velocity is not simply proportional to $\Omega R_*$, but instead increases faster. This effect is shown in Figure 4.4, where the equatorial rotation velocity is plotted as a function of $\Omega/\Omega_{br}$. It is clear that from around $0.5\,\Omega_{br}$ the linear relation breaks down, and the rotation velocity is no longer adequately described by $V_\varphi(\theta) = \Omega R_* \sin\theta$. At $\Omega = \Omega_{br}$, the rotation velocity is $1\frac{1}{2}$ times larger than if the deformation is not taken into account.

If the effect of radiation is included, the value of the breakup rotation rate is not so easily found, and in fact depends on many factors (see Maeder 2000 for a discussion). The main reason for this is that the deformation of the stellar surface is not the only effect the rotation has on the star. Due to the rotation, the effective gravity at the surface decreases toward the

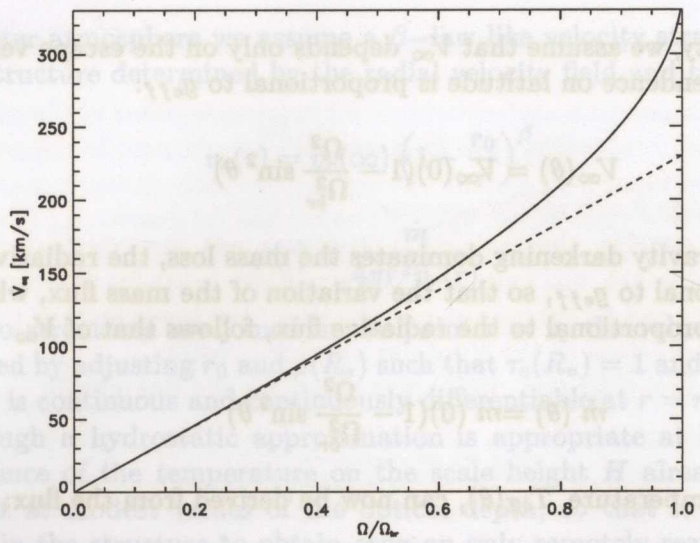


Figure 4.4: *Equatorial rotational speed as a function of rotation rate for a* $M = 15\,M_\odot$, $R_p = 16\,R_\odot$ *star. The dotted line is the limit without deformation,* $V_\phi = \Omega\, R_*$

equator as

$$g_{eff}(\theta) = \frac{GM_*}{R_*^2}(1 - \frac{\Omega^2}{\Omega_{br}^2}\sin^2\theta) \tag{4.7}$$

if the effect of radiative acceleration is neglected.

There are several wind properties that are affected by this and change as a function of lattitude:

1. According to the theory of line driven winds (CAK 1975), observationally confirmed by Abbott in 1978 and later improved by Abbott (1982) and Pauldrach, Puls & Kudritzki (1986), $V_\infty$ scales as $V_{esc}$ (and thus with $g_{eff}$). $V_\infty$ therefore decreases towards the equator;

2. The decrease in $g_{eff}$ leads to an increase in $\dot{m}$ towards the equator (Friend & Abbott, 1986);

3. Owocki & Gayley (1997) and Owocki, Cranmer & Gayley (1998) found that the increase in gravity darkening (von Zeipel, 1924) at the equator leads to a decrease in $\dot{m}$.

Although effects 2 and 3 are competing, a recent analysis by Maeder (1999) indicates that 3 will dominate $\dot{m}$, unless a strong increase in opacity, due to the bi-stability jump (Lamers, Snow & Lindholm 1995), occurs.

For simplicity, we assume that $V_\infty$ depends only on the escape velocity, so that the dependence on latitude is proportional to $g_{eff}$:

$$V_\infty(\theta) = V_\infty(0)(1 - \frac{\Omega^2}{\Omega_{br}^2}\sin^2\theta) \tag{4.8}$$

Assuming gravity darkening dominates the mass loss, the radiative flux is also proportional to $g_{eff}$, so that the variation of the mass flux, which is assumed to be proportional to the radiative flux, follows that of $V_\infty$

$$\dot{m}\ (\theta) = \dot{m}\ (0)(1 - \frac{\Omega^2}{\Omega_{br}^2}\sin^2\theta) \tag{4.9}$$

The effective temperature, $T_{\rm eff}(\theta)$, can now be derived from the flux:

$$T_{\rm eff}(\theta) = T_{\rm eff}(0)(1 - \frac{\Omega^2}{\Omega_{br}^2}\sin^2\theta)^{\frac{1}{4}} \tag{4.10}$$

With these assumptions, we generated the 2-D model atmospheres for our radiatively driven, rotating stellar winds. However, the parameterizations are clearly only approximately valid. For a detailed, quantitative determination of the structure of a rotating star, a detailed evaluation of the structural equations for the whole star is needed.

### 4.3.1 Generating a model atmosphere

We want to investigate the effect of rotation on the line spectra of and radiation forces in a rotating stellar wind. Although we can calculate the line transfer on a fixed structure, this structure is not explicitly known but depends on the radiation field itself. Since calculating a self-consistent solution is beyond the scope of this work, we will instead assume in the following that the influence of the line on the structure is negligible and that all the relevant properties of the structure are known and fixed during the calculations.

In the inner atmosphere, we assume hydrostatic equilibrium, where the velocity of the outflow is determined by the density and the mass loss rate:

$$\rho(r) = \rho(R_*)\mathrm{e}^{-(r-R_*)/H(T_{eff})} \tag{4.11}$$

$$v_r(r) = \frac{\dot{m}}{4\pi r^2 \rho(r)} \tag{4.12}$$

In the outer atmosphere we assume a $\beta-$law like velocity structure and a density structure determined by the radial velocity field and the mass loss rate:

$$v_r(r) = v_r(\infty)\left(1 - \frac{r_0}{r}\right)^{\beta} \tag{4.13}$$

$$\rho(r) = \frac{\dot{m}}{4\pi r^2 v_r(r)} \tag{4.14}$$

These two structures are joined in the point $r = r_c$ the value of which is determined by adjusting $r_0$ and $\rho(R_*)$ such that $\tau_c(R_*) = 1$ and the velocity structure is continuous and continuously differentiable at $r = r_c$.

Although a hydrostatic approximation is appropriate at large depth, the influence of the temperature on the scale height $H$ already becomes important at modest values of the optical depth, so that it needs to be included in the structure to obtain even an only remotely realistic model. We therefore numerically integrate a simple system of hydrostatic equations from $r = r_c$, at which point we also know $\partial\rho/\partial r$, to the inner boundary:

$$\frac{\partial \rho}{\partial r} = -\rho/H(r), \tag{4.15}$$

$$H(r) = \frac{4kT(r)}{3\mu g_{eff}} \tag{4.16}$$

and

$$T(r) = T_{eff}\left(\frac{3}{4}(4\tau_R(r) + q(4\tau_R(r)))\right)^{\frac{1}{4}} \tag{4.17}$$

repeatedly until the system is internally consistent. Since $T(r)$ is dependent on the radiation field and therefore not known, we parameterized it with an LTE temperature (Mihalas, 1978). The Rosseland opacity $\alpha_R$ is calculated from OPAL tables (Iglesias & Rogers, 1991) and the local density for a solar metalicity stellar atmosphere. The factor 4 increase in the Rosseland optical depth that was used to calculate the temperature was determined by fitting the temperature to that of a 1-D stellar wind model calculated with the stellar wind code CMFGEN (Hillier & Lanz, 2001).

To generate a 2-D atmosphere, a series of 1-D atmospheres were calculated for different latitudes, i.e. all effects of latitudinal gradients on the structure are neglected. Each atmosphere is calculated with the appropriate value for $R_*$, $V_\infty$ and $\dot{m}$, according to the latitudinal dependence of these quantities as described in the previous section.

For the rotation velocity, a Keplerian velocity law was taken, assuming rigid rotation of the star:

$$v_\phi(r,\theta) = \Omega_* R_* \cos(\theta)\frac{R_*}{r} \tag{4.18}$$

where the lattitude $\theta = 0$ at the equator.

For the line opacity, the ionization structure was not considered, but rather the line strength was calculated from a fixed value for the oscillator strength $f = 0.25$ and by taking the population of the lower level of the line to be a specified fraction of the total ion number density.

A Voigt function (Mihalas, 1978) was taken for the line profile

$$\varphi(a,v) = \frac{H(a,v)}{\sqrt{\pi}\Delta\nu_D} \tag{4.19}$$

with

$$a = \frac{\gamma_{rad} + \gamma_{col} N_e}{4\pi\Delta\nu_D}, \tag{4.20}$$

$$v = \frac{\nu - \nu_0}{\Delta\nu_D}, \tag{4.21}$$

$\Delta\nu_D$ is the Doppler width of the line, $N_e$ the electron density and the usual radiative and electron collisional damping factors $\gamma_{rad} = 2.6 \cdot 10^8\,\mathrm{s}^{-1}$ and $\gamma_{col} = 7.6 \cdot 10^{-7}\,\mathrm{cm}^3\,\mathrm{s}^{-1}$, appropriate values for strong resonance lines.

In realistic problems, however, the line strength is unlikely to be uniform, even in a 1-D atmospheric structure, and detailed calculations are needed to determine the correct occupation numbers of the upper and lower energy levels of the atomic transition.

For the continuum opacity, we included only electron scattering, H and He bound-free opacity (Kramers formula) and electron-ion free-free opacity using (Rybicky & Lightman, 1979)

$$\alpha_{ff} = 3.7 \cdot 10^8 N_e N_{ion} \frac{Z^2}{T^{\frac{1}{2}}\nu^3} g_{ff}, \tag{4.22}$$

in c.g.s. units, where $N_e$ and $N_{ion}$ are the electron and ion densities, $Z$ is the ionization stage, and $g_{ff}$ is a Gaunt factor of order unity.

Although the model atmospheres resulting from this procedure are not consistent with the radiation field, the structures are qualitatively similar to those from detailed 1-D calculations of winds of non-rotating massive stars (Hillier & Miller, 1998, Aufdenberg 2001). The results can therefore not be used for a quantitative comparison with observations, but rather they have to be regarded as a qualitative indicator of the changes in the radiation field and line profiles resulting from rotation.

## 4.4 Results

The results of the calculations can be divided in two main parts. The first is the importance of rotation for the emergent line profile for different viewing angles, i.e. how much does the line profile change as a function of rotation rate. This is important for the determination of the mass loss rate directly from the line profile assuming no rotation, and for the determination of the rotation velocity itself.

The second is the dependence of the radiation force in a rotating wind on the rotation rate. To this end we calculated the radiation force per unit volume directly from the intensity itself. We can only hope to verify the validity of the assumptions made in generating our models, as the aim of this qualitative study is not to generate fully self-consistent model atmospheres. The results will, however, give us a good indication of the behavior of the radiative forces driving the wind and the changes on it due to rotation effects.

We repeated the calculations for several line strengths, to investigate the importance of rotation for weak lines, important for the wind dynamics, as well as for strong lines, important for observations. Due to the decreasing effectiveness of the differential rotation with increasing distance to the stellar surface, the effects of the rotation on spectral lines is likely to be dependent on the line strength.

We have calculated the emergent line profiles and radiative acceleration for a 2-D atmospheric structure corresponding to a 15 $M_\odot$, 16 $R_\odot$ star with $\dot{m}\ (0) = 10^{-6}\,M_\odot\,y^{-1}$, $T_{\rm eff}(0) = 35000\,K$, $V_\infty(0) = 1500\,km\,s^{-1}$ and $\beta = 1.0$. We also adopted a constant turbulent velocity broadening of the line of $25\,km\,s^{-1}$, to reduce the number of frequency points needed in the calculations.

This relatively massive star, which can be thought of as representative for spectral type B0, was chosen as the most likely candidate for large spectroscopic effects, as the observed rotational surface velocity peaks around this spectral type, and the stellar atmosphere is already quite extended, even for moderately strong lines.

The mass was taken representative for spectral type B0 (McNally, 1965) The radius corresponding to this mass for main sequence type stars is about 8 $R_\odot$. However, the gravity at the surface with this radius results in a large density gradient, which could not be resolved on a spherical grid for rotationally deformed stars (see also §4.4.3). For this reason, the radius was taken to be twice as large.

The line opacity was calculated for 4 representative line strengths by taking the population of the lower energy level of the line to be $10^{-9}$, $10^{-8}$, $10^{-7}$ and $10^{-6}$ of the total number density (the yellow, green, cyan and blue profiles from Figure 4.2), hereafter line strength **a**, **b**, **c** and **d** respectively. They correspond to a continuum to line opacity ratio, $r_{cl}$, of approximately $5 \cdot 10^1$, $5 \cdot 10^2$, $5 \cdot 10^3$ and $5 \cdot 10^4$ respectively.

The calculations were carried out on 24 2 GHz PCs, taking about 24 hours (20 minutes per ALI for approximately 70 iterations) to convergence. We used a spherical grid with $N_\theta \times N_r = 25 \times 60$, $31 \times 75$ and $35 \times 90$ points for $\Omega = 0.5$, 0.75 and $> 0.85$ times $\Omega_{br}$ respectively. The angular points were automatically selected by the program at startup, dedicating half the total number of points to sample the radius of the star in the continuum, the other half is distributed homogeneously over the $4\pi$ solid angle. The stopping criterion is set to be a maximum relative change of any quantity anywhere on the grid less than $10^{-3}$ between two consecutive ALI.

### 4.4.1 Accuracy of the short characteristics method

Before proceeding to actual calculations, it is important to verify that the short characteristics method can be used in situations where very large velocity differences exist between adjacent points on the grid. Although great care has been taken to ensure accurate resolution of all relevant quantities within a cell, no such guarantee can be made regarding the intensity interpolations, needed at the intersection of each ray with the grid cell, under these circumstances.

Therefore, the line source function for our model, without rotation, was calculated in 1-D with a spherical long characteristics code, specifically written for this purpose, and in 2-D with the 2-D short characteristics code. As the long characteristics method does not suffer from intensity interpolation related numerical effects, this is a good test for determining the error introduced by the intensity interpolations needed by the short characteristics method. A comparison of the relative difference of the 1-D and 2-D source functions for line strength **b** is shown in Figure 4.5.

Although the difference may seem excessive, with errors of 30% or more, a closer inspection of the problem itself reveals that the errors are only significant in regions that are very optically thin for the line under consideration. The resulting error in the emergent line profiles is therefore significantly smaller, and has not been observed to exceed 5% in our tests.

The errors are mainly due to the accumulation of interpolation errors and numerical diffusion due to limitations in the resolution. Although the

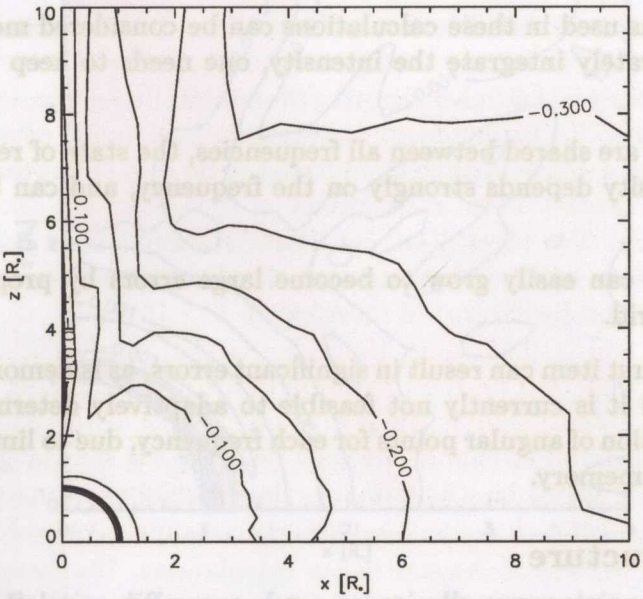


Figure 4.5: *Relative difference between the 1-D and 2-D line source functions for line strength* **b** *for identical, spherically symmetric structures without rotation.*

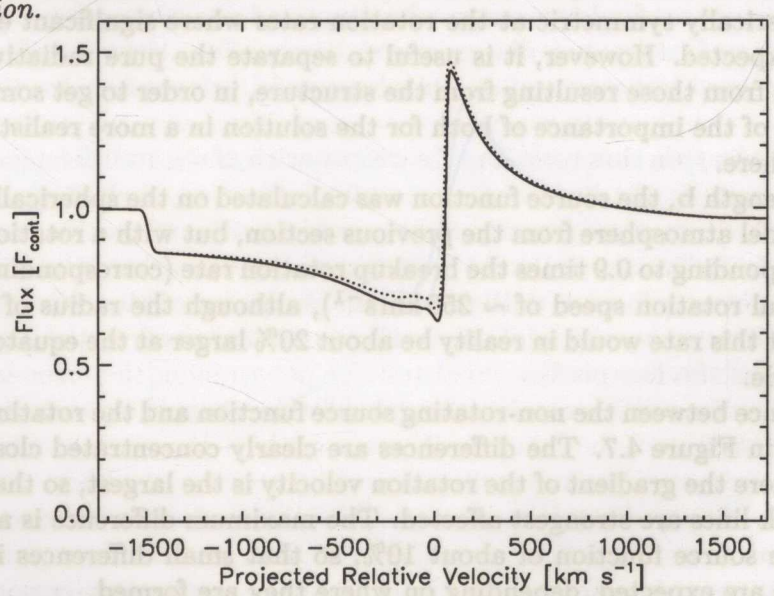


Figure 4.6: *Comparison between the 1-D (dotted) and 2-D (solid) line profiles for line strength* **b** *for identical, spherically symmetric structures without rotation.*

angular resolutions used in these calculations can be considered more than sufficient to accurately integrate the intensity, one needs to keep in mind that

1. as all angles are shared between all frequencies, the state of resolution of the intensity depends strongly on the frequency, and can be quite bad; and
2. small errors can easily grow to become large errors by propagation across the grid.

In particular the first item can result in significant errors, as is demonstrated in Figure 3.3, but it is currently not feasible to adaptively determine the optimum distribution of angular points for each frequency, due to limitations in CPU time and memory.

### 4.4.2 1D structure

In this section, we investigate the direct effect of rotation on the source function in a spherically symmetric underlying atmosphere and wind. This is mainly of academic interest, as the structure of the stellar wind is unlikely to remain spherically symmetric at the rotation rates where significant effects can be expected. However, it is useful to separate the pure radiative transfer effects from those resulting from the structure, in order to get some understanding of the importance of both for the solution in a more realistic model atmosphere.

For line strength **b**, the source function was calculated on the spherically symmetric model atmosphere from the previous section, but with a rotation velocity corresponding to 0.9 times the breakup rotation rate (corresponding to an equatorial rotation speed of $\sim 250\,\mathrm{km\,s^{-1}}$), although the radius of a star rotating at this rate would in reality be about 20% larger at the equator than at the pole.

The difference between the non-rotating source function and the rotating one is plotted in Figure 4.7. The differences are clearly concentrated close to the star, where the gradient of the rotation velocity is the largest, so that it is likely weak lines are strongest affected. The maximum difference is an increase in the source function of about 10%, so that small differences in the line profile are expected, depending on where they are formed.

The line profiles for 0°, 30° and 90° inclination are plotted in Figure 4.8. The differences between the non-rotating and 0° inclination profiles is fairly small, as expected from the small difference between the line source functions. The direct broadening effect of the rotation on the 30° and 90°

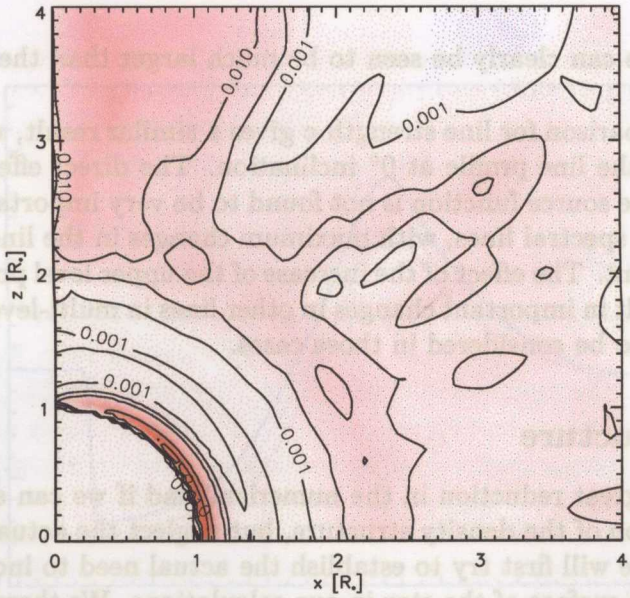


Figure 4.7: *Relative difference, for a spherically symmetric wind (see text), between the 1-D and 2-D line source functions for line strength* **b**. *The 2-D source function was computed with a rotation rate of 0.9 times* $\Omega_{br}$.

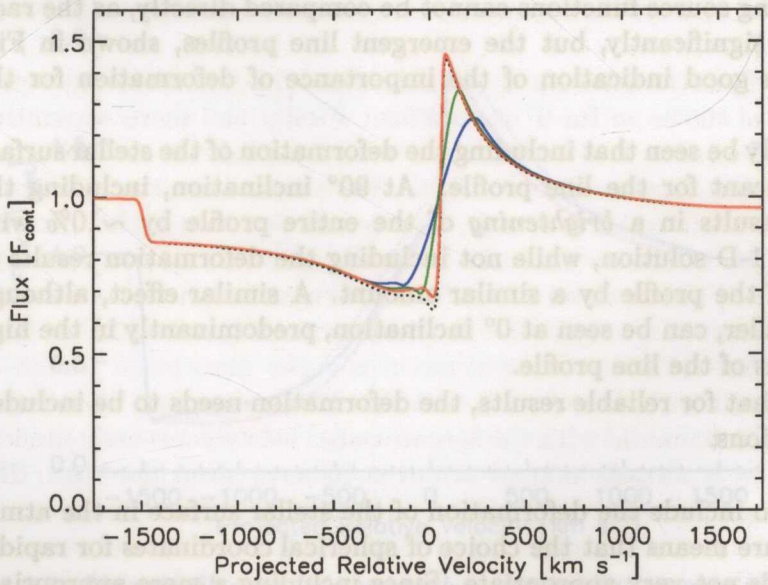


Figure 4.8: *Comparison between the 1-D (dotted) and 2-D line profiles, for a spherically symmetric wind (see text), for line strength* **b** *but with the 2-D rotating at 0.9 times* $\Omega_{br}$, *for* 0°, 30° *and* 90° *inclination.*

inclination profiles can clearly be seen to be much larger than the effect of the change in $S_l$.

A similar comparison for line strength **c** gives a similar result, with only small changes to the line profile at 0° inclination. The direct effect of the rotation on the line source function is not found to be very important in the formation of most spectral lines, with maximum changes in the line profiles of only a few percent. The effect of the increase of the upper level population can, however, result in important changes in other lines in multi-level atoms, and it still needs to be considered in those cases.

### 4.4.3 2D structure

As it would be a great reduction in the numerical load if we can assume a latitudinal variation of the density structure, but neglect the actual oblateness of the star, we will first try to establish the actual need to include the deformation of the surface of the star in our calculations. We therefore calculate the emergent line profile for our model with line strength **c**, rotating at 90% of the breakup rotation rate, both with and without including the deformation of the stellar surface.

The resulting source functions cannot be compared directly, as the radii of both differ significantly, but the emergent line profiles, shown in Figure 4.9, give a good indication of the importance of deformation for the whole wind.

It can clearly be seen that including the deformation of the stellar surface is quite significant for the line profile. At 90° inclination, including the deformation results in a *brightening* of the entire profile by ~10% with respect to the 1-D solution, while not including the deformation results in a *darkening* of the profile by a similar amount. A similar effect, although somewhat smaller, can be seen at 0° inclination, predominantly in the high velocity regions of the line profile.

It is clear that for reliable results, the deformation needs to be included in the calculations.

The need to include the deformation of the stellar surface in the atmospheric structure means that the choice of spherical coordinates for rapidly rotating stars is not very appropriate. Since including a more appropriate new coordinate system in the code is currently not feasible (but will be included in a future version of the code) the problems were calculated in spherical coordinates with increased resolution. To verify that the numerical error introduced by the new griddings is small, the same test as in the

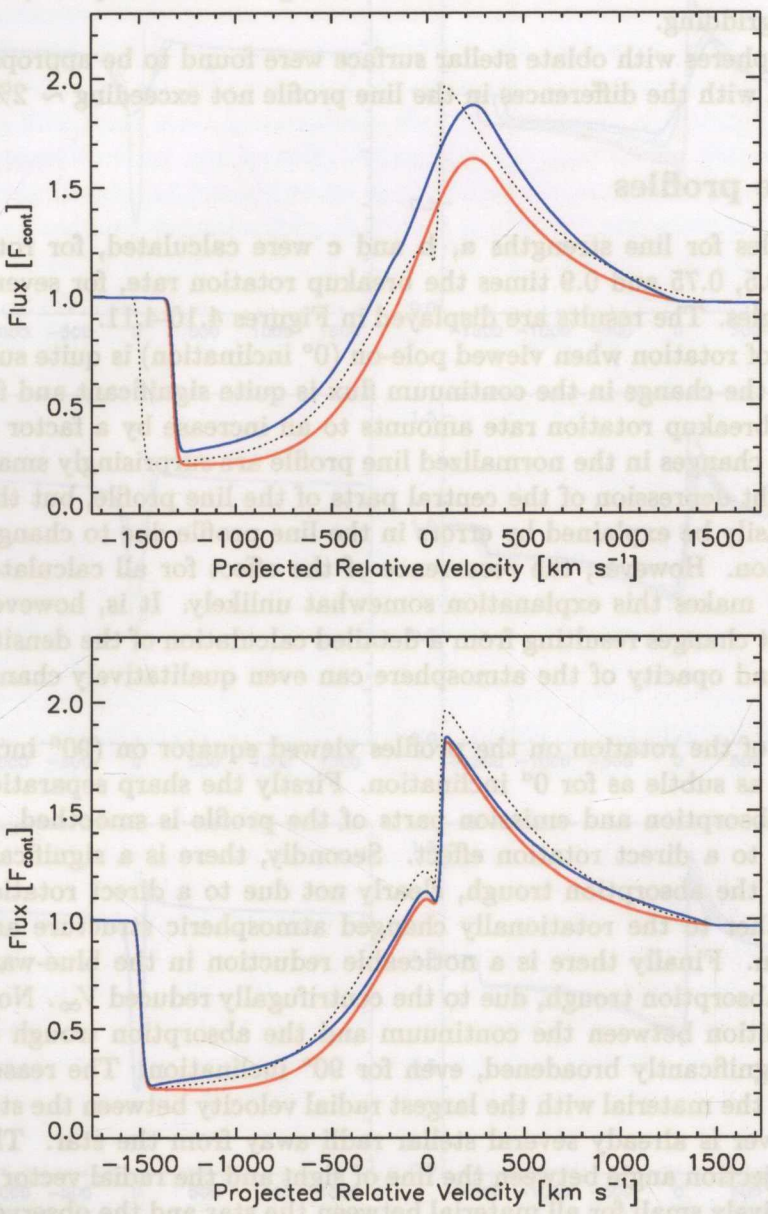


Figure 4.9: *Line profiles for line strength* **c**, *for a rotation rate of 0.85 times* $\Omega_{br}$, *without deformation (red) and including the deformation (blue) of the stellar surface, for* 90° *(top) and* 0° *(bottom) inclination.*

previous section was done for the same non-rotating model atmosphere, but with the new gridding.

The atmospheres with oblate stellar surface were found to be appropriately resolved, with the differences in the line profile not exceeding $\sim$ 2%.

### 4.4.4 Line profiles

The line profiles for line strengths **a**, **b** and **c** were calculated, for rotation rates 0, 0.5, 0.75 and 0.9 times the breakup rotation rate, for several inclination angles. The results are displayed in Figures 4.10-4.11.

The effect of rotation when viewed pole-on (0° inclination) is quite subtle. Although the change in the continuum flux is quite significant and for 0.9 times the breakup rotation rate amounts to an increase by a factor of about 1.5, the changes in the normalized line profile are surprisingly small. There is a slight depression of the central parts of the line profile, but this effect could easily be explained by errors in the line profile due to changes in the resolution. However, the recurrence of the effect for all calculated line strengths, makes this explanation somewhat unlikely. It is, however, very likely that changes resulting from a detailed calculation of the density, temperature and opacity of the atmosphere can even qualitatively change this result.

The effect of the rotation on the profiles viewed equator on (90° inclination) is not as subtle as for 0° inclination. Firstly the sharp separation between the absorption and emission parts of the profile is smoothed, as expected, due to a direct rotation effect. Secondly, there is a significant brightening of the absorption trough, clearly not due to a direct rotation effect, but rather to the rotationally changed atmospheric structure and source function. Finally there is a noticeable reduction in the blue-ward extent of the absorption trough, due to the centrifugally reduced $V_\infty$. Note that the transition between the continuum and the absorption trough at $-V_\infty$ is not significantly broadened, even for 90° inclination. The reason for this is that the material with the largest radial velocity between the star and the observer is already several stellar radii away from the star. The maximum projection angle between the line of sight and the radial vector is therefore relatively small for all material between the star and the observer, so that the rotational velocity projected onto the line of sight, and thus the rotational broadening, is also small.

The influence of the rotation depends noticeably on the line strength. The effect of rotation on the weaker lines is mostly to brighten the absorption region of the profiles. For stronger lines, the brightening of the absorp-

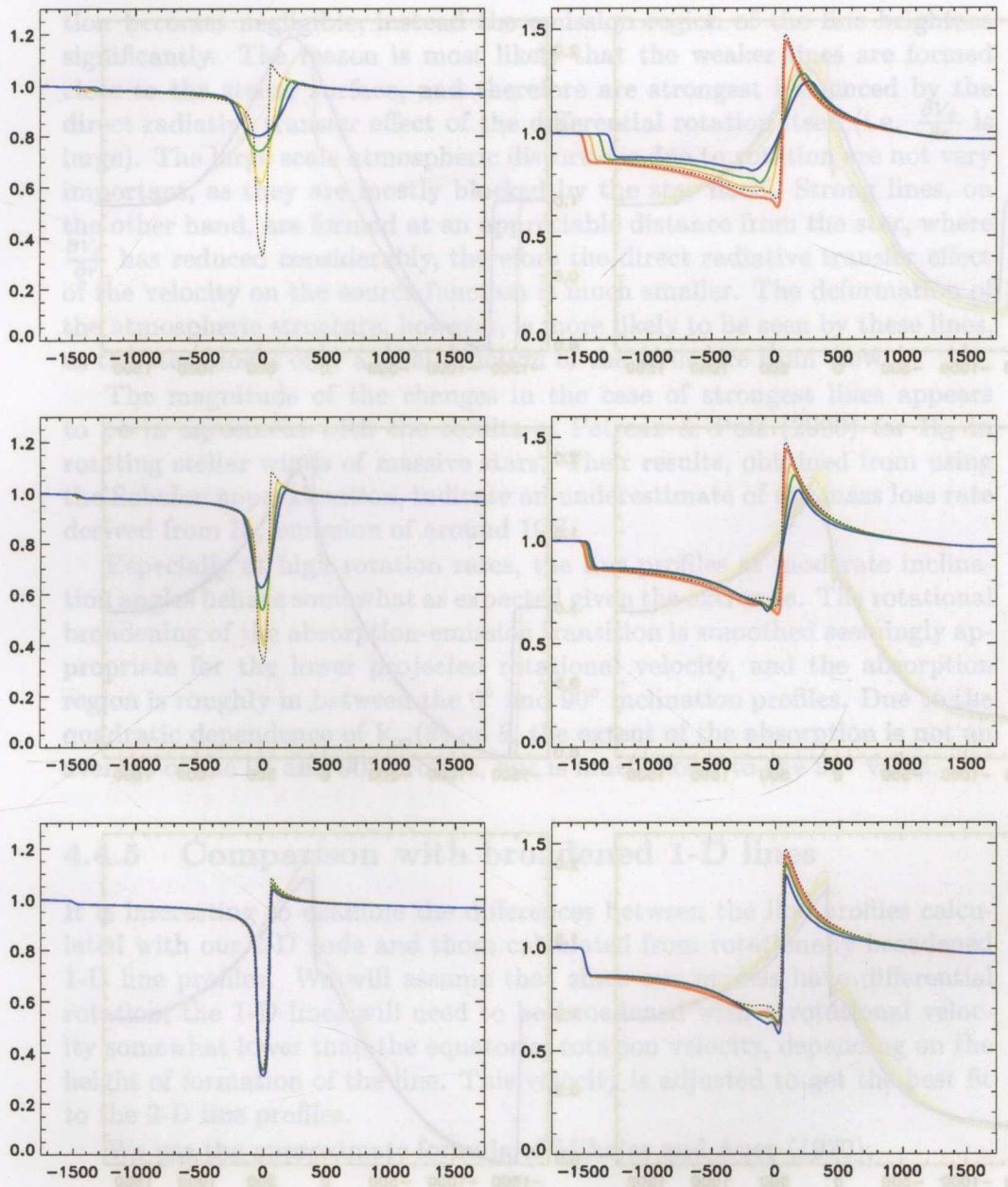


Figure 4.10: *Line profiles, normalized to the continuum, for* 90° *(top),* 60° *(middle) and* 0° *(bottom) inclination, for line strengths* **a** *(left) and* **b** *(right) for rotation rates* 0, 0.5, 0.75 *and* 0.9 *times* $\Omega_{br}$*, together with the corresponding 1-D profile (dotted).*

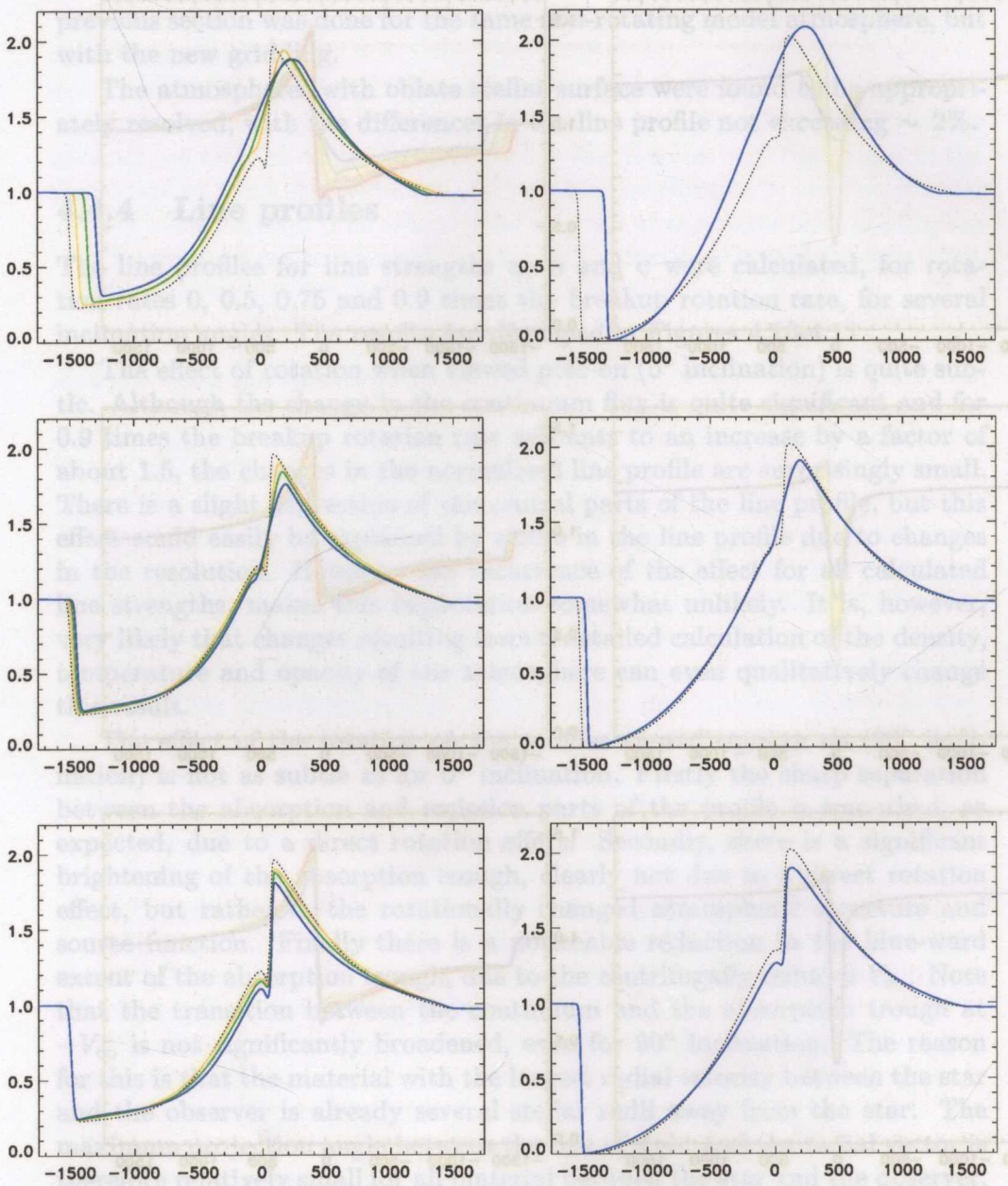


Figure 4.11: *Line profiles, normalized to the continuum, for* 90° *(top),* 60° *(middle) and* 0° *(bottom) inclination, for line strengths* **c** *(left) and* **d** *(right) for rotation rates* 0, 0.5, 0.75 *and* 0.9 *times* $\Omega_{br}$*, together with the corresponding 1-D profile (dotted).*

tion becomes negligible, instead the emission region of the line brightens significantly. The reason is most likely that the weaker lines are formed close to the stellar surface, and therefore are strongest influenced by the direct radiative transfer effect of the differential rotation itself (i.e. $\frac{\partial V_\phi}{\partial r}$ is large). The large scale atmospheric distortions due to rotation are not very important, as they are mostly blocked by the star itself. Strong lines, on the other hand, are formed at an appreciable distance from the star, where $\frac{\partial V_\phi}{\partial r}$ has reduced considerably, therefore the direct radiative transfer effect of the velocity on the source function is much smaller. The deformation of the atmospheric structure, however, is more likely to be seen by these lines, as the star blocks only a small fraction of the structure from view.

The magnitude of the changes in the case of strongest lines appears to be in agreement with the results of Petrenz & Puls (2000) for $H_\alpha$ in rotating stellar winds of massive stars. Their results, obtained from using the Sobolev approximation, indicate an underestimate of the mass loss rate derived from $H_\alpha$ emission of around 10%.

Especially at high rotation rates, the line profiles at moderate inclination angles behave somewhat as expected given the extremes. The rotational broadening of the absorption-emission transition is smoothed seemingly appropriate for the lower projected rotational velocity, and the absorption region is roughly in between the 0° and 90° inclination profiles. Due to the quadratic dependence of $V_\infty(\theta)$ on $\theta$, the extent of the absorption is not an average of the 0° and 90° profiles, but is much closer to the 90° value.

### 4.4.5 Comparison with broadened 1-D lines

It is interesting to examine the differences between the line profiles calculated with our 2-D code and those calculated from rotationally broadened 1-D line profiles. We will assume that since our models have differential rotation, the 1-D lines will need to be broadened with a rotational velocity somewhat lower than the equatorial rotation velocity, depending on the height of formation of the line. This velocity is adjusted to get the best fit to the 2-D line profiles.

We use the approximate formula of Mihalas and Auer (1970),

$$F_r(\lambda) \approx \frac{2}{\pi} \int_{-1}^{1} F(\lambda + \frac{v}{c}\lambda_0 x)\sqrt{1-x^2}\,\mathrm{d}x, \qquad (4.23)$$

where $F_r(\lambda)$ is the rotationally broadened flux and $F(\lambda)$ the unbroadened flux, to broaden the line profiles, as the 2% error level they quote is suffi-

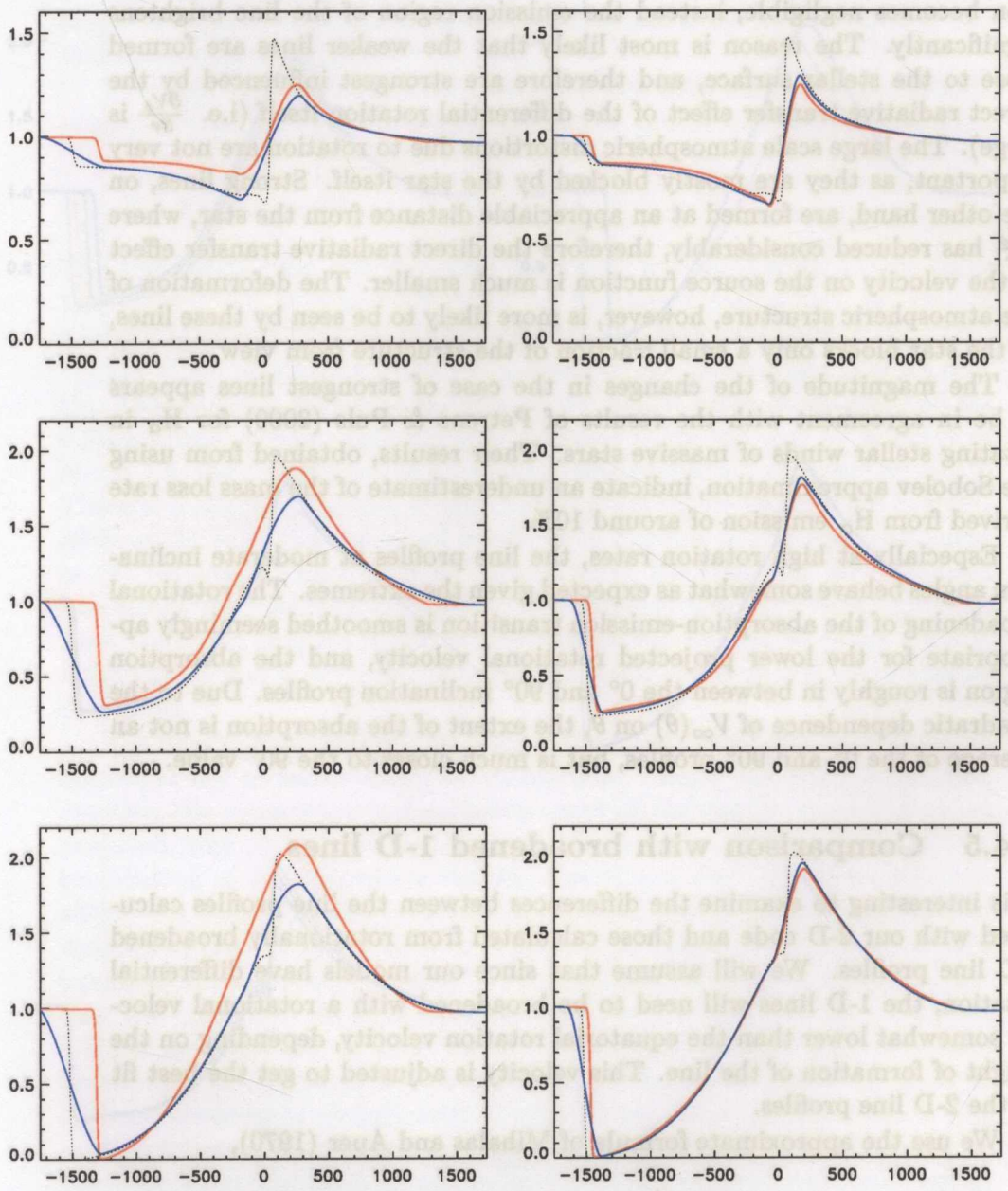


Figure 4.12: *Plots of the 2-D line profile and the corresponding 1-D rotationally broadened line profile at a rotation rate of 0.9 times $\Omega_{br}$ for line strength* **b** *(top),* **c** *(middle) and* **d** *(bottom), together with the corresponding 1-D line profiles (dotted) for* 90° *(left) and* 30° *(right) inclination.*

ciently small compared to the estimated errors in our profiles for a meaningful comparison.

The 1-D line profiles rotationally broadened in this way for a rotation rate of 0.9 times $\Omega_{br}$ are plotted in Figure 4.12, together with the unbroadened profiles and the corresponding 2-D profiles, for line strengths **b**, **c** and **d**. In most cases, the best fit (whenever that could be determined in a meaningful way) was for a velocity of $230\,\mathrm{km\,s^{-1}}$, about 10% lower than the true surface rotational velocity at the equator. The comparison for all the lines displayed is better than the error for an inclination angle of 30°, but quickly deteriorates for larger values.

The largest difference between the rotationally broadened 1-D profiles and the 2-D profiles follows from the brightening of the line profile reported in the previous section. Also, the broadening of the continuum-absorption transition is grossly overestimated, which is not seen in the 2-D profiles. The qualitative difference between the broadened 1-D and the 2-D profiles is, however, surprisingly small, with the most important feature being a shift in some absorption and emission features of at most a few $\mathrm{km\,s^{-1}}$ between the 1-D and 2-D profiles.

Quantitatively, the differences are typically of order 10-20%, even at 0.9 times the breakup velocity. This is surprising given the large amount of deformation of the stellar surface and the wind structure at this rotation rate. Larger effects seem possible for stronger lines, but given the accuracy of the code it seems likely that the errors would dominate the solution, and we leave this for a future study.

### 4.4.6 Radiation force

One of the important issues in stellar rotation is the effect of the rotation on the radiation force. This is important for the dynamics of the wind, which in turn affect the radiation field itself. However, since we only solve the transfer equation for a single resonance line on a fixed atmospheric structure, any forces derived from the calculation can only be checked against the input for consistency, as the total force on the material is an accumulation of all spectral lines in the atmosphere.

The radiation volume force per unit frequency was computed from the first moment of the transfer equation, the flux, times the local opacity (Mihalas, 1978)

$$f_\nu \mathrm{d}\nu = \frac{1}{c}\,\alpha_\nu F_\nu \mathrm{d}\nu = \frac{1}{c}\,\alpha_\nu \int I_\nu\, \mathbf{n}\cdot \mathrm{d}\Omega\, \mathrm{d}\nu \qquad (4.24)$$

where $F_\nu$ is the monochromatic flux and $\mathbf{n}$ is the direction of propagation

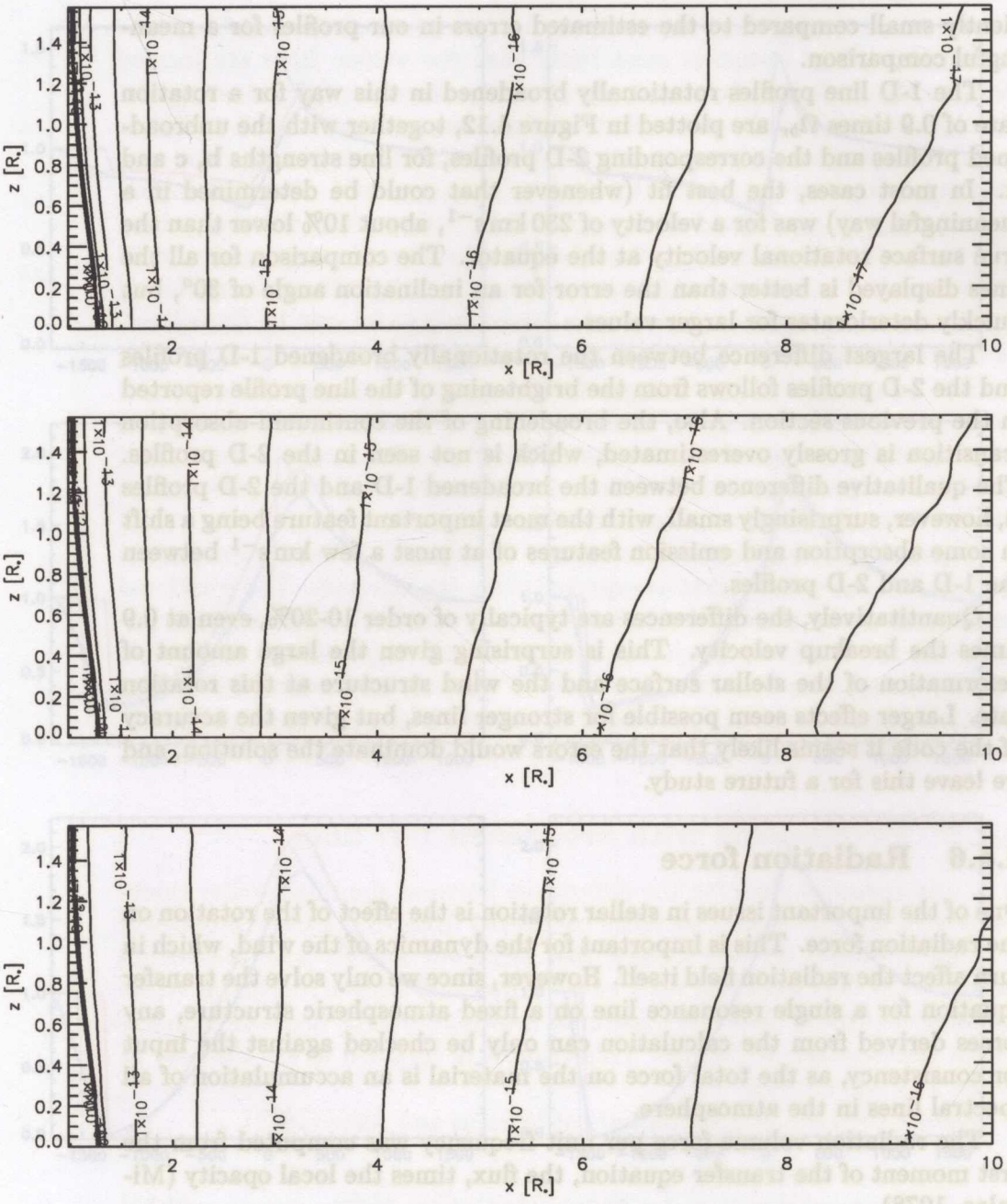


Figure 4.13: *Radiation force per unit volume* [$\mathrm{dyn\,cm^{-3}}$] *in the r direction, at a rotation rate of 0.9 times* $\Omega_{br}$ *and for line* **a** *(top),* **b** *(middle) and* **c** *(bottom).*

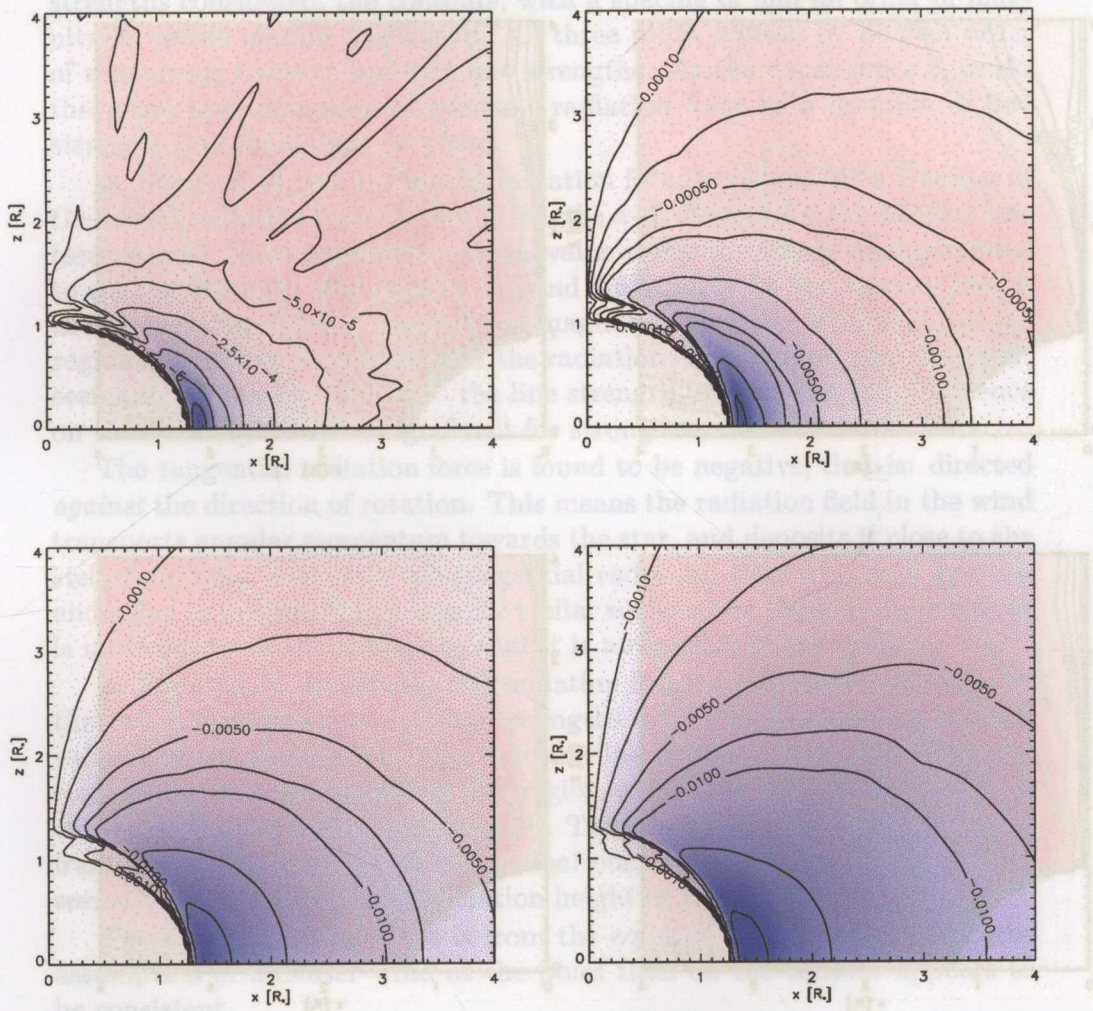


Figure 4.14: *Radiation force per unit volume in the $\varphi$ direction normalized to the radiation force per unit volume in the r direction, at a rotation rate of 0.9 times $\Omega_{br}$ and for line* **a** *(top left),* **b** *(top right),* **c** *(bottom left) and* **d** *(bottom right).*

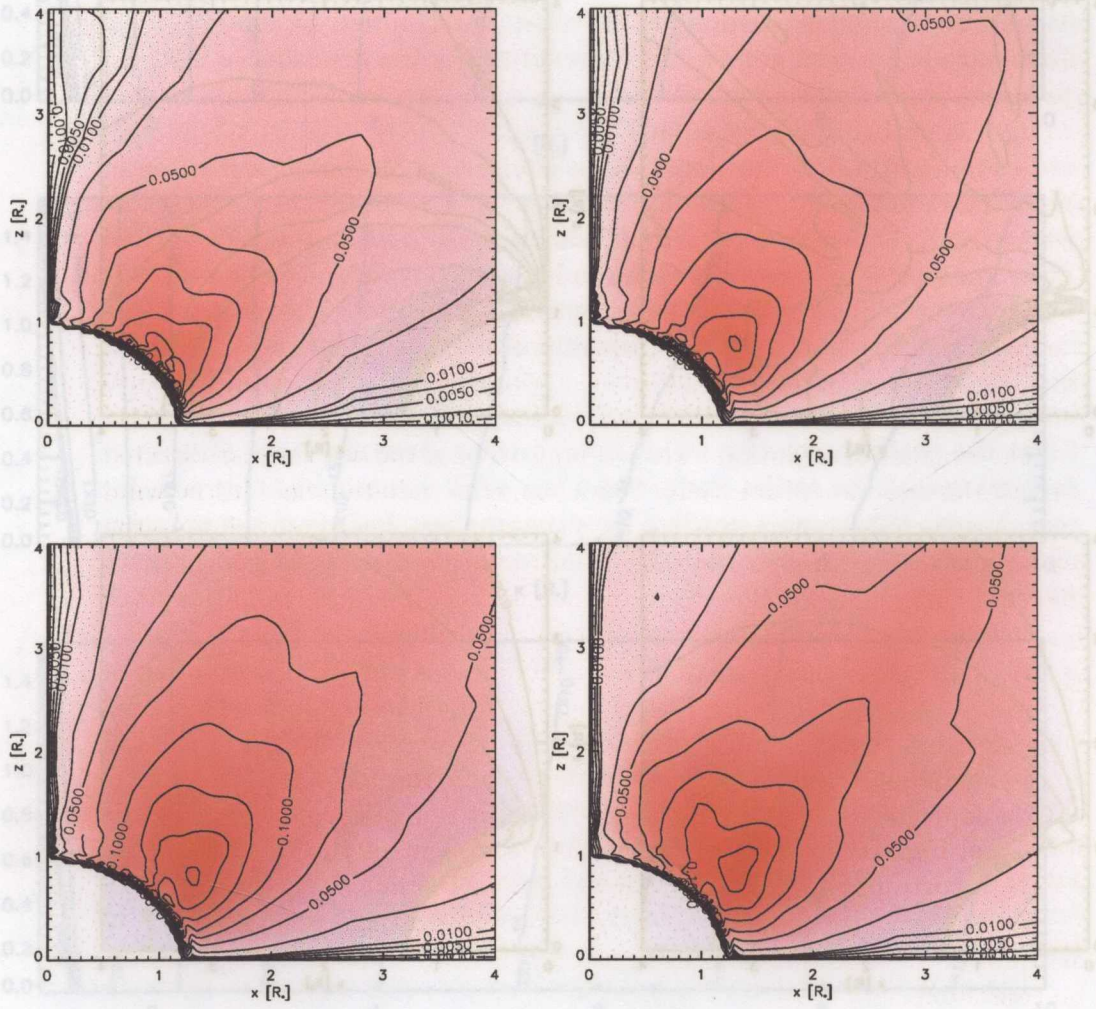


Figure 4.15: *Radiation force per unit volume in the $\theta$ direction normalized to the radiation force per unit volume in the r direction, at a rotation rate of 0.9 times $\Omega_{br}$ and for line* **a** *(top left),* **b** *(top right),* **c** *(bottom left) and* **d** *(bottom right).*

of the intensity $I_\nu$.

The radiation force, integrated across the frequency band affected by the line, is plotted in Figures 4.13-4.15 for 0.9 times the breakup rotation rate. The radial radiation force, plotted in Figure 4.13 for line strengths **a-c**, appears to increase roughly proportional to the square root of the line strength. For an increase of one order of magnitude between the line strengths considered, the contours, with a spacing of half an order of magnitude, are in similar positions in all three plots, shifted by half an order of magnitude between any two line strengths. As the dependence is weak, the usual approximation of constant radiation force as a function of line strength is probably not very bad.

In Figure 4.14, the tangential radiation force is plotted as a fraction of the radial radiation force for line strengths **a-d**. Except for the weakest line (strength **a**), the maximum fractional value seems to be only weakly related to the line strength, and peaks at around 5-6%. Only for the weakest line, is the importance at least one order of magnitude smaller. The extent of the region in which this component of the radiation force is important, however, seems to be directly related to the line strength, so that the total influence on the wind is still more significant for strong lines than for weak lines.

The tangential radiation force is found to be negative, that is: directed *against* the direction of rotation. This means the radiation field in the wind transports angular momentum towards the star, and deposits it close to the stellar surface. Although the tangential radiation force is indeed positive and equal in magnitude close to the stellar surface, the radial radiation force is much larger in this region, so that it is not visible in the plots.

In Figure 4.15, the latitudinal radiation force is plotted as a fraction of the radial radiation force for line strengths **a-d**. The maximum fractional value does not appear to be related to the line strength, as for the tangential component, but the extent of the region where the force is significant is clearly dependent on the line strength. The position of the maximum in the fractional importance of the latitudinal component of the radiation force seems to correspond to the formation height of the line.

The direction of the force is from the equator to the pole, so that the assumption of a denser wind at the poles than on the equator appears to be consistent.

The origin of the latitudinal and tangential components of the radiation force is clearly different, as is demonstrated by Figure 4.16-4.17.

Figure 4.16 shows the tangential radiation force for 4 different rotation rates, 0.5, 0.75, 0.85 and 0.9 times the breakup rotation rate, normalized to the radial radiation force. The maximum fractional value of the tangen-

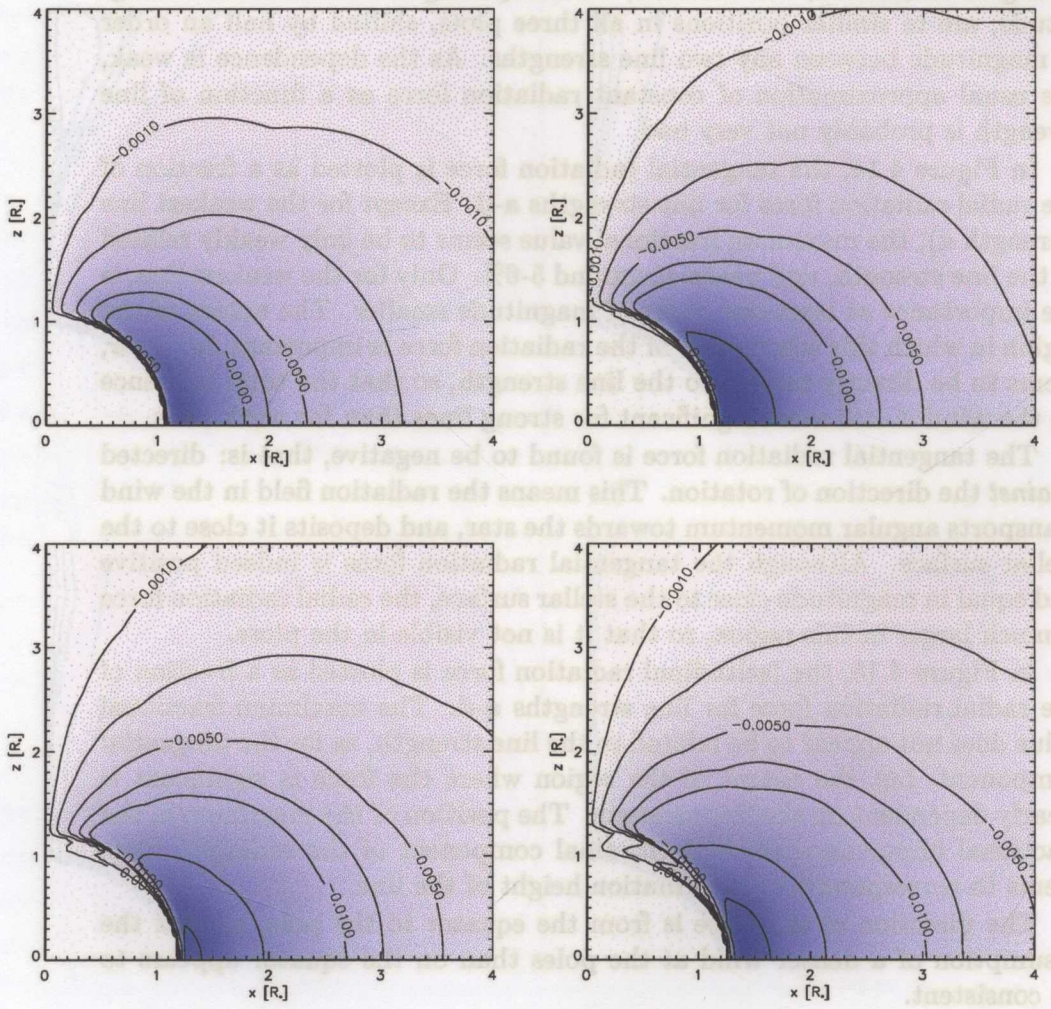


Figure 4.16: *Radiation force per unit volume in the $\varphi$ direction normalized to the radiation force per unit volume in the r direction, for line strength* **c** *and for a rotation rate of 0.5 (top left), 0.75 (top right) 0.85 (bottom left) and 0.9 (bottom right) times $\Omega_{br}$.*

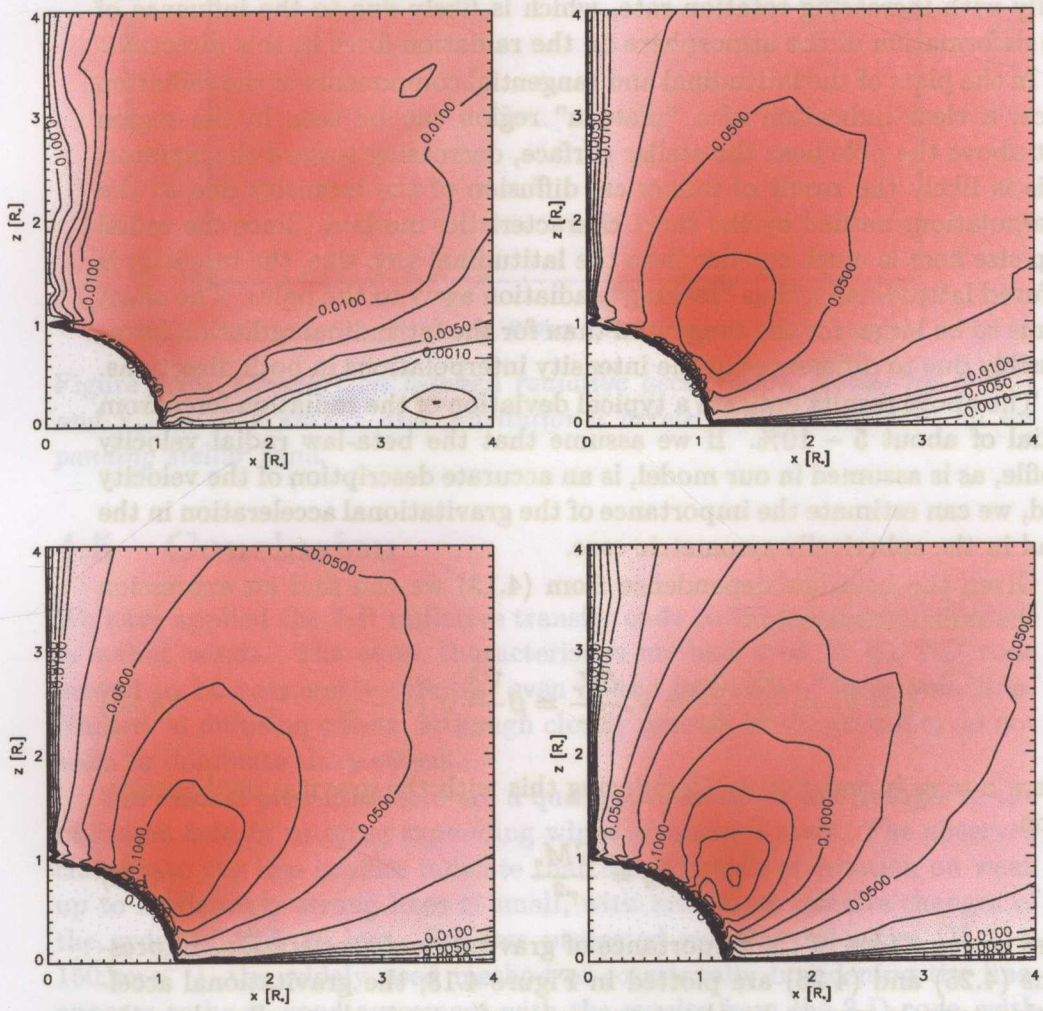


Figure 4.17: *Radiation force per unit volume in the $\theta$ direction normalized to the radiation force per unit volume in the r direction, for line strength* **c** *and for a rotation rate of 0.5 (top left), 0.75 (top right) 0.85 (bottom left) and 0.9 (bottom right) times $\Omega_{br}$.*

tial radiation force increases approximately linearly with increasing rotation rate, indicating that this component is mainly the result of a direct radiative transfer effect.

In Figure 4.16, the latitudinal radiation force for the same 4 rotation rates is plotted, again normalized to the radial radiation force. The maximum fractional value of the latitudinal radiation force increases quadratically with increasing rotation rate, which is likely due to the influence of the deformation of the atmosphere on the radiation force in this direction.

In the plots of the latitudinal and tangential components of the radiation force, a clear indication of a "plateau" region can be seen in the region just above the pole near the stellar surface, decreasing toward the equator. This is likely the result of numerical diffusion of the intensity due to the interpolations needed by the short characteristics method. Since the radial step size here is much smaller than the latitudinal step size, the intensity is diffused latitudinally, thus "leaking" radiation away to the poles. The effect seems to be larger for the tangential than for the latitudinal radiation force, possibly due to differences in the intensity interpolations in both directions.

The above results indicate a typical deviation of the radiation force from radial of about $5 - 10\%$. If we assume that the beta-law radial velocity profile, as is assumed in our model, is an accurate description of the velocity field, we can estimate the importance of the gravitational acceleration in the wind in the spherically symmetric case.

Given the beta-law dependence from (4.13) we can find an expression for the radial acceleration

$$\ddot{x} = \dot{V}_r = \frac{\partial V_r}{\partial r}\frac{\partial r}{\partial t} = V_r \frac{\partial V_r}{\partial r} = \beta \frac{V_\infty^2}{r_0} x^2 (1-x)^{2\beta-1}, \tag{4.25}$$

where $x = r_0/r$ and $\beta \approx 1$. Comparing this with the gravitational acceleration

$$g = \frac{GM_*}{r^2} \tag{4.26}$$

gives us some idea of the importance of gravitational acceleration. Expressions (4.25) and (4.26) are plotted in Figure 4.18; the gravitational acceleration term is seen to be about one order of magnitude smaller than the acceleration of the wind.

Since gravity is of only minor importance, the magnitude of the ratio of latitudinal to radial and tangential to radial radiation forces is indicative for the order of magnitude of the changes to the wind structure due to differential rotation.

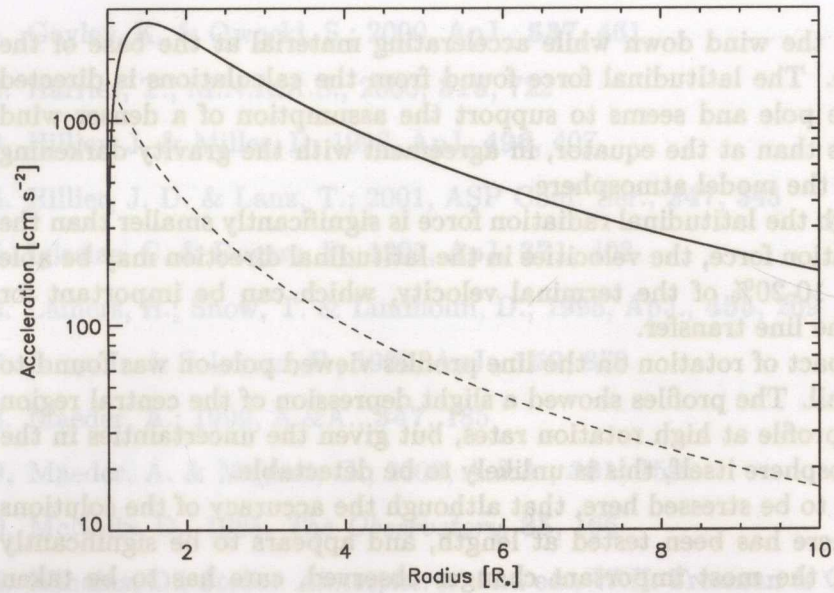


Figure 4.18: *Comparison between radiative acceleration (solid) for* $\beta = 1$ *and* $V_\infty = 1500\,km\,s^{-1}$ *and gravitational acceleration (dashed) in an expanding stellar wind.*

## 4.5 Conclusion

We have applied the 2-D radiative transfer code to the problem of rotation in stellar winds. The short characteristics method used in the 2-D code proved to be reasonably reliable, even in the presence of large velocities. Numerical diffusion effects, although clearly present in the solution, do not seem to dominate the problem.

The results presented here are a qualitative study of the changes in the radiation field in rotating expanding winds of massive stars. The observed changes to the line profiles indicate that the influence of rotation on weak up to moderately strong lines is small, with maximum relative changes of the order of 20% or less. For low projected rotation velocities ($V_{rot} < 150\,\mathrm{km\,s^{-1}}$), the widely used method of rotationally broadening the line, appears to be in good agreement with the results from the 2-D code, with most changes smaller than the typical error of the 2-D code ($\sim 5\%$). Only for the highest rotation rates and viewing the star equator-on are the changes in the line profiles significant.

The radiation force is affected at a similar level, with typical maximum departures from radial of 10-20%. There is a small tangential force, tend-

ing to slow the wind down while accelerating material at the base of the atmosphere. The latitudinal force found from the calculations is directed towards the pole and seems to support the assumption of a denser wind at the poles than at the equator, in agreement with the gravity darkening assumed in the model atmosphere.

Although the latitudinal radiation force is significantly smaller than the radial radiation force, the velocities in the latitudinal direction may be able to grow to 10-20% of the terminal velocity, which can be important for details in the line transfer.

The impact of rotation on the line profiles viewed pole-on was found to be very small. The profiles showed a slight depression of the central region of the line profile at high rotation rates, but given the uncertainties in the model atmosphere itself, this is unlikely to be detectable.

It needs to be stressed here, that although the accuracy of the solutions presented here has been tested at length, and appears to be significantly better than the most important changes observed, care has to be taken in interpreting these results. The reliability of the results is, as always, not better than the model atmosphere from which they are derived. For a complete treatment of the transfer problem in 2-D atmospheres, a significant increase in the level of detail of the atomic data is needed, which is at present beyond our numerical capabilities.

# References


1. Abbott, D.; 1978, ApJ., **225**, 893
2. Abbott, D.; 1982, ApJ., **259**, 282
3. Aufdenberg, J; 2001, P.A.S.P, **113**, 119
4. Bjorkman, J. & Cassinelli, J.; 1993, ApJ., **409**, 429
5. Bonnet, R. M.; 1983, Solar Physics, **82**, 487
6. Cassinelli, J.; 1991, Astr. Union Symp., **143**, 289
7. Castor, J.; Abbott, D. & Klein, R.; 1975, ApJ, **195**, 157
8. Cranmer, S. & Owocki, S.; 1995, ApJ., **440**, 308
9. Deubner, F. & Gough, D.; 1984, Ann. Rev. A. & A. , **22**, 593
10. Friend, D.B., Abbott, D.C.; ApJ, 1986, **311**, 701

11. Gayley, K. & Owocki, S.; 2000, ApJ., **537**, 461

12. Harries, T.; M.N.R.A.S., 2000, **315**, 722

13. Hillier, J. & Miller, D; 1998, ApJ, **496**, 407

14. Hillier, J. D. & Lanz, T.; 2001, ASP Conf. Ser., **247**, 343

15. Iglesias, C. & Rogers, F.; 1991, ApJ, **371**, 408

16. Lamers, H.; Snow, T. & Lindholm, D.; 1995, ApJ., **455**, 269

17. Lucy, L. & Solomon, P.; 1970, ApJ., **159**, 879

18. Maeder, A.; 1999, A.&A., **347**, 185

19. Maeder, A. & Meynet, G.; 2000, A.&A., **361**, 159

20. McNally, D., 1965, *The Observatory*, **85**, 166

21. Mihalas, D., *Stellar Atmospheres*, 2nd ed., W.H. Freeman & Co., San Francisco, 1978

22. Mihalas, D., Auer, L.; ApJ, 1970, **161**, 1129

23. Owocki, S. & Gayley, K.; 1997, ASP Conf. Ser., **120**, 121

24. Owocki, S. & Puls, J.; 2002, ApJ., **568**, 965

25. Owocki, S.; Cranmer, S. & Blondin, J.; 1994, ApJ., **424**, 887

26. Owocki, S.; Cranmer, S. & Gayley, K.; 1998, Ap.&S.Sc., **260**, 149

27. Paploizou, J. & Wheler, J.; 1973, M.N.R.A.S, **164**, 1

28. Pauldrach, A.; Puls, J.; Hummer, D.; Kudritzki, R. P.; 1985, A.&A. Lett., **148**, 1

29. Pauldrach, A.; Puls, J.; Kudritzki, R. P.; 1986, A.&A., **164**, 86

30. Petrentz, P. & Puls, J.; 2000, A.&A., **358**, 956

31. Press, W.H., Teukolsky, S.A., Vetterling, W.T., Flannery, B.P.; *Numerical Recipes in C*, 2nd ed., Cambridge University Press, New York, 1992

32. Tassoul, J.; *Stellar Rotation*, Cambridge University Press, New York, 2000

33. von Zeipel, H., 1924, MNRAS, **84**, 684

# Chapter 5

# NLTE Radiative Transfer in CV Disks.

**We apply the 2D Short Characteristics code, presented in chapter 2, to the problem of line transfer in accretion disks in cataclysmic variables. The aim is to calculate line profiles and radiation pressure to qualitatively investigate the effect of the radiation field on the disk structure. We observed significant NLTE effects only at very small inclination angles ($< 10°$), since the rotational broadening dominates all other effects at larger angles. The effect of the differential rotation on the NLTE effects was found to be as important as the NLTE effects themselves.**

## 5.1 Introduction

Since almost all objects in the universe acquire angular momentum during their formation (Catelan & Theuns, 1996a, 1996b), it is usually not possible for material to flow directly from one object to another. Instead the material will orbit the receiving object, until it can lose its angular momentum somehow. If the loss of angular momentum is gradual, a steady flow of material will slowly approach the receiving object, forming an accretion disk. The gradual loss of angular momentum usually occurs through a viscous process of some sort, due to which the material in the disk is heated.

Some well studied objects in which radiation from an accretion disk is important vary from Active Galactic Nuclei (AGN) (Robson, 1999), to disks in T-Tauri stars (Bertout, 1989), to accreting binary systems (Hilditch, 2001). In some cases, the disk contributes only partly to the emitted radiation, making direct interpretation of the observed spectrum difficult. To test our understanding of the physics of accretion disks, it is helpful to find objects for which the disk is the dominant source of the radiation emitted.

Although manifestly astrophysically important, calculating the radiation field in a disk structure is not a simple 1-D problem, unlike the case for stellar atmospheres, since the disk has two very different length scales in the radial and vertical directions. In addition there may be a wind driven by the disk or the central object, resulting in an extended atmosphere that needs a true 3-D treatment (Pereyra, Kallman & Blondin, 1997).

An approximate way to deal with this problem, is to approximate the disk as a geometrically thin object, i.e. the radial length scale is much larger than the vertical one, so that the transfer equation may be solved by a series of vertical 1-D solutions (Hubeny, 1994). The advantage of this approach is that the radiative transfer can be calculated with a great level of detail, so that the vertical structure of the disk can be accurately determined.

However, Wehrsche, Bascheck & Shaviv (1994) claim that for disks in cataclysmic variable stars (hereafter CV), this approximation is not valid and a multidimensional solution cannot be avoided. 3-D calculations of resonance lines in CV disks have been carried out (Adam, 1990; Papkalla, 1994), but the enormous numerical effort needed to solve the transfer equation in 3-D has precluded the inclusion of any level of detail beyond the 2-level atom formulation.

We apply the 2-D short characteristics radiative transfer code, presented in chapter 2 (van Noort, Hubeny & Lanz, 2002), to the problem of the line transfer of resonance lines in CV disks. The assumption of a 2-D cylindrical computational grid with rotational symmetry significantly reduces the nu-

merical effort, so that the line profile and rotational velocity can be treated accurately. Since we are currently only able to calculate a radiative transfer solution on a specified density, temperature and velocity structure, we calculate a 2-D disk structure from a series of 1-D solutions (Wade & Hubeny, 1998).

Although for detailed calculations of the emergent spectrum, the simultaneous self-consistent calculation of the disk structure and the radiation field are needed, which is beyond our current capabilities, the current study should give us insight in what differences to expect from such calculations with respect to the currently used 1-D approach. The emphasis will be on the diagnostic value of a multidimensional as opposed to a 1-D treatment of the radiation field, as well as on the radiation forces that are likely to be important in the dynamics of the disk.

## 5.2 Cataclysmic Variables

Cataclysmic variables (CV's) are a class of objects that is characterised by their very large variability of up to 6 orders of magnitude and the very short timescale on which they can vary.

Observations of them have been reported for over a century, and models of them have been developed based on their characteristics. The very short timescale of their variability suggests a very compact object of at most a few AU, the temperature of their spectra, however, is typically between $10^4$ and $10^5$ K (Warner, 1995).

Since fusion-based explanations cannot produce the energy radiated away from such a small region, these objects can only be associated with accretion flows onto compact objects, such as white dwarfs or neutron stars. The kinetic energy, acquired by falling into the gravitational well of the compact object, is able to account for the observed luminosity and temperatures.

The binary nature of CV's was first suggested by Kraft (1962), who noted that all the CV systems he observed were spectroscopic binaries that consisted of a white dwarf primary and an approximately $1M_{\odot}$ secondary star. He suggested a model whereby the primary star accreted material from the secondary.

This model was developed further by Shakura & Sunyaev (1973), who calculated the structure of the disk, asuming a simple parameterisation of the disk viscosity. Although many people have refined their original model, the exact physical nature of the disk viscosity remains a topic of debate. The disk geometry, however, was verified by Horne (1985) and Marshe &

Horne (1988), who were able to map the intensity distribution of the disk for some eclipsing CV binaries.

The evolution of a CV consists of a complex sequence of events (see also Patterson 1984). The initial state of the binary is that of a low mass dwarf, typically 0.1-0.2 $M_\odot$, orbiting a more massive primary with a long period. The primary evolves past the red giant stage and ejects a planetary nebula, causing the secondary component to spiral in, the common envelope phase. The primary then evolves further into a white dwarf. The magnetized wind of the secondary slowly reduces the orbital separation (Patterson 1984), until the low-mass secondary fills its Roche lobe and starts to transfer mass to the primary, by which time the binary system that is left has a period of only a few hours and a separation $\sim 1\,R_\odot$. The mass transfer from the secondary to the primary results in an accretion disk (Patterson 1984) in non-magnetically dominated systems, or an accretion column in the magnetically dominated case.

As the spiral-in phase takes a long time, the white dwarf is generally already quite cool by the time the accretion phase starts. The system now consists of two low luminosity components, so that the luminosity of the system is easily dominated by the radiation emitted by the disk. CVs therefore provide a good test case for our understanding of plasma physics and accretion processes in general. For this reason, they have been extensively studied, revealing many subclasses of magnetic and non-magnetic CVs, depending on the accretion rate and the properties of the primary (an extensive survey of many properties and subtypes of CVs is given by Warner, 1995).

In magnetically dominated systems, the dynamics of material is partially or completely determined by the magnetic field of the white dwarf. The resulting changes in the density, temperature and velocity structure with respect to the non-magnetically dominated case can vary from truncation of the inner part of the disk for relatively weak magnetic fields to complicated, 3-D structures for strong magnetic fields. Here we will be concerned only with non-magnetically dominated systems. These can be roughly subdivided in two categories.

In nova systems, the accretion rate is constant over long periods of time (years to decades), while mass accumulates on the surface of the white dwarf. When the pressure and temperature are sufficient to start nuclear fusion, a nuclear runaway in the envelope triggers an explosion, the nova, which can increase the luminosity by some 2-6 orders of magnitude. The disk is completely disrupted and has to re-form, after which the normal accretion state is resumed. As the period between outbursts is long, and the

luminosity of the system can be dominated by the disk luminosity during these periods, these are the most interesting systems for studying steady state disks.

Sub-nova or dwarf nova systems are less extreme, with the outbursts being related to periods of increased accretion rather than thermonuclear runaway, and the variation of the luminosity is consequently less spectacular. The occurrence of sub-novae is, however, much more frequent (days or weeks), and during the outbursts several interesting phenomena have been observed, related to the configuration and dynamics of the accretion disk. These are therefore interesting systems for studying the time dependent behavior of the disk.

The variability of CVs seems to be an essential part of their behavior, and during outbursts variability on many time scales has been observed. Some of these are associated with inhomogeneities in the disk (clumping), and instabilities in the dynamics of the disk (i.e. superhumps, etc., see Warner 1995), indicating that these disks are not always homogeneous and cylindrically symmetric.

In addition, P-Cygni profiles have been observed coming from CV systems, suggesting there is a substantial wind coming from the disk (Heap et. al 1978, Greenstein & Oke 1982, Córdova & Mason 1982) with a terminal velocity corresponding to the escape velocity of the white dwarf. The formation of the emission lines is not yet fully understood and requires detailed, self-consistent modelling of the entire system.

For simplicity, however, we will concentrate on a time averaged disk structure of a nova system only, which is assumed to be in a steady state, cylindrically symmetric, non-magnetically dominated, have a constant accretion rate and does not have a wind.

### 5.2.1 CV disk structure

Although the vertical structure of a disk is usually very important from an observational and diagnostic point of view, if the vertical height of the disk is much less than the inner radius of the disk, the radial structure can be conveniently derived by vertically integrating the density. The density of the disk can then be expressed as a surface density, $\rho$, so that the continuity equation, expressing conservation of mass, becomes

$$\frac{\partial \rho}{\partial t} + \vec{\nabla} \cdot (\rho \mathbf{v}) = \frac{\partial \rho}{\partial t} + \frac{1}{r}\frac{\partial}{\partial r} r (\rho v_r) = 0 \qquad (5.1)$$

in polar coordinates, assuming cylindrical symmetry.

Similarly we can write the conservation of angular momentum, $\mathbf{l} = \mathbf{r} \times (\rho \mathbf{v})$, as

$$\frac{\partial \mathbf{l}}{\partial t} + \vec{\nabla} \cdot (\mathbf{l} \otimes \mathbf{v}) = \left( \frac{\partial \rho r^2 \Omega}{\partial t} + \frac{1}{r} \frac{\partial}{\partial r} r \left( \rho r^2 \Omega v_r \right) \right) \hat{\mathbf{z}} = Q \, \hat{\mathbf{z}} \tag{5.2}$$

where $\hat{\mathbf{z}}$ is the unit vector in the $z$-direction and $Q$ is a viscous torque term (Frank, King & Raine, 2002)

$$Q = \frac{1}{r} \frac{\partial}{\partial r} \nu \rho r^3 \frac{\partial \Omega}{\partial r} \tag{5.3}$$

The time independent simultaneous solution of (5.1)-(5.3) can be found by setting $\partial / \partial t = 0$, so that (5.2) becomes

$$r \left( \rho r^2 \Omega v_r \right) = \nu \rho r^3 \frac{\partial \Omega}{\partial r} + C. \tag{5.4}$$

The value of C can be found by assuming that the Keplerian velocity at $R_*$ is greater than the rotation velocity of the star, and that the boundary layer at which the velocity departs from Keplerian is thin compared to $R_*$. We can then assume that there is a point where

$$\frac{\partial \Omega}{\partial r} \Big|_{r=R_*} = 0 \quad \text{and} \quad \Omega \approx \Omega_K(R_*) \tag{5.5}$$

so that

$$C = -\frac{\dot{m}}{2\pi} \sqrt{GMR_*}. \tag{5.6}$$

with $\dot{m} = -2\pi r \rho v_r$ is the accretion rate. Substitution of a Keplerian value for $\Omega$ in (5.4) gives

$$\rho = \frac{\dot{m}}{3\pi\nu} + \frac{2C}{3\nu\sqrt{GMr}} = \frac{\dot{m}}{3\pi\nu} \left( 1 - \sqrt{\frac{R_*}{r}} \right) \tag{5.7}$$

All we need now is a description for the disk viscosity, $\nu$, to derive the vertically integrated mass density for a thin disk. A famous parameterization, by Shakura & Sunyaev (1973), is the $\alpha$-parameterization

$$\nu = \alpha c_s H \tag{5.8}$$

where $c_s$ is the local sound speed and $H$ the height of the disk. Assuming a simple parameterization for the opacity, the structure of the Shakura-Sunyaev solution to the disk problem can be analytically determined.

Another approach (Lynden-Bell & Pringle, 1974) is to regard the viscosity as resulting from turbulence of some sort. Given the molecular viscosity, the value of the Reynolds number for typical disks assuming molecular viscosity only is

$$Re = \frac{\Omega R^2}{\nu_{mol}} >> Re_c \approx 10^3, \tag{5.9}$$

where $Re_c$ is the critical Reynolds number beyond which the flow will become turbulent. The critical value of around $10^3$ is found from experience with laboratory fluid dynamics.

We can thus safely assume that the disk is turbulent and that the turbulent viscosity dominates all other sources of viscosity. If we assume that the turbulence can somehow gain energy from the shear in the disk flow, it will grow until the turbulent viscosity is large enough for the viscous energy dissipation to balance the energy input. This is exactly the case for the critical Reynolds number, $Re_c$, so that the viscosity can be found from

$$\nu_c \approx \frac{\Omega R^2}{Re_c} \tag{5.10}$$

Although given the viscosity the radial structure of the disk is known, the vertical structure still needs to be calculated. This cannot be done in a similar way to calculating a stellar atmosphere for two important reasons. Firstly the optical thickness of the disk is not infinite, and secondly energy is generated *inside* the disk structure, whereas in the stellar case it is only *flowing through* the atmosphere.

The result is that, since energy is released throughout the disk structure, the surface layers of the disk are heated and a hot corona and an outflow are formed. The dynamics and structure of the wind are an active field of research, and much progress has recently been made. Pereyra, Kallman & Blondin (1997) and more recently Perreyra & Kallman (2003) made time-dependent models of CV disk structures and their winds and concluded that there was a supersonic outflow from the central regions of the disk colliding with the wind from the disk, producing a shock front above the disk.

However, line profiles calculated from these structures are currently not able to reproduce observed line profiles (Proga, Kallman, Drew & Hartley 2002). Clearly, the structure is multidimensional and to model it a detailed multidimensional treatment of the radiation transfer is needed. This is presently not possible due to limitations in numerical resources, so that alternative methods are employed here.

We will adopt the commonly made approximation for disks, that the radial optical thickness of the disk is much larger than the vertical one and

that there is no wind. The disk can then simply be approximated by a series of 1-D solutions, each of which can be calculated in great detail.

For simplicity we neglect the boundary layer, connecting the disk to the star. This is not necessarily appropriate, as about half of all the gravitational potential energy of the material originally falling into the disk is converted to kinetic energy at the inner boundary and a substantial portion of this energy is radiated away in the boundary layer. Due to the large difference in the disk temperature and the temperature of the boundary layer, the two contributions can usually be separated easily, so that we do not consider its contribution here, but we concentrate on the disk itself instead.

## 5.3 CV Disk model atmospheres

For the present calculations, CV disk models were taken from the grid of models calculated by Wade & Hubeny (1998), computed with the program TLUSDISK (Hubeny, 1990).

In these models, the radial density structure was calculated from (5.7) and (5.10), assuming a critical Reynolds number of 5000, and an effective temperature distribution, constraining the total flux at the surface, from Pringle (1981)

$$T_{eff}(r) = T_* x^{-\frac{3}{4}} \left(1 - x^{-\frac{1}{2}}\right)^{\frac{1}{4}} \tag{5.11}$$

where $x = r/R_*$ and

$$T_* = 64800\,K \times \left[\left(\frac{M_*}{1\,\mathrm{M}_\odot}\right)\left(\frac{\dot{m}}{10^{-9}\,\mathrm{M}_\odot\,\mathrm{y}^{-1}}\right)\left(\frac{R_*}{10^9\,\mathrm{cm}}\right)\right]. \tag{5.12}$$

On a number of "rings", sufficient to resolve the radial variations accurately, the vertical density and temperature structure was calculated by solving the hydrostatic equilibrium equations in a 1-D plane-parallel geometry, assuming LTE. Energy balance was enforced between the radiative losses at the surface and the viscous heating, distributed throughout the vertical extent of the disk.

The irradiation by the central star was not included in the model structure, which is a reasonable approximation for the structure, as the energy released inside the disk is much larger, provided the central star is not very hot. There may, however, be a significant irradiation effect of the radiation of the central star on the source function at the surface of the disk, so that for calculating the source function it is included.

The 2-D structure was compiled from a series of 1-D solutions provided by the TLUSDISK program. Since the points in the z-direction are different for all models, they need to be interpolated to a rectangular grid. Also, structural quantities are needed in regions where they are not provided.

To represent a disk of this type on a rectangular grid is not as easy as it may seem, as all vertical structures for all radii considered must be *simultaneously* resolved accurately by the vertical grid. Moreover, the part of the atmosphere where the resolution is most crucial, the photosphere, is not in the same vertical location for all radii. Although most vertical structures require a minimum of about 50 points, we have no more than about 100 vertical points to resolve the vertical structure for all radii simultaneously, so that sacrifices have to be made regarding the resolution.

The outer boundary of the disk cannot be taken from the 1-D structures, as an infinitely extended atmosphere was assumed in the $r$ and $\varphi$ directions to calculate them. This is obviously not true near the outer edge of the disk, and some solution for the structure needs to be found here. Since there are no good descriptions for this, a simple solution was employed, by rotating the vertical structure of the outermost ring with radius $R$ around the point $(R, 0)$, thus creating the outer half of a torus with a radial structure equal to the vertical structure of the outermost ring (Hubeny & Plavec, 1991). Although this method has no firm theoretical basis, it should be approximately correct and the contribution of this part of the disk to the emitted radiation is usually small and will thus not severely affect the results.

Since, on the grid, we are dealing with the disk only, irradiation of the disk by the central star and boundary layer need to be included by applying the appropriate boundary conditions. Since the star and the boundary layer extend above the disk, this needs to be done on two sides of the computational grid: the inner and the top boundaries. Although the temperature of the boundary layer is not known, for simplicity, we assume the incoming intensity at the boundaries to be equal to the Planck function, with a $T_{\rm eff} = 10^6$ K. The precise temperature is not very important, as the irradiation of the disk was found to be unimportant in all the cases presented here.

The line and continuum opacities were calculated as in §4.3.1, although the level populations should be calculated from first principles for more accurate results.

Finally, the rotational velocity was assumed to be Keplerian

$$v_\phi(r) = \sqrt{\frac{GM_{wd}}{r}} \tag{5.13}$$

and, for simplicity, a representative radial velocity of $10\,\mathrm{km\,s^{-1}}$ was assumed.

## 5.4 Results

We calculated the 2-D structures for Wade & Hubeny (1998) models **p** and **m**. Although they are LTE models, line transfer can be done in NLTE on these structures, providing some insight in the NLTE line formation in these systems and the importance of NLTE effects for the emergent line profiles.

Since the turbulent velocities underlying the disk viscosity and the mechanisms generating them have still not been clearly identified, we considered a constant turbulent velocity of $100\,\mathrm{km\,s^{-1}}$.

We considered three line strengths, **a** and **b**, with lower level population of $10^{-6}$ and $10^{-4}$ times the total ion number density respectively. These correspond to continuum to line opacity ratio, $r_{cl}$, of approximately $5 \cdot 10^4$ and $5 \cdot 10^6$ respectively, which corresponds to the strongest lines, such as H $L_\alpha$ and the C-IV resonance lines at 1550 Å.

The calculations were carried out on 50 2 GHz PCs, taking about 10 hours (15 minutes per ALI for approximately 40 iterations) to convergence. We used a cylindrical grid with $N_z \times N_r = 80 \times 96$ spatial points and $N_\theta \times N_\varphi = 13 \times 40$ angular points, distributed homogeneously over the $4\pi$ solid angle. The stopping criterium is set to be a maximum relative change of any quantity anywhere on the grid less than $10^{-3}$ between two consecutive ALI.

### 5.4.1 Model p

As a first choice, we selected model **p**, in the middle of the parameter space of the grid of model atmospheres calculated by Wade & Hubeny (1998). The mass of the white dwarf and the accretion rate are typical for those found in CV systems, about $0.8\,\mathrm{M_\odot}$ and $3.1 \cdot 10^{-10}\,\mathrm{M_\odot\,y^{-1}}$ respectively. The continuum optical thickness of the central part of the disk is $\sim 40$, and the radial optical thickness $\sim 2000$.

We only considered line strength **b**, as the NLTE effects for weaker lines were expected to be qualitatively similar and not very large.

#### 5.4.1.1 Line formation

For calculating the emergent line profile, the code presented in Chapter 3 was used. Due to the geometry of the structure, the distribution of the

points in each image was concentrated in rings, so that many points are

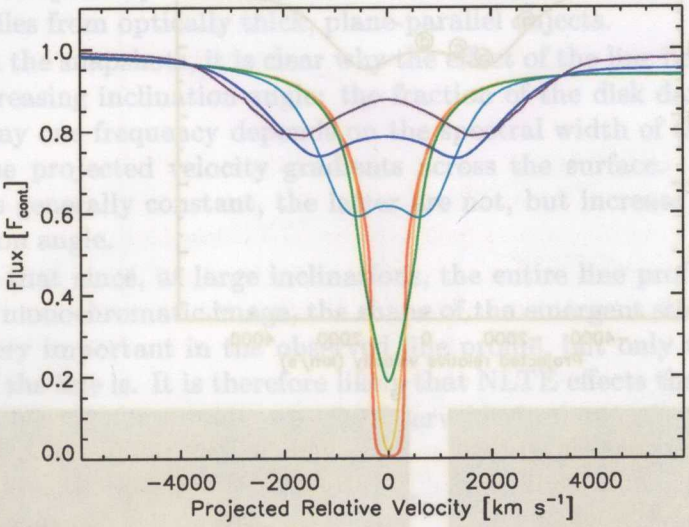


Figure 5.1: *Line profiles for model* **p**, *with* $V_{turb} = 100\,km\,s^{-1}$, *for* 0°, 5°, 10°, 30°, 60° *and* 80° *inclination. The change in the slope of the continuum with inclination angle is the result of limb darkening.*

needed to obtain an accurate answer. On average, to obtain an accuracy of around 0.01, 10000-20000 points per monochromatic image were needed.

To accurately take the obscuration of the disk by the star into account, the primary star was replaced with a non-radiating, absorbing sphere. Although for large inclination angles, the contribution of the star may, become important, this is not taken into account in the line profiles.

For a large range of inclination angles ($\gtrsim$10°), the formation of the line is completely dominated by the effect of the rotation. The projected rotation velocity is large enough to produce a characteristic double peaked line profile, as can be seen in Figure 5.1.

The monochromatic snapshots provided by the code, can provide some insight in the formation of this line profile. In Figure 5.2, monochromatic snapshots are plotted for several frequencies around the central frequency of a spectral line with strength **b** for disk model **p**.

Apart from the obvious bright central part of the disk, dark bands can be seen, the position and shape of which clearly depend on the frequency. The dark bands are regions of the disk where the rotational velocity, projected onto the line of sight, is such that we see the disk locally at or close to the line frequency $\nu_0$, i.e. $v_{proj} = c\,(\nu - \nu_0)/\nu_0$. The increased opacity,

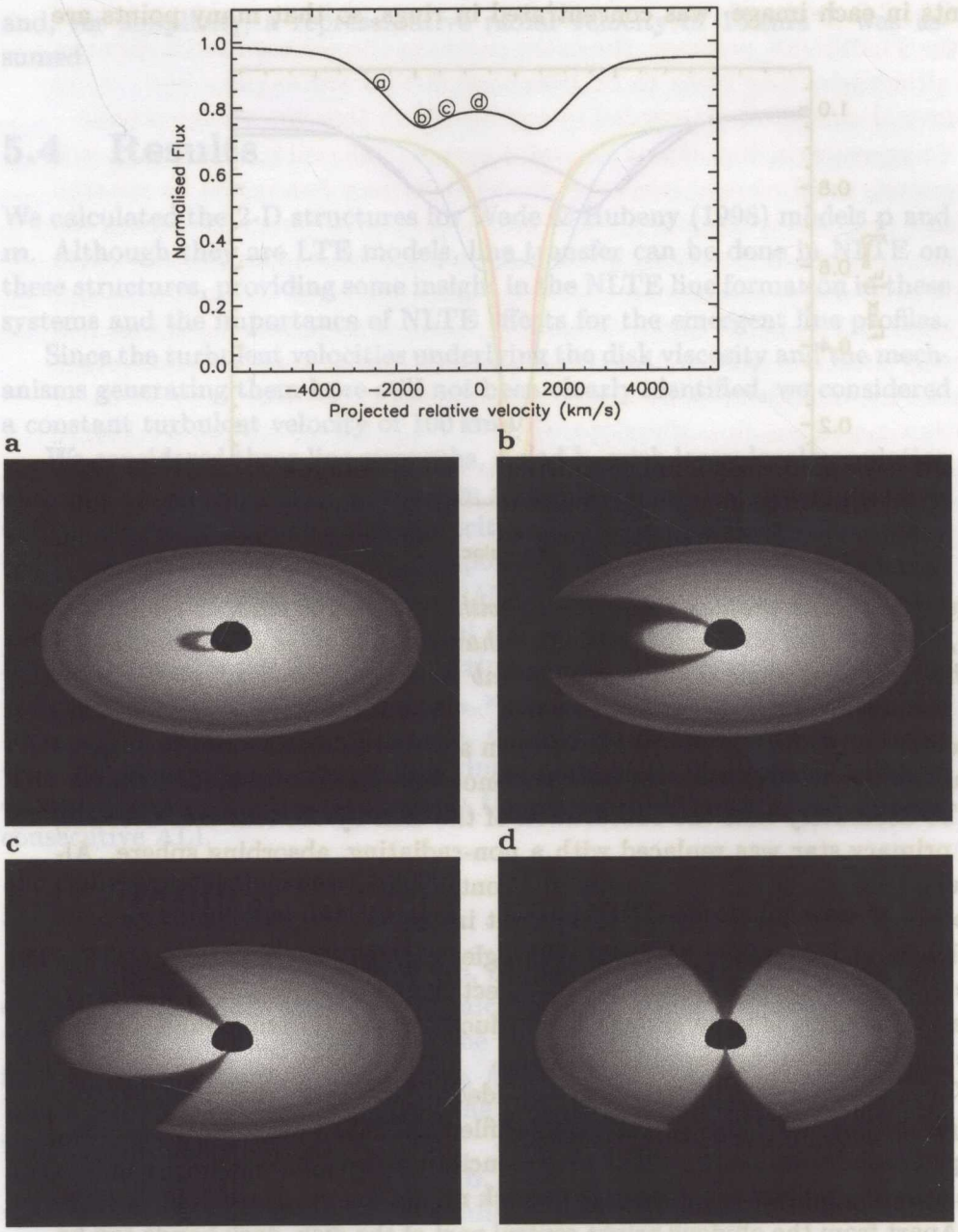


Figure 5.2: *Monochromatic snapshots of model* **p**, *in a spectral line (top), with* $V_{turb} = 100\,km\,s^{-1}$, *at* 60° *inclination. The logarithm of the normalized monochromatic intensity is plotted as a gray scale. The 'rings' visible on the surface are partly the result of inaccuracies in the solution due to the limited radial resolution.*

combined with the decreasing source function with decreasing optical depth in the atmosphere, produces the usual darkening, as we are used to in most line profiles from optically thick, plane-parallel objects.

From the snapshots, it is clear why the effect of the line becomes weaker with increasing inclination angle: the fraction of the disk darkened by the line at any one frequency depends on the spectral width of the line as well as on the projected velocity gradients across the surface. Although the former is generally constant, the latter are not, but increase strongly with inclination angle.

Note that since, at large inclinations, the entire line profile is included in every monochromatic image, the shape of the emergent static line profile is not very important in the observed line profile, but only the equivalent width of the line is. It is therefore likely that NLTE effects that do not alter the strength of a line much are only observable for low inclination systems.

#### 5.4.1.2 Effect of differential rotation

In Figure 5.3, the emergent line profiles are plotted for line strength **b** at 0° and 5° inclination for the same disk structure, but assuming LTE, NLTE without differential rotation and NLTE including differential rotation, when calculating the source function. In the line profile synthesis the rotation is fully taken into account in all three cases.

The effect of differential rotation on the source function is seen to be quite large, with the core flux of the line increasing by 50% at 0° inclination with respect to a NLTE treatment without differential rotation. However, already at 5° inclination, the effect of differential rotation on the line profile has all but disappeared.

The radiation forces are plotted in Figure 5.4. The dominant force is clearly in the $z$ direction, dominating the radial force by some 2 orders of magnitude. This seems to be consistent with a semi 1-D approach. The tangential radiation force is much smaller than the other forces and can be assumed completely unimportant, at 4 to 5 orders of magnitude below the radiation force in the $z$ direction.

Apart from a brightening of the inner core of strong resonance lines, no evidence was found for strong multidimensional effects or strong effects of differential rotation on the disk structure, probably due to the lack of important NLTE effects in the atmosphere. The importance of the differential rotation for the NLTE effects that were found indicates that a multidimensional treatment of the radiation field may be very important for disks with extended outflows, where NLTE effects can be expected to be much more

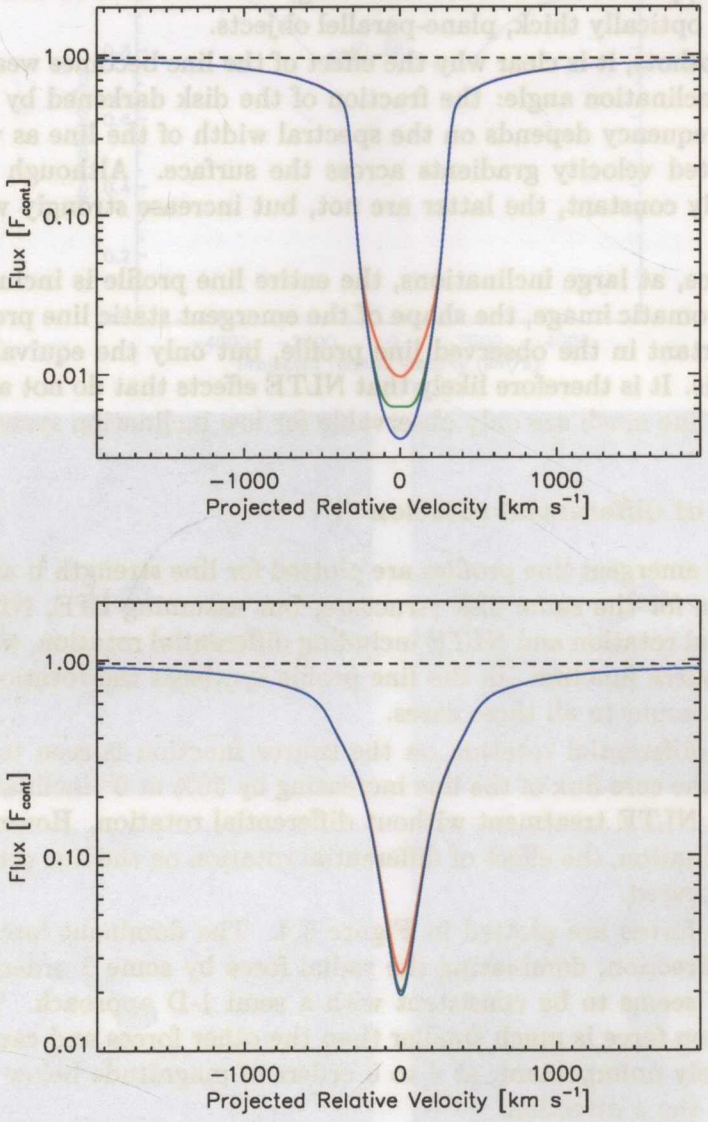


Figure 5.3: *Line profiles for model* **p**, *line strength* **b**, *for* 0° *(top) and and* 5° *(bottom) inclination for a source function calculated in* ***LTE***, ***NLTE without differential rotation*** *and* ***NLTE including differential rotation***. *The rotation is taken into account in all line profile calculations. The influence of NLTE effects is decreasing strongly with inclination angle and the influence of rotation deceases even faster.*

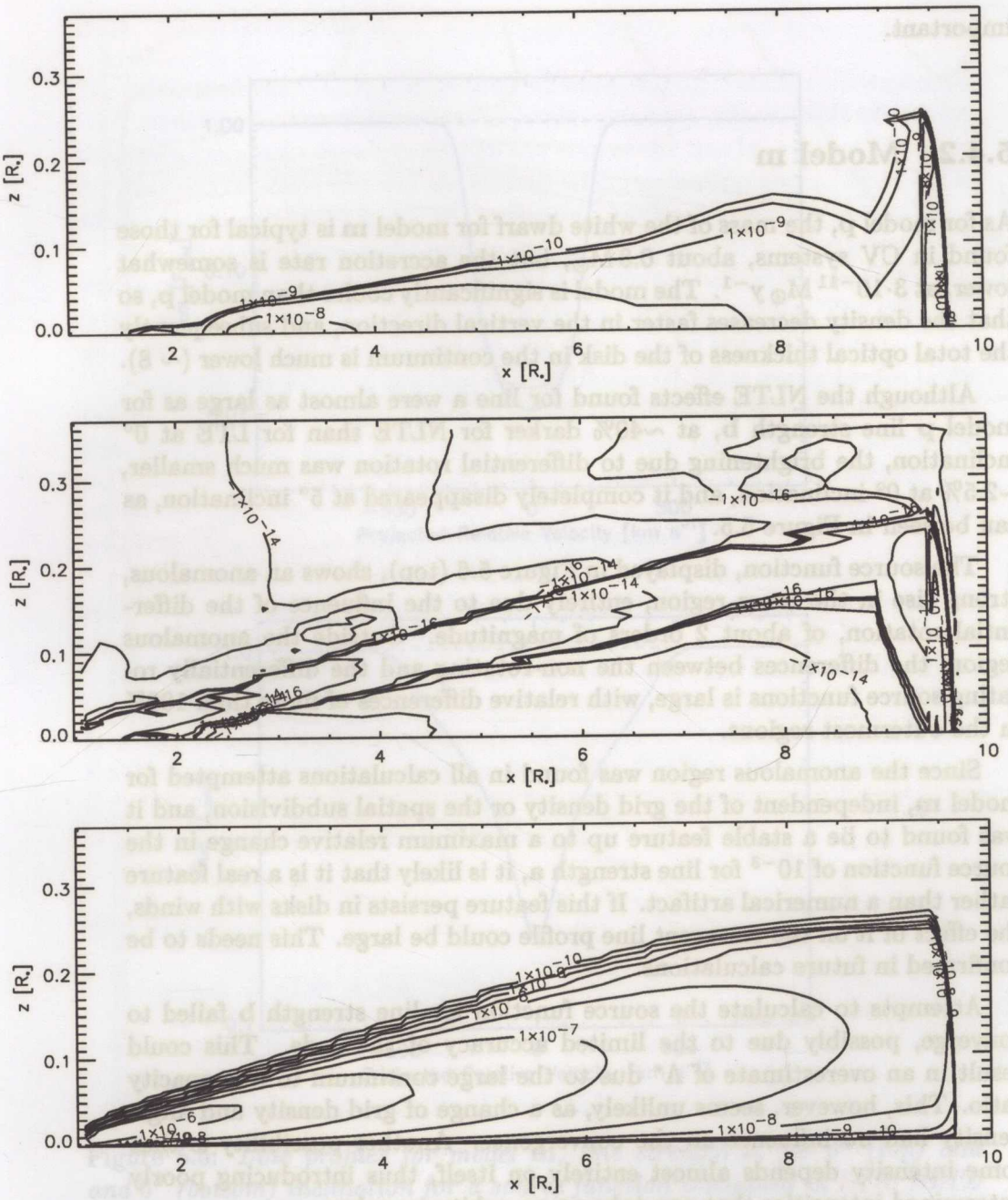


Figure 5.4: *Radiation force per unit volume* [dyn cm$^{-3}$] *in the r (top),* $\varphi$ *(middle) and in the z (bottom) direction for model* **p**.

important.

### 5.4.2 Model m

As for model **p**, the mass of the white dwarf for model **m** is typical for those found in CV systems, about $0.8\,M_\odot$, but the accretion rate is somewhat lower, at $3{\cdot}10^{-11}\,M_\odot\,y^{-1}$. The model is significantly cooler than model **p**, so that the density decreases faster in the vertical direction, and subsequently the total optical thickness of the disk in the continuum is much lower ($\sim 8$).

Although the NLTE effects found for line **a** were almost as large as for model **p** line strength **b**, at ~40% darker for NLTE than for LTE at 0° inclination, the brightening due to differential rotation was much smaller, ~2.5% at 0° inclination, and it completely disappeared at 5° inclination, as can be seen in Figure 5.5.

The source function, displayed in Figure 5.6 (top), shows an anomalous, strong rise in the inner region, entirely due to the influence of the differential rotation, of about 2 orders of magnitude. Outside the anomalous region, the differences between the non-rotating and the differentially rotating source functions is large, with relative differences of more than 100% in the outermost regions.

Since the anomalous region was found in all calculations attempted for model **m**, independent of the grid density or the spatial subdivision, and it was found to be a stable feature up to a maximum relative change in the source function of $10^{-3}$ for line strength **a**, it is likely that it is a real feature rather than a numerical artifact. If this feature persists in disks with winds, the effect of it on the emergent line profile could be large. This needs to be confirmed in future calculations.

Attempts to calculate the source function for line strength **b** failed to converge, possibly due to the limited accuracy of the code. This could result in an overestimate of $\Lambda^*$ due to the large continuum to line opacity ratio. This, however, seems unlikely, as a change of grid density and angle density had no influence on the convergence. Another possibility is that some intensity depends almost entirely on itself, thus introducing poorly determined intensities that can take on an arbitrary value.

In both cases, an substantial outflow eminating from the surface of the disk would probably eliminate the problem by increasing the opacity in the anomalous region, hence making it easier to converge the source function.

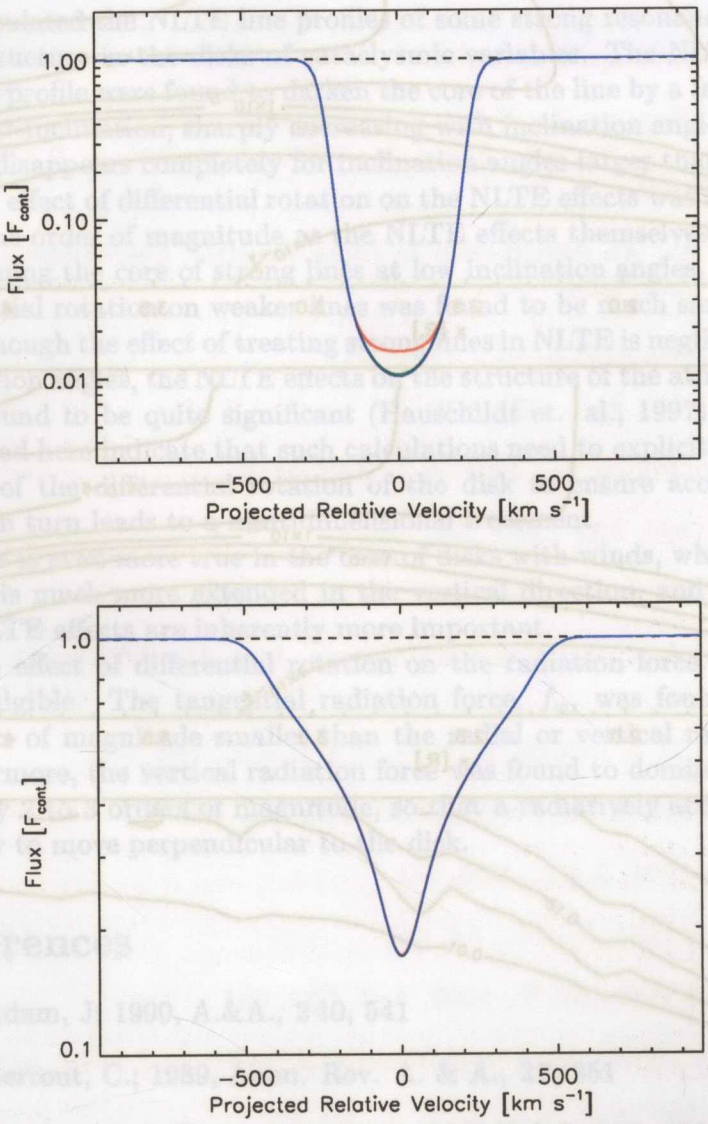


Figure 5.5: *Line profiles for model* **m**, *line strength* **a**, *for* 0° *(top) and and* 5° *(bottom) inclination for a source function calculated in* ***LTE***, ***NLTE without differential rotation*** *and* *NLTE including differential rotation*. *The rotation is taken into account in all line profile calculations. As for model* **p**, *the influence of NLTE effects is decreasing strongly with inclination angle.*

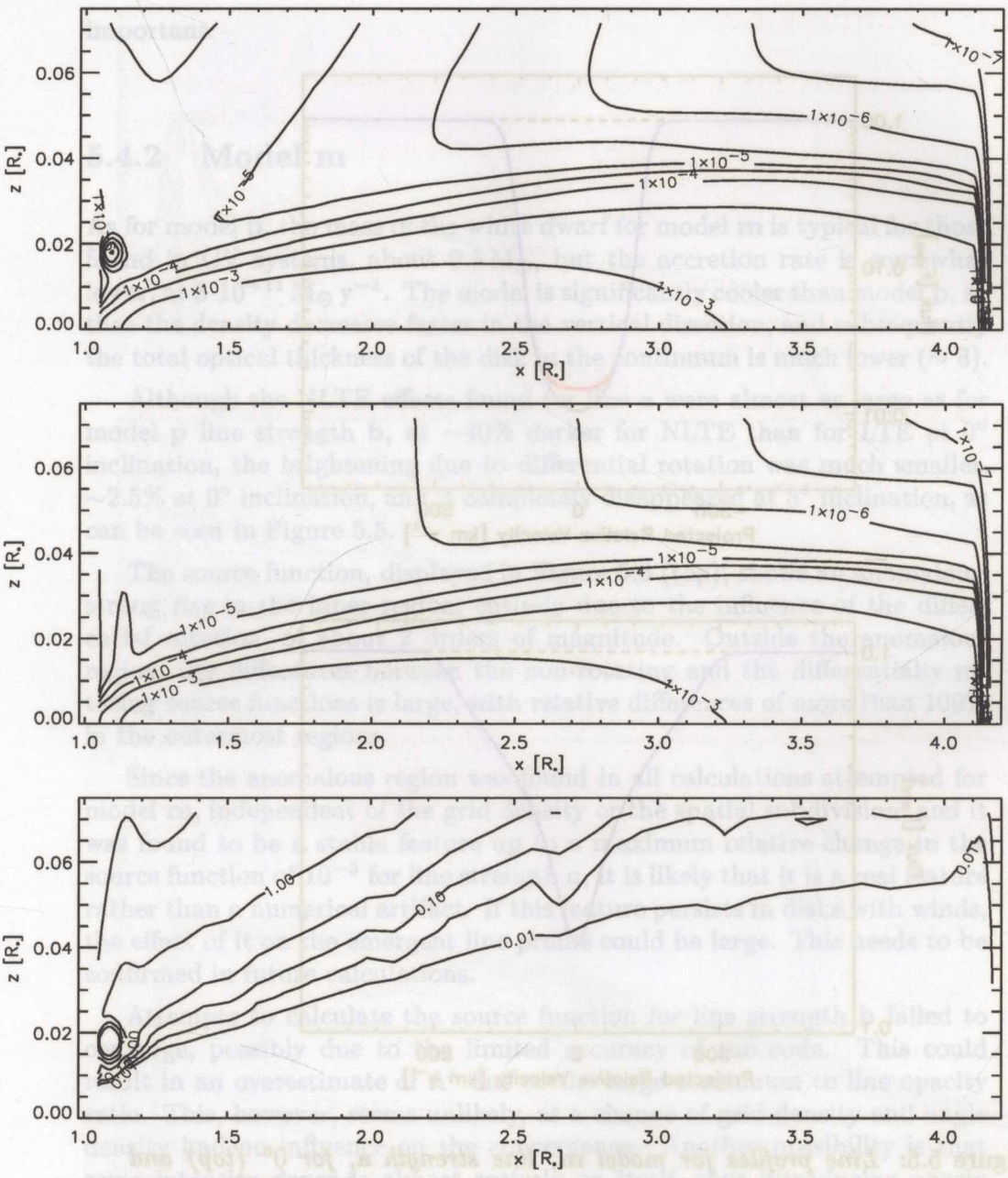


**Figure 5.6:** *Line source function in the differentially rotating (top) and non-rotating (middle) case, for model* **m**, *line strength* **a**. *The ratio* $(S_{l,rot}/S_{l,non-rot}) - 1$ *is plotted in the bottom figure, indicating significant differences in the optically thin regions of the disk, due only to differential rotation.*

## 5.5 Conclusion

We calculated the NLTE line profiles of some strong resonance lines on an LTE structure in the disks of cataclysmic variables. The NLTE effects on the line profile were found to darken the core of the line by a factor of about 0.6 at 0° inclination, sharply decreasing with inclination angle. The NLTE effects disappears completely for inclination angles larger than about 10°.

The effect of differential rotation on the NLTE effects was found to be of the same order of magnitude as the NLTE effects themselves, significantly brightening the core of strong lines at low inclination angles. The effect of differential rotation on weaker lines was found to be much smaller.

Although the effect of treating strong lines in NLTE is negligible for large inclination angles, the NLTE effects on the structure of the atmosphere have been found to be quite significant (Hauschildt et. al., 1997). The results presented here indicate that such calculations need to explicitly include the effects of the differential rotation of the disk to ensure accurate results, which in turn leads to a multidimensional treatment.

This is even more true in the case of disks with winds, where the atmosphere is much more extended in the vertical direction, and thus multi-D and NLTE effects are inherently more important.

The effect of differential rotation on the radiation force was found to be negligible. The tangential radiation force, $f_\varphi$, was found to be 4 to 5 orders of magnitude smaller than the radial or vertical radiation force. Furthermore, the vertical radiation force was found to dominate the radial force by 2 to 3 orders of magnitude, so that a radiatively accelerated wind is likely to move perpendicular to the disk.

## References

1. Adam, J; 1990, A.&A., **240**, 541
2. Bertout, C.; 1989, Annu. Rev. A. & A., **27**, 351
3. Catelan, P. & Theuns, T.; 1996a, M.N.R.A.S, **282**, 436
4. Catelan, P. & Theuns, T.; 1996b, M.N.R.A.S, **282**, 455
5. Córdova, F. & Mason, K.; 1982, ApJ., **260**, 716
6. Frank, J., King, A. & Raine, D.; *Accretion power in astrophysics*, 3rd ed., Cambridge univ. Press, New York, 2002

7. Greenstein, J. & Oke, J.; 1982, ApJ., **258**, 209

8. Hauschildt, P.; Shore, S.; Schwarz, G.; Baron, E.; Starrfield, S. & Allard, F.; 1997, ApJ., **490**, 803

9. Heap, S. R.; Boggess, A.; Holm, A.; Klinglesmith, D. A.; Sparks, W.; West, D.; Wu, C. C.; Boksenberg, A.; Willis, A. & Wilson, R.; 1978, Nature, **275**, 385

10. Hilditch, R.W.; *An introduction to Close Binaries*, Cambridge univ. Press, New York, 2001

11. Horne, K.; 1985, M.N.R.A.S., **213**, 129

12. Hubeny, I., 1990, ApJ., **351**, 632

13. Hubeny, I. & Plavec, M., 1991, A.J., **102**, 1156

14. Hubeny, I.; 1994, ASP Conf. Ser., **56**, 3

15. Kraft, R.; 1962, ApJ., **135**, 408

16. Kříž, S. & Hubeny, I., 1986, Bull. Astron. Inst. Czechoslovakia, **37**, 129

17. Lynden-Bell, D. & Pringle, J., 1974, M.N.R.A.S., **168**, 603

18. Marsh, T. & Horne, K.; 1988, M.N.R.A.S., **235**, 269

19. Papkalla, R; 1994, A.&A., **295**, 551

20. Patterson, J.; 1984, ApJSS., **54**, 443

21. Pereyra, N. & Kallman, T.; 2003, ApJ, **582**, 984

22. Pereyra, N.A., Kallman, T. and Blondin, J.; 1997, ApJ., **477**, 368

23. Pringle, J.; 1981, Ann. Rev. A. & A., **19**, 137

24. Proga, D.; Kallman, T.; Drew, J. & Hartley, L.; 2002, ApJ., **572**, 382

25. Robson, I.; 1999, IAU Symposium, **194**, 3

26. Shakura, N. & Sunyaev, R.; 1973, A. & A., **24**, 337

27. Wade, R. & Hubeny, I.; 1998, ApJ., **509**, 350

28. Warner, B; *Cataclysmic Variable Stars*, Cambridge University Press, New York, 1995.

29. Wehrse, R., Bascheck, B. and Shaviv, G.; 1994, ASP Conf. Ser., **56**, 35

# Chapter 6

# Summary

In this thesis, the multidimensional radiative transfer effects were investigated for two classes of objects for which multidimensional effects are expected.

First we developed a 2-D radiative transfer code that can solve the transfer equation in the 2-level atom formalism in Cartesian, cylindrical and spherical coordinate systems, the latter two with rotational symmetry. We used the short characteristics scheme, to reduce the numerical load of the code, together with accelerated lambda iteration (ALI), while using the locally comoving frame formulation. The short characteristics scheme was adapted to handle variations of the various local quantities due to curvature of the geometry as well as due to large velocities.

The code was parallelized to enable the use of the code for realistic problems on networked clusters of computers. This was done by spatially splitting the problem in sub-domains. This method proved to be stable and efficient for many astrophysically interesting problems.

The accuracy of the short characteristics scheme was tested for a variety of test problems, by calculating problems in 1-D and in 2-D in different coordinate systems. The accuracy of the code was shown to be of order 1-2% in static cases, and of order 5% in slowly moving structures.

A code was also developed for generating line profiles on 2-D structures, given the source function, using the long characteristics method and an adaptive mesh refinement (AMR) method for maintaining sufficient accuracy. This code was found to be very accurate (better than 1%), provided the source function is accurate.

Both codes were then applied to the problem of differential rotation in

stellar winds. The atmosphere of a typical star of spectral type B was calculated approximately, after which the source function, line profile and radiation forces were calculated. The effect of the rotation on the line profiles was found to be remarkably small, with typical changes over a range in line strength of 4 orders of magnitude of no more than $\sim$ 20%, even at 90% of the breakup velocity, resulting in an equatorial expansion of the star of about 25%. Also, the approximate method of broadening a spectral line for a given rotation velocity was found to be useful up to 90% of the breakup rotation rate, for modest inclination angles. Only for large inclination angles are the effects of the rotation on the line profiles significantly different from rotationally broadened line profiles to justify a more thorough investigation.

The latitudinal radiation force, calculated with the 2-D short characteristics code, were found to be directed toward the poles. For the strongest lines calculated here, the force was at most around 20% of the radial radiation force, and must be considered dynamically important for the dynamics of the wind, as it is not balanced by the gravity as is the case for the radial radiation force. The latitudinal component of the wind was found to be mostly due to the physical deformation of the wind structure itself rather than due to the differential rotation of the structure, and is therefore likely to be sensitive to a self-consistent treatment of the structure and the radiation field.

The tangential radiation force was found to be typically of order 2-5% of the radial force, and was not found to depend strongly on the line strength. It is directed against the direction of rotation, and thus works to decrease the rotation velocity of the wind. This force is unlikely to be dynamically important,as it is relatively small compared to the dominant forces in the wind.

## 6.1 Conclusion

The results from chapters 4 and 5 show that a multidimensional treatment of the radiation field is needed in order to calculate accurate spectra for some extended objects. The small changes for the line formation in rotating winds is surprising, and should serve as a warning that things may not be what they appear at first sight. Although the flux levels are 1.5 times higher for a fast rotating star than for a non-rotating star, when viewed pole-on, the differences in the observed line profiles are unlikely to be unambiguously attributable to the rotation alone. However, by increasing the level of detail, it may be possible to constrain the configuration further.

The precise effects of rotation on the structure of these winds is difficult to estimate without a more self-consistent approach to calculate the wind structure, but given the magnitude of the non-radial radiation forces, significant structural changes are likely.

The NLTE effects in disks are clearly larger, although the effect of them on the line profiles is largely lost due to the large rotational broadening in all but systems observed at low inclination. Significant changes in the line profiles of strong lines can be expected when vertical outflows are included, and this will be investigated in future work.

## 6.2 Future work

The development and subsequent application of the 2-D radiative transfer code, presented in chapter 2, has shown that there is a wide gap between the development of this type of code and the application of it to realistic astrophysical problems. Resolution is the key aspect prohibiting a widespread application of the code to many problems of interest.

Future codes may deal with these problems by using

- a more flexible grid (a triangular grid method has been recently implemented by Vinkovic Ivezic & Elitzur 2002) or even no grid at all. Surfaces of constant value of quantities may be represented by a number of triangles. If efficient methods can be developed to determine the optimum position of the points, the number of points may be greatly reduced.

- automatic resolution management in all dimensions (spatial, angular and frequency), for instance based on AMR techniques;

- optimizing the method for parallelization, i.e. a more expensive method may be used if it is possible to parallelize more efficiently, depending on the available CPU time;

Although it is unlikely that any of these properties come at no additional cost, the reduction of the number of grid points may well lead to a reduction of the total cost. Implementing them will, however, very likely lead to improved stability and accuracy of the code.

Finally, a more detailed treatment of atomic data and energy balance is needed to generate more detailed model atmospheres. This will gradually improve as the available computer speed improves.

# References

1. Vinkovic, D.; Ivezic, Z. & Elitzur, M., 2002, AAS Meeting 200, #85.04